UNIVERSITY OF STRATHCLYDE

Model Based Cross-directional Monitoring and Control of Plastic Film Thickness

by

Sung-ho Hur

A thesis presented in fulfilment of the requirements
for the degree of Doctor of Philosophy

in the

Faculty of Engineering
Department of Electronic & Electrical Engineering

2010

Declaration of Authorship

I, Sung-ho Hur, declare that

- This thesis is the result of my original research. It has been composed by myself and has not been previously submitted for examination which has led to the award of a degree.
- The copyright of this thesis belongs to the author under the terms of the United Kingdom Copyright Acts as qualified by University of Strathclyde Regulation 3.50. Due acknowledgement must always be made of the use of any material contained in, or derived from, this thesis.

Signed: _____

Date: _____

UNIVERSITY OF STRATHCLYDE

Abstract

Faculty of Engineering
Department of Electronic & Electrical Engineering

Doctor of Philosophy

by Sung-ho Hur

The main topics of this research are modelling, fault monitoring, and cross-directional control of a plastic film manufacturing process operated by DuPont Teijin Films Ltd.

The developed model is of high dimension and built using the first-principles of chemical and mechanical engineering, such as equations for mass transfer, heat transfer, and the flow of viscous fluids in addition to empirical knowledge related to the behaviour of polymer. The model in turn provides a safe off-line platform for developing new cross-directional control and fault monitoring systems.

As with other sheet-forming processes, such as papermaking and steel rolling, the plastic film manufacturing process employs large arrays of actuators spread across a continuously moving sheet to control the cross-directional profiles of key product properties. In plastic manufacturing, the main control property is finished product thickness profile as measured by a scanning gauge downstream from the actuators. The role of the cross-directional control system is to maintain the measured cross-directional profiles of plastic properties on target. The second part of this research develops a novel cross-directional controller, which is in turn demonstrated by application to the first-principles model.

Fault monitoring systems can be broadly classified into 3 categories: model-based, data-driven, and knowledge-based. The third part of this research introduces a novel model-based fault monitoring system. The system is demonstrated by application to both the first-principles model and industrial data extracted from the real-life plant.

Acknowledgements

First, I would like to thank my supervisor, Dr. Reza Katebi for keeping me in the best direction throughout the project, his encouragements, and enthusiasm he always showed for my work. His careful reading of this thesis has improved its quality significantly.

I would like to express my sincere appreciation to Dr. Andrew Taylor for his support and for being my co-supervisor in DuPont Teijin Films UK Ltd. Frequent project update meetings, important process data, company reports, and more have helped me complete this project.

I am grateful to Dr. Jonas Balderud for his guidance throughout the first part of this project before leaving the industrial control centre (ICC). All those chemical engineering lectures at the beginning of this project are very much appreciated.

I would like to thank my second supervisor Prof. Michael Grimble for his encouragements. I am grateful to all the staff in the ICC including Sheila Campbell and Drew Smith and the rest of my colleagues for creating a pleasant and stimulating working environment.

I would like to acknowledge financial support of this project from DuPont Teijin Films UK Ltd, UK EPSRC Industrial CASE Award, and UK EPSRC Platform Grant (GR/R04683/01). I would like to thank DuPont Teijin Films UK Ltd for their contributions to the modelling part of this project and their staff including Alan Jones, Andrew Doonan, Pierre Moussalli, and Sean Donoghue for travelling to the ICC to attend a project update meeting.

I would like to pay special tribute to my wife for all she has done for me. I am indebted to my parents and brother for their support and believing in me. Last but not least, I would like to thank my parents-in-law for their encouragements and support in many ways ever since we first met.

Contents

List of Figures

List of Tables

Abbreviations

Cast	**Cast**ing Drum
Cool	**Cool**ing Rolls
CD	**C**ross **D**irection(al)
DBH	**D**ie **B**olt **H**eaters
DTF	**D**uPont **T**eijin **F**ilms UK Ltd
FR	**F**ast-nip **R**olls
FDD	**F**ault **D**etection & **D**iagnosis
FDA	**F**isher **D**iscriminant **A**nalysis
FD	**F**orward **D**raw
ICI	**I**mperial **C**hemical **I**ndustries
IMC	**I**nternal **M**odel **C**ontrol
MD	**M**achine **D**irection(al)
MF	**M**ass **F**low
NL	**N**onlinear **E**lement
PLS	**P**artial **L**east **S**quares
PA	**P**oly**a**mide
PEN	**P**oly**e**thelene **N**aphthalate
PET	**P**oly**e**thelene **T**erephthalate
PP	**P**oly**p**ropylen
PS	**P**oly**s**tyrene
PH	**P**re-**h**eat Rolls
PCA	**P**rinciple **C**omponent **A**nalysis
PA	**P**rocess **A**rray
PRBS	**P**seudo **R**andom **B**inary **S**ignal
SC	**S**tandard **C**onditions
SD	**S**ideways **D**raw
SR	**S**low-nip **R**olls

ST **St**enter Oven

Symbols

u	actuator set-points	%
A	area	m^2
W	basis weight	kg/m^2
k	conductivity	W/Km
k	delay	
d	distance or thickness	m
E_i	disturbance distribution matrix	
d	disturbance signal	
e	error signal	
R_i	fault distribution matrix	
f	fault signal	
F	force	N
g	gap (taper or die-lip)	m
H	half width of die body	m
Q	heat transfer	W or J/s
h	heat transfer coefficient	W/m^2K
G	interaction matrix	
G_r	interaction matrix (reduced)	
L	length (taper or land)	m
$\tilde{l}$	length of film (stretched)	m
l	length of film (un-stretched)	m
m	mass	kg
$\dot{m}$	mass flow rate	kg/s
M_c	mass fraction crystalline	%
k	material conductivity	W/mK
y	measurements (thickness)	%

N	number of actuators	
M	number of measurements	
J_i	performance index	
d	process delay	
P	pressure	Pa or bar
k_g	process gain (first-principles model)	
k_p	process gain (industrial model)	
r	residual signal	
C_p	specific heat capacity	$J/kg/K$ or $J/kg/°\mathrm{C}$
T	temperature	K
$\tilde{h}$	thickness of film (stretched)	m
h	thickness of film (un-stretched)	m
v	velocity	m/s
f	viscosity factor	
V	volumetric flow	m^3/s
$\tilde{w}$	width of film (stretched)	m
w	width of film (un-stretched)	m
ψ	accuray of estimated state space model	
ω	angular frequency	rads^{-1}
ξ	correction factor (mass flow)	
η	correction factor (neck-in)	
ρ	density	kg/m^3
ϵ	emissivity	
μ_n	mean of column n in G or G_r	
Γ	smoothing matrix	
σ	Stefan-Boltzmann constant	W/m^2K^2
ϵ	strain	%
σ	stress	Pa or bar
Λ	stretch ratio (sideways-draw)	
α	time constant	
β	tuning factor (proposed controller)	
μ	viscosity	$Pa \cdot s$

To my wife and son, Hyejoo and Daegyu

Chapter 1

Introduction

The study presented in this thesis explores three important areas of process control – modelling, control, and fault monitoring of an industrial process. The industrial process considered in the study is a plastic film manufacturing process operated by DuPont Teijin Films UK Ltd (DTF).

1.1 Background and Motivation

Plastic film manufacturing processes are exploited to produce a variety of product including plastic bags, windshield safety glass, medical test strips, magnetic cards, electronic display, floppy disks, and video tapes (MacDonald, 2007). The process converts polymer resin to plastic films via a number of complex stages such as melting, filtering, deforming, orienting, heating, crystallising, coating, and winding (Looney et al., 2005). Every stage must be performed prudently to produce finished product that meets strict quality requirements. The overall process that combines all these stages is large-scale and can be complex.

A plastic film manufacturing process is a sheet-forming process as with paper-making, sheet metal rolling, and plate glass manufacture. The most important quality requirement of a sheet-forming process is the cross-directional (CD) thickness profile of the finished product, where CD thickness profile refers to the thickness profile across the width of the sheet as shown in Figure 1.1. To ensure that the CD thickness profile of the plastic film remains as flat as possible, the plastic

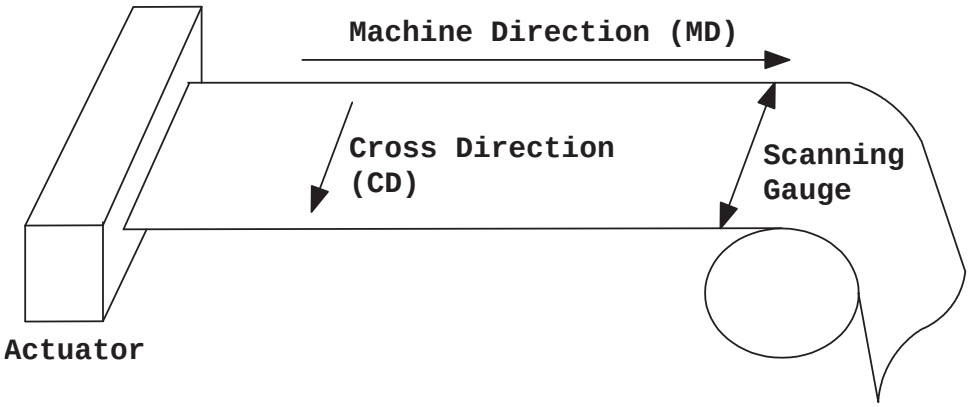

FIGURE 1.1: Schematic diagram of a generic sheet-forming process

film industry started implementing CD control systems in the 1970s although widespread use of such systems did not occur until the 1980s (Featherstone et al., 2000). The machine-direction (MD), on the other hand, is the direction of flow as depicted in the figure. There exist strong interactions between actuator movements and the resulting CD thickness profile. The CD thickness profile control is therefore considered more difficult than the MD thickness profile control (Åström, 1977, 1973; Bialkowski, 1978, 1983; Cegrell and Hedqvist, 1975; Dumont, 1989; Ma and Williams, 1988; Sikora et al., 1984), and this thesis will focus mainly on the CD problem.

In line with other sheet-forming processes, plastic film manufacturing processes employ a large array of actuators across the continuously moving sheet (film) to control the CD thickness profile of the finished product, which is measured by a scanning gauge downstream from the actuators as illustrated in Figure 1.1. The scanning gauge travels back and forth across the moving sheet, and a zigzag pattern of measurements is thus generated. The actuators are uniformly spaced in the cross-direction (CD), and the portions of the sheet affected by each actuator overlap significantly owing to the fluid and solid mechanics in the sheet. Moreover, there exists a time delay between the time when the actuators are adjusted and the time when the CD thickness profile is measured by the scanning gauge. For controlling purposes, the plastic film needs to be divided into many (up to a few hundreds) CD sections, and there can be as many actuators, resulting in a high number of inputs and outputs. Due to all these characteristics of the process, control and monitoring of the process can be complex and challenging.

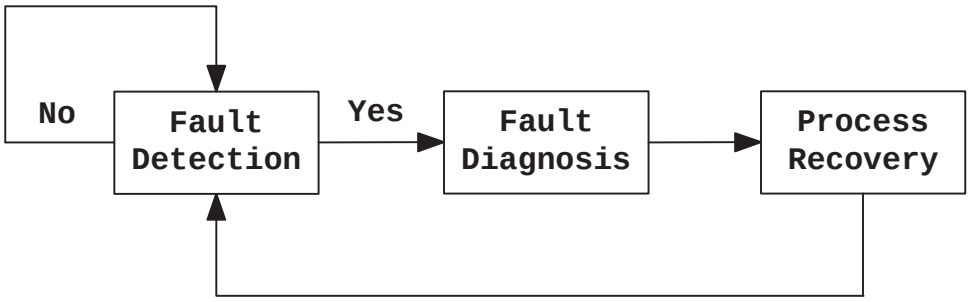

FIGURE 1.2: Schematic diagram of a fault monitoring loop

Further, although CD control systems compensate for many types of disturbances, there are changes in the process that the control system cannot compensate for adequately. These changes are referred to as faults. Types of faults occurring in industrial processes include actuator faults, sensor faults, and process parameter changes. For industrial processes to satisfy the performance specifications, any faults in the process need to be detected, diagnosed, and removed. These tasks as a whole are referred to as fault monitoring and depicted in Figure 1.2. Successful fault monitoring can maintain the planned operations by keeping the plant operators and maintenance personnel better informed of the process status. It will therefore help them remove abnormal behaviour from the process (Chiang et al., 2001).

1.2 Objectives and Methodology

The development of a model-based CD controller and fault monitoring system are two main objectives of this thesis. Because they are model-based, a detailed mathematical model is a prerequisite. Consequently, the development of a mathematical model of the plastic film manufacturing process is another objective of this thesis.

1.2.1 Process Modelling

The model developed in this thesis is built using the first-principles of chemical and mechanical engineering, such as equations for mass transfer, heat transfer,

and the flow of viscous fluids in addition to empirical knowledge related to the behaviour of polymer. This is more general to derive a model from experimental input-output data because it is often too complex and challenging to accurately construct a model using first-principles due to the complexities associated with the process, such as particle-particle interactions, crystallisation, deformation and fracture mechanics, and non-linear viscosity variation (VanAntwerp et al., 2007).

Some progress has been made to develop first-principles models of plastic film manufacturing processes, but these models are still very rare. However, when such a model becomes available, it can bring many benefits. For instance, most model-based control and monitoring algorithms require a state-space or transfer function model identified from the process. The model can be used to simulate the process enabling shorter and more flexible identification experiments leading to less wasted product. By simulating the process, the model also allows new and existing control and fault monitoring algorithms to be developed without wasting product. Adding disturbances and faults allows the simulation of realistic scenarios where faults and disturbances are present without the need for experiments on the real-life process. Moreover, it would be useful for tuning the process and training the plant operators and allow for the determination of the optimal design, position, and spacing of sensors and actuators.

1.2.2 Cross-directional Control

CD control is usually model-based or robust. Briefly, the former offers improved steady state performance when the reference model required for model-based control is accurate enough, while the latter guarantees more robust dynamic performance (Heath and Wills, 2002). Robust control systems such as those reported in Duncan and Bryant (1997), Stewart et al. (2003a), and Taylor and Duncan (2006) have been applied to real-life industrial sheet-forming processes successfully.

Model-based control systems, on the other hand, have not been suitable for high speed sheet-forming processes because an online optimisation needs to be solved at each sampling instant and because an accurate mathematical model is necessary. However, significant improvement in computer processor speed over the last decade and the first-principles model as a result of the first objective of this thesis make model-based CD control more suitable. The CD control system developed

in this thesis is a modification of internal model control (IMC) but also includes an observer. This observer is designed to minimise the effects of disturbances and modelling errors to bring improved tracking and robust performance. Moreover, a new objective function is introduced and optimised online subject to constraints for the optimal steady state performance.

1.2.3 Fault Monitoring

The model-based approach rather than the data-driven or knowledge-based approach is used to develop a fault monitoring system. Specifically, the parity relations (Deckert et al., 1977; Frank, 1990; Gertler, 1998; Lou et al., 1986; Mironovski, 1979, 1980) are utilised for residual generation, which can be the most important task in model-based fault monitoring. For good fault detection, a multi-objective optimisation problem must be solved in order for the residual to be sensitive to faults but insensitive to disturbances and modelling errors. Analytic solutions are generally employed for solving this multi-objective optimisation problem. Breaking this tradition, an evolutionary algorithm, or more specifically, a genetic algorithm, is utilised for solving this multi-objective optimisation problem in this thesis. The use of a genetic algorithm can increase the possibility of finding the global optimisation solution (global minimum) by avoiding the calculation of cost function gradients, which can lead to local minima. Another advantage of utilising a genetic algorithm is that it is rather simple to understand and implement.

Once a fault has been detected, the next stage is to determine which fault has occurred, and this stage is often referred to as fault diagnosis. Although many books and papers neglect fault diagnosis and focus on fault detection only, the fault monitoring system developed in this thesis performs fault diagnosis by constructing a set of structured residuals. Each residual is designed to be sensitive to a subset of faults, while being insensitive to any other faults. Consequently, fault diagnosis becomes the problem of determining which residual is non-zero or has violated the thresholds. The task that should follow fault detection and diagnosis is process recovery as depicted in Figure 1.2. In general, this stage is performed manually by the plant operators referring to the structured residual set. The downtime required for this stage can thus be minimised by good fault

detection and diagnosis (FDD). Hence the development of improved FDD systems is essential to enhance safety and production rates for existing equipment and to reduce product defects, raw material consumption, and energy consumption.

1.3 Structure and Content of the Thesis

This thesis is composed of three parts. The first part is the development of a first-principles model describing the plastic film manufacturing process. In order to develop such a model, it is essential to understand all the stages of the process including extrusion, where a polymer melt is fed into a die; casting, where the polymer melt is discharged through the die-lip gap onto a rotating casting drum to form a continuous amorphous sheet; MD stretching; CD stretching; heat setting; and winding, where finished product is rolled. All these stages are described in Chapter 2 and mathematically modelled in Chapter 3. The resulting model is a large-scale model and is based on the first-principles of chemical and mechanical engineering such as mass transfer, heat transfer, and deformation. The validation of the model built in Matlab/Simulink® is carried out using data provided by DuPont Teijin Films UK Ltd (DTF) and is presented in Chapter 4.

The second part of the thesis introduces a novel CD controller design in Chapter 5. This CD controller is model-based and thus requires a reference model of the process, specifically in the state-space form. The first-principles model developed in Chapter 3 simulates the real-life process, and the reference model is therefore identified from this model. System identification is an active topic in the field of CD control but is not a main topic in this thesis. Nevertheless, the subspace identification method provided by the System Identification Toolbox™7 in Matlab® is utilised for deriving a reference model in the state-space form in Appendix B. This state-space model is also employed for designing a fault monitoring system in Chapter 6. The performance of the CD controller is demonstrated by its application to the first-principles model under various disturbance scenarios. Existing CD controllers are also applied to the first-principles model under the same disturbance scenarios to determine how well the proposed controller works compared with the existing controllers.

The third part of the thesis presents the development of a model-based fault monitoring system that requires solving a multi-objective optimisation problem in Chapter 6. A genetic algorithm is used for solving this optimisation problem, and an introduction to the genetic algorithm is presented in Appendix C. To assess the fault monitoring system, it is applied not only to the first-principles model under various disturbance and fault scenarios but also to data extracted from the real-life process under a faulty condition in Chapter 6.

Chapter 7 summarises the thesis and discusses open problems which can help increase the performance of the first-principles modelling, CD controller, and fault monitoring system. The parameters of the first-principles model are summarised in Appendix A, and a few samples of the Simulink® models and Matlab® files are presented in Appendix D.

1.4 Contributions of the Thesis

The contributions of this thesis can be summarised as follows:

- Review of the plastic film manufacturing process (Chapter 2)
- Development of a first-principles model for the plastic film manufacturing process (Chapters 3; [1], [2], [3], and [4] in Section 1.5)
- Implementation, parameter tuning, and validation of the first-principles model (Chapter 4; [1], [2], [3], and [4] in Section 1.5)
- Identification and validation of a state-space model required for the new model-based controller and fault monitoring system (Appendix B)
- Analysis of existing CD controllers and their application to the first-principles model (Chapter 5; [1], [4], and [5] in Section 1.5)
- Development of a novel CD controller and its application to the first-principles model (Chapter 5; [1] and [5] in Section 1.5)
- Development of a novel fault monitoring system and its application to the first-principles model and data collected from the real-life process (Chapter 6; [2] and [6] in Section 1.5)

1.5 Publications Arising from the Thesis

1.5.1 Journal Papers

[1] Hur, S., Katebi, R., and Taylor, A. (2010). Modelling and control of a plastic film manufacturing web process. Submitted to *IEEE transactions on Industrial Informatics*

[2] Hur, S., Katebi, R., and Taylor, A. (2010). Model-based fault monitoring of a plastic film extrusion process. Submitted to *IET transactions on Control Theory & Applications*

1.5.2 Conference Papers

[3] Hur, S., Balderud, J., Katebi, R., and Taylor, A. (2008). A control and monitoring oriented model of a film manufacturing process. *In Proceedings of the 17th World Congress The International Federation of Automatic Control (IFAC), Seoul, Korea*, 8357-8361.

[4] Hur, S., Balderud, J., Katebi, R., and Taylor, A. (2009). Cross directional control of a film manufacturing process using a first principle model. In *Proceedings of the European Control Conference (ECC) 2009, Budapest, Hungary*, 4475-4480.

[5] Hur, S., Katebi, R., and Taylor, A. (2010). Model-based controller design for a plastic film extrusion process. Accepted for presentation at *the 2010 IEEE Multi-Conference on Systems and Control (MSC), Yokohama, Japan.*

[6] Hur, S., Katebi, R., and Taylor, A. (2010). Fault detection and diagnosis of a plastic film extrusion process. Accepted for presentation at *the UKACC International Conference on Control (Control 2010), Coventry, U.K.*

Chapter 2

Plastic Film Manufacturing

The first synthetic polymer, celluloid was invented by John Wesley Hyatt in 1869, but the rapid growth of the polymer industry started in the 1930s with the development of acrylic polymers, polystyrene, nylon, and polyurethanes followed by the advent of polyethylene, polyethelene terephthalate (PET), polypropylene, and other polymers in the 1940s and 1950s. Polymers are usually compounded with other materials such as flame retardants, colourants, fillers (to reduce cost), and other polymers before being processed (Vlachopoulos and Strutt, 2003). The resulting compounds are referred to as plastics, which can be classified into two categories: thermoplastics and thermosets (Tucker, 1989). Thermoplastics can be melted by heating and solidified with cooling, and the examples include PET, polyethelene naphthalate (PEN), nylon, and celluloid. Thermosets, on the other hand, is hardened by heat due to cross-linking of polymer chains. Thermosets, such as bakelite, duroplast, and polymides, are generally stronger than thermoplastics and thus more suitable for high temperature applications. The plastic film manufacturing process described in this chapter is concerned with thermoplastics.

The process presented in this chapter is adopted by DuPont Teijin Films UK Ltd (DTF) for producing biaxially oriented plastic films, which include biaxially oriented PET and PEN films. The plastic films are stretched in the machine direction (MD) and cross direction (CD), thereby becoming biaxially oriented. The original work in making biaxial oriented PET films was carried out by Imperial

Chemical Industries (ICI) Ltd in the 1930s, and DuPont started producing them in 1952 in the UK (Taylor, 1989).

The main features achieved by biaxially oriented plastic films include good tensile strength, resistance to shrinkage and wrinkles, barrier to water vapour, and clarity. The most commonly employed methods for generating such plastic films are the double bubble tubular method (Kang and White, 1990; Kang et al., 1990; Kim and White, 1992; Song and White, 2000a; Rhee and White, 2001; Song and White, 2000b; Yamane and White, 1987) and the stenter method (DTF, 2005; Kanai and Campbell, 1999; Levy and Carley, 1989; Looney et al., 2005; MacDonald, 2007; Stevens and Covas, 1995; Tucker, 1989). The former biaxially stretches the film at once and the latter conducts biaxial stretching via two stages. Only the stenter method, which is utilised by DTF, is described step by step in the following sections.

2.1 Preparation

Crystallisation, drying, and blending are performed simultaneously during the preparation stage. As shown in Figure 2.1, a pump feeds polymers through the cutter, where the polymers are cut into pellets. Prior to the drying stage, the pellets are partially crystallised to avoid chip sintering, which may block the outlets. Subsequently, the pellets are dried to reduce the water content to prevent degradation resulting from hydrolysis, which may occur later in the process. Once dried and in turn cooled, these pellets are blended with reclaimed pellets, which are edge trimmed films (Section 2.8). The combined pellets are then fed into the extruder, which is the first stage of the drawing process, through the silo.

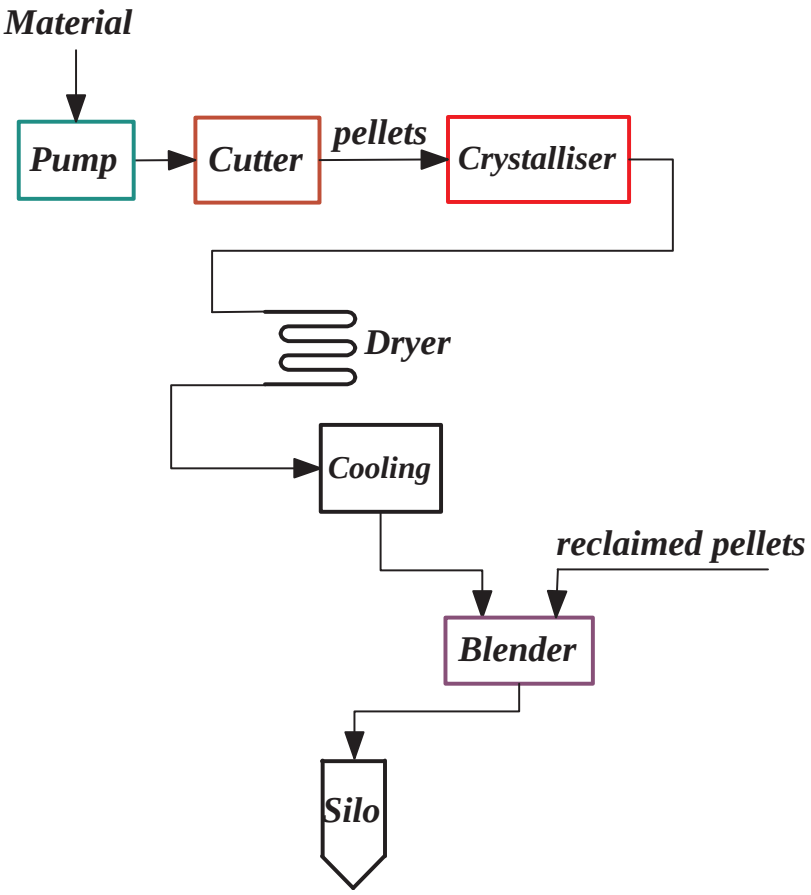

FIGURE 2.1: Polymer preparation

2.2 Extrusion

Extruders often employ one or more screw extruders comprising an Archimedean screw rotating in a heated barrel as depicted in Figure 2.2. In single screw extrusion, which is the most widely used method, the raw material (polymer pellets) from the silo shown in Figure 2.1 is fed into the space between the temperature controlled barrel and the screw. The motor rotates the screw, thereby conveying the raw material from left to right in Figure 2.2. As the raw material is conveyed by the screw rotation, it is subjected to melting as the heaters increase the temperature of the barrel which transmits heat to the polymer. The pellets are consequently converted into melt while travelling through the conveying channels on the screw as shown in Figure 2.3. Although not depicted in the figure, the

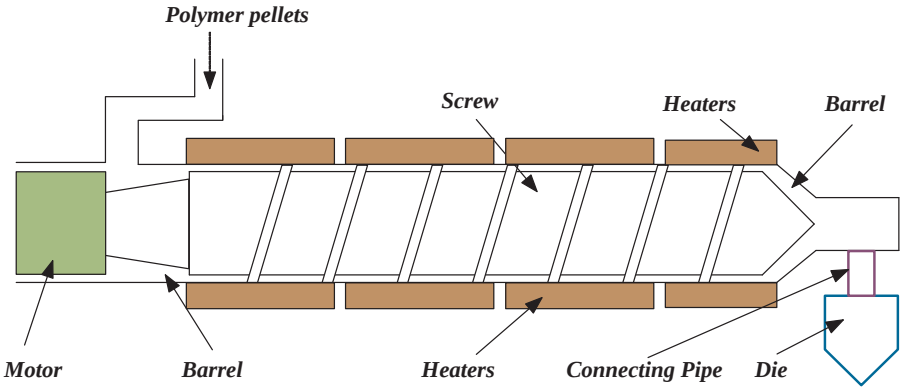

FIGURE 2.2: Single screw extrusion

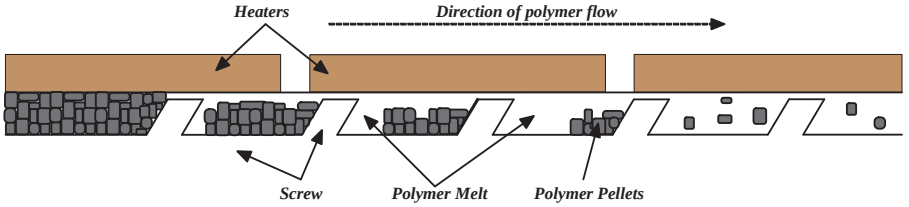

FIGURE 2.3: Polymer melt surrounding polymer pellets in screw conveying channels

conveying channel on the screw is often contoured from large to small in the direction of flow to take account of the density change, which occurs as the polymer pellets are converted into melt and for pressure development.

Another extrusion method that can be employed is tandem screw extrusion. In contrast to the single screw extruder, where conveying of raw materials, melting, and blending are processed with one single screw extruder, tandem screw extruders share these tasks between two single screw extruders that are connected in series. In general, the primary extruder focuses on melting and is of high-speed whereas the secondary extruder focuses on blending and rotates at a lower speed than the primary extruder. Because of the use of two extruders which share tasks, higher capacity extrusion is possible, and because the secondary extruder is allowed to rotate at lower temperature, the temperature of the polymer melt flowing into the die can be reduced if required.

Whichever method is used, the main purpose of extrusion is to deliver polymer melt to the die at a constant mass flow rate.

2.3 Filter and Die

As the polymer melt exits the extruder, it is pumped into the die through the pipe as depicted in Figure 2.2. A filter is often placed between the extruder-outlet and the die-inlet to prevent impurities, such as degraded polymer, gels, and pipe deposits, from entering the die. Especially for product which requires high-quality performance such as PET video tapes and capacitors, the use of an appropriate filter unit is essential. As the process of replacing the filter unit can cause reduction in productivity, the filter needs to be long-life.

The purpose of the die is to convert the melt of a circular cross-section, due to the circular cross-section of the connecting pipe, into a uniformly thick melt curtain of the required width through the die-lip shown in Figure 2.4. The geometry of a die is often designed so that the area of the cross-section decreases from the feed-side to the other side known as blank-side as depicted in the figure. This is because, if the cross-directional area of the die were uniform, the residence time would increase towards the blank-side, and an increase in the residence time can increase the chance of degradation occurring (DTF, 2006a).

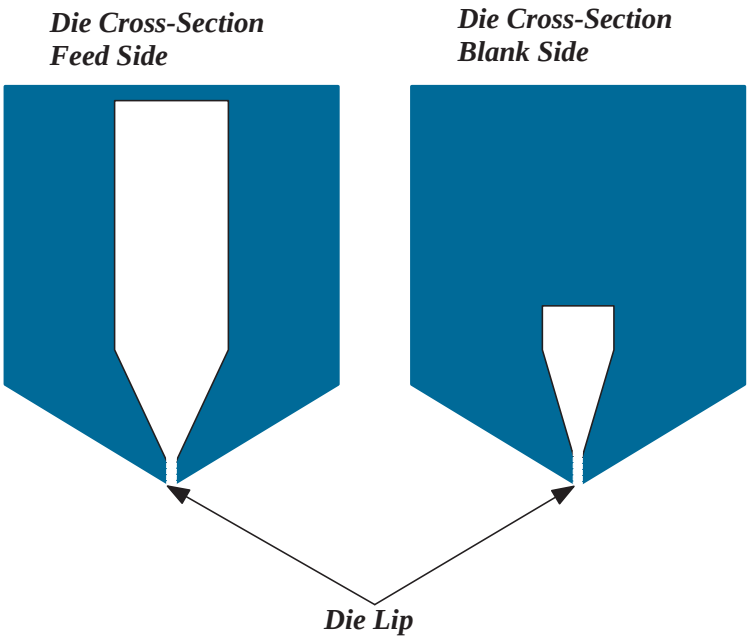

FIGURE 2.4: Cross section of the die, Left: feed-side, Right: blank-side

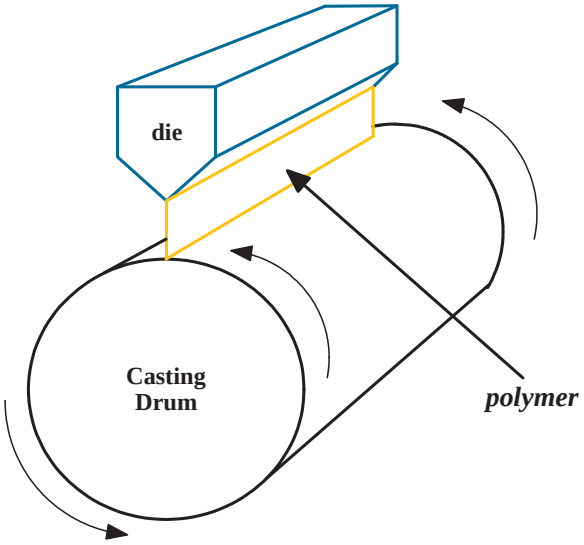

FIGURE 2.5: Die to casting drum

The gauging sensor (Section 2.8) located before the winder is employed to measure the CD thickness profile of product, which is signalled to the die-lip. The die-lip is designed to produce an adjustment to local melt flow rate and hence the thickness of the film towards the end of the process – this is the principle mechanism of CD control discussed in Chapter 5. The most commonly used methods are die-lip gap adjustment and viscosity adjustment using die-bolt heaters (DBH). The former employs a large array of adjusting-bolts, each rotated by the corresponding servo-motor. The latter, on the other hand, employs an array of die-bolt heaters with a fixed die-lip gap. By heating the local melt, the local viscosity increases resulting in higher mass flow rate, hence increased thickness, or vice versa. The viscosity adjustment method has an advantage of achieving more precise adjustment but is limited to specific kinds of polymer, whereas the die-lip gap adjustment method benefits from having quicker response time. The die-lip gap adjustment method is considered in this study.

2.4 Casting

Polymer melt curtain extruded through the die-lip is drawn down onto a casting drum in order to establish a continuous and uniformly thick base sheet of

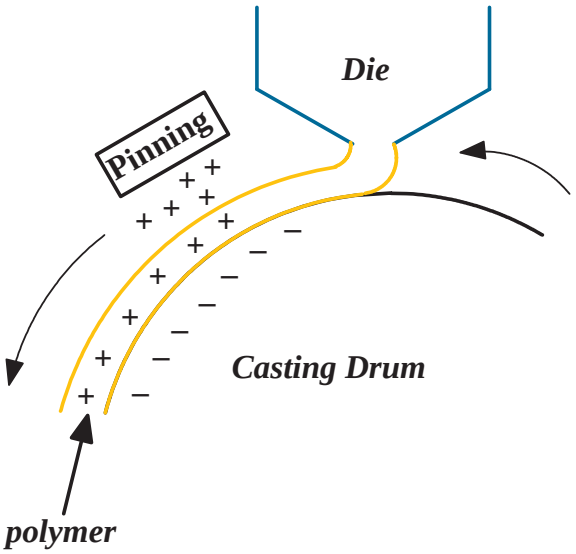

FIGURE 2.6: Electrostatic pinning

polymer as depicted in Figure 2.5. The casting drum is designed to cool down and thus solidify the base sheet. Polymers crystallise at temperature below the melting temperature and above the glass transition temperature. PET films have a melting temperature and glass transition temperature of approximately 260°C and 80°C, respectively, and the temperature of melt curtain from the die is approximately 300°C. Since crystallisation increases brittleness and can cause film breakage later in the process, the temperature of the film needs to be brought to temperature below its glass transition temperature as quickly as possible. Only times that require the polymer to crystallise are while it is being stretched in the MD and CD so as to cause biaxial orientation of polymeric molecular chains and during the crystallisation stage towards the end of the process. This crystallisation stage, which is discussed in more detail in Section 2.7, improves tensile properties, removes the stress caused by the stretching, and therefore prevent the plastic film from shrinking back at high temperature and over time.

To cool down the base sheet evenly on both sides, various methods have been proposed depending on the type of polymer. Examples include multi-rolls of small diameters, a single roll of a large diameter often with a water spray, and both. A water spray (Kanai and Campbell, 1999) is placed such that the base sheet lies between the casting drum and the spray and is responsible for cooling the air-side (or air contacting side) of the base sheet. For cooling the other side

of the sheet (drum-side), the temperature of the casting drum is controlled by adjusting the temperature of the water inside the casting drum, whose surface needs to be a good conductant.

The base sheet needs to be pinned onto the casting drum; otherwise, not only is the efficiency of cooling lowered, but the air between the base sheet and the casting drum becomes entrapped causing the bubbles to remain on the base sheet. This problem is often referred to as pinner-bubble or surface roughening (Kanai and Campbell, 1999). The pinning method considered in this study is electrostatic pinning. An electrostatic field is generated by the pinning unit, thereby inducing a charge on the base sheet. This forces the base sheet onto the surface of the casting drum since the casting drum is earthed as shown in Figure 2.6.

To avoid thickness variation in the MD, the casting drum needs to rotate smoothly at a constant speed and is therefore speed-controlled. The process consists of four speed controllers: one each for casting-drum, slow-nip rolls, fast-nip rolls, and stenter oven. The rest of the rolls are passively rotated by the moving film. As described in Section 2.5, the speeds of the slow and fast-nip rolls need to be different in order to stretch the film, but the speeds of the casting-drum and slow-nip rolls need to be the same, and those of the fast-nip rolls and stenter oven also need to be the same; otherwise, unwanted stretching of the film can occur due to the speed differences.

As the polymer curtain falls onto the surface of the casting drum, the width of the curtain decreases and the edges become thicker than the rest regions. This phenomenon adds another complexity to modelling of the process and is known as neck-in. It also occurs during the forward-draw stage and is discussed in the following section.

2.5 Forward-draw

A base sheet that has been processed via the casting stage is referred to as a cast film. The slow and fast-nip rolls shown in Figure 2.7 are speed-controlled and rotate at different speeds. As the names suggest, the fast-nip rolls rotate at a faster speed than the slow-nip rolls. The cast film passes over a series of

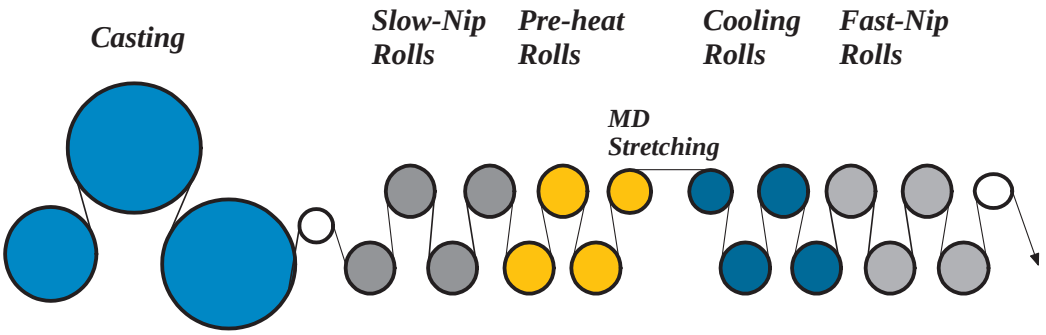

FIGURE 2.7: Casting to fast-nip rolls

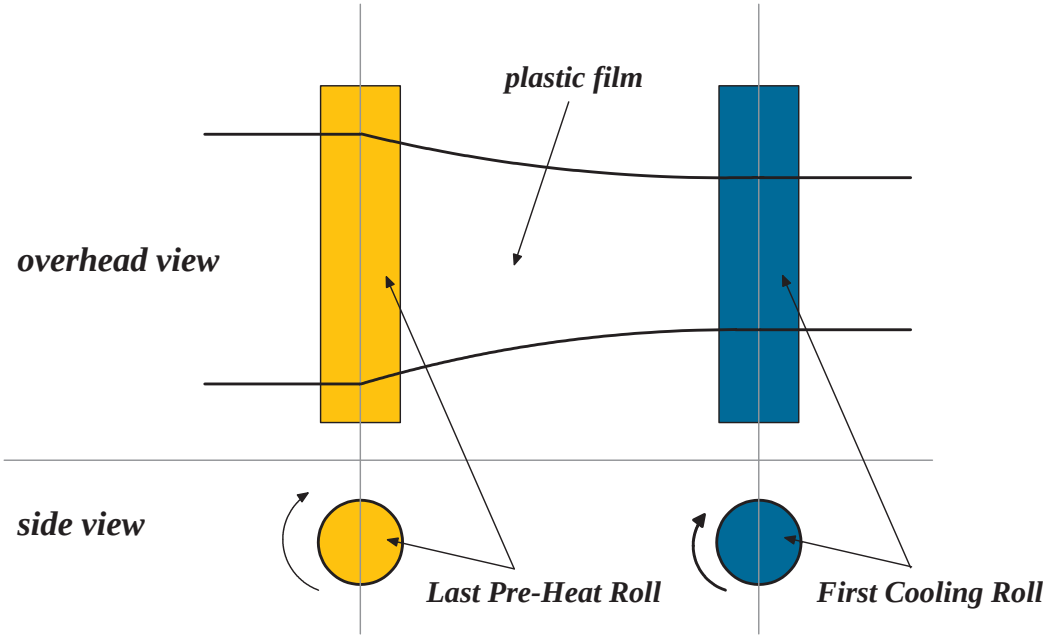

FIGURE 2.8: Neck-in during forward-draw

pre-heat rolls, which increase the temperature of the cast film to 15°C above its glass transition temperature (MacDonald, 2007), where the cast film can be more readily stretched. As depicted in Figure 2.7, the slow-nip rolls prior to the pre-heat rolls and the fast-nip rolls posterior to cooling rolls nip the cast film and the speed difference between the slow and fast-nip rolls causes the cast film to stretch in the MD. Once the film has been stretched, the temperature is brought below the glass transition temperature to avoid further crystallisation, which can make the film more brittle and cause film breakage later in the process.

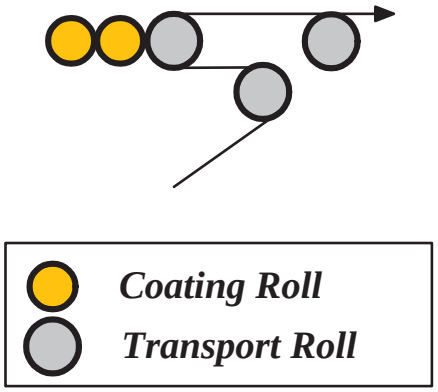

FIGURE 2.9: Coaters; Single-side coating

Stretching the film in the MD at crystallisation temperature – above the glass transition temperature and below the melting temperature – causes orientation or alignment of polymeric molecular chains in the MD. The alignment of molecular chains increases Young's modulus and tensile strength by a factor proportional to the stretch ratio, which is approximately 3.5 to 1.

As the film is stretched in the MD, the width of the film decreases as depicted in Figure 2.8 causing the edges to become thicker than the other regions of the film. This phenomenon is referred to as neck-in as introduced in Section 2.4. As this thickness variation can be amplified later in the process, CD control to minimise the thickness variation across the width of the film can become more complex and challenging.

2.6 Coating

There exist several methods for coating the film. Examples of single and double-side coating (Glawe, 2009) are depicted in Figures 2.9 and 2.10, respectively. Each outer coating roll of the pairs shown in the figures is partially submerged in a tray filled with coating material, where the tray is fed the coating material via a pump from a small stock tank. By continuously rotating the outer coating rolls of the pairs, the inner coating rolls corotate deploying a thin layer of the coating material onto the film. Each pair in Figure 2.10 deploys the coating material onto

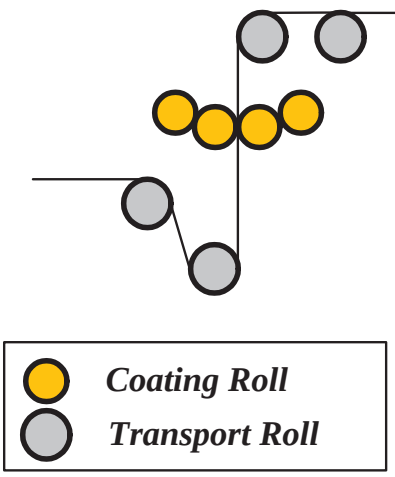

FIGURE 2.10: Coaters; Double-side coating

a different side of the plastic film whereas the pair in Figure 2.9 can deploy the material onto one side only.

The coating material usually consists of a large portion of water and a small portion of coating substance. The water contained in the coating material needs to be removed from the film surfaces by evaporation, which is carried out in the stenter oven. Furthermore, the rotation speed of the coating rolls needs to be kept constant as the speed variation can lead to temperature and thickness variation of the film later in the process.

2.7 Stenter Oven

The stenter oven includes five stages, each performing a different task, as follows:

1. Pre-heat stage
2. Sideways-draw stage
3. Buffer stage
4. Crystallisation stage
5. Cooling stage

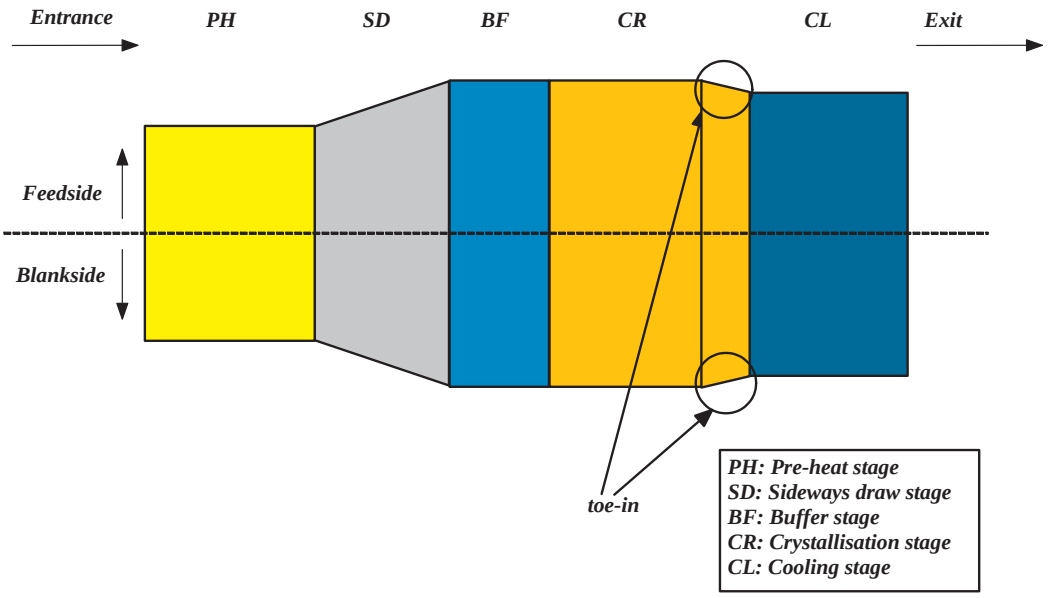

FIGURE 2.11: The overhead view of stenter oven

Figure 2.11 depicts the overhead view of the stenter oven. As the film enters the stenter oven, the pre-heat stage brings the film temperature above its glass transition temperature, where the film can readily be stretched. The temperature can be increased by releasing hot air from the nozzles located at the top and bottom of the stenter oven.

During the second stage of the stenter oven, the edges of the film are clipped and led along diverging rails causing the film to stretch in the CD as shown in Figure 2.11. This causes alignments of some molecular chains in the CD to a point where the alignments approximately balance those in the MD formed during the forward-draw stage. The stretch ratio of the sideways-draw is close to that of the forward-draw and is approximately 3.5 to 1. Moreover, this stage aligns the molecular chains that have not already aligned in the MD and some of those which have already aligned in the MD towards the CD (MacDonald, 2007). They in turn increase Young's modulus and tensile strength in the CD by a factor proportional to the stretch ratio. The temperature at this stage is higher than the temperature at the forward-draw stage because the glass transition temperature increases as crystallinity increases. Furthermore, the thicker regions of the film, caused by neck-in during the casting and forward-draw stages, tend to stretch less than the thinner regions adding another complexity to the process.

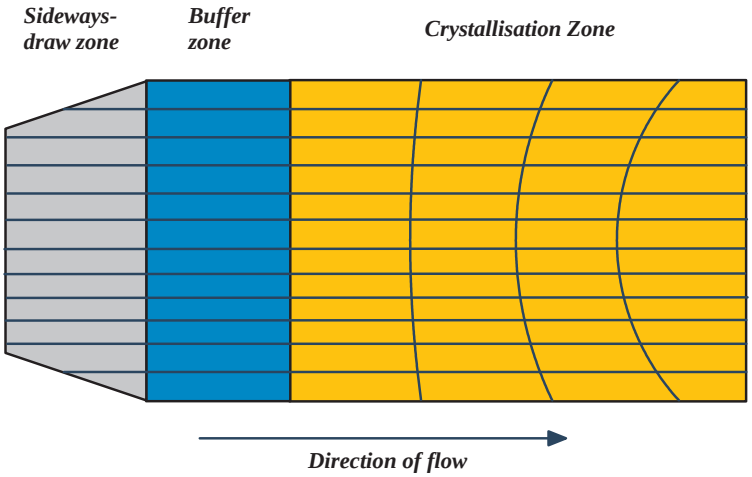

FIGURE 2.12: Bowing

0-15% of molecular chains align in the MD during the forward-draw stage and 25-35% of the molecular chains align in the CD and MD during the sideways-draw stage (Looney et al., 2005).

The temperature of the buffer stage is designed to be close to that of the sideways-draw stage. This stage acts as an insulator as there exists a significant temperature difference between the sideways-draw and crystallisation stages.

During the crystallisation stage, the temperature of the film is brought to temperature (usually higher than 200°C) above the glass transition temperature (80°C) and below the melting temperature (260°C). Although the residence time may only be a few seconds, a considerable rise in crystallinity occurs. At this stage, approximately 50% of the molecular chains are usually aligned in the MD and CD.

Another phenomenon that occurs during the crystallisation stage is bowing, in which if a CD straight line was drawn on the film at the end of the sideways-draw stage, this line would have a curvature towards the exit of the stenter oven as shown in Figure 2.12. This is because non-crystalline regions of the film experience significant molecular relaxation causing the CD centre of the film to shrink back towards the sideways-draw stage while the edges are constrained by the clips.

The width of the film decreases during the crystallisation stage by employing converging rails as shown in Figure 2.11. By decreasing the width of the film,

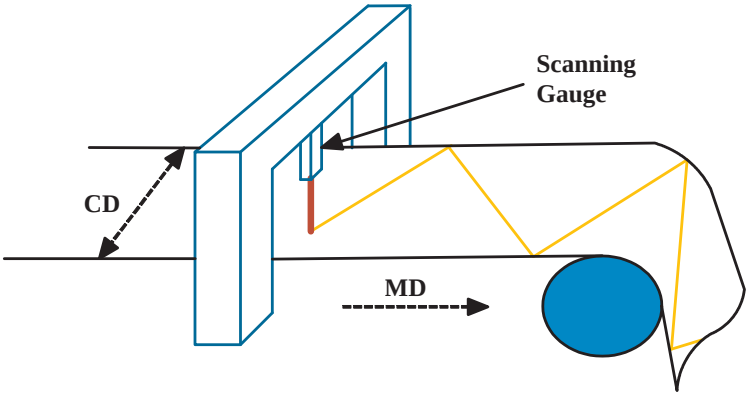

FIGURE 2.13: Scanning gauge

the stress formed during the preceding stages is relaxed, thereby improving the dimensional stability of the film at high temperature. This method of decreasing the width of the film is known as toe-in.

The cooling stage allows the film some time at temperature below the glass transition temperature to strengthen the alignments of polymeric molecular chains formed during the forward and sideways-draw stages and the crystallisation stage. The crystallisation and cooling stages together are often referred to as annealing.

In order to control the temperature of the stenter oven at different stages more efficiently, over and above the classification of the stenter oven into the five stages, each stage is classified into zones. Each zone is further divided into feedside and blankside each with a different temperature controlling system as shown in Figure 2.11. As a result, each stage employs a number of independent temperature controlling systems. Furthermore, in order to avoid thickness variation in the MD, the stenter oven is speed-controlled. The speed of stenter oven needs to be kept the same as that of the fast-nip rolls to avoid unwanted stretching of the film.

2.8 Scanning Gauge and Winding

As the film exits the stenter oven, a scanning gauge traverses across the moving film measuring the CD thickness profile. Since the film keeps moving in the

MD and the scanning gauge traverses across the CD, the resulting measurements are not in a straight CD line but in a zigzag pattern. These measurements are signalled back to the actuators at the die-lip gap to provide correction to local melt flow rate, hence the thickness profile. CD control is a main topic of this thesis and is discussed in Chapter 5.

The edges of the film at this stage are thicker than the other regions mainly due to neck-in, which occurs during the casting and forward-draw stages. For the film to be wound into a large mill roll properly, the thicker edges are slit prior to the winding stage. The edges are reclaimed for reprocessing into a film and combined with fresh polymers at the start of the process as described in Section 2.1. These edge trimmed films are then wound into a mill roll of approximately 4 to 8m in width. The average thickness in the CD depends on the type of film being produced but can range from 50 to 300 microns.

2.9 Summary

This chapter has described the plastic film manufacturing process for producing biaxially oriented plastic films such as biaxially oriented PET and PEN films. The overall process looks close to the one depicted in Figure 2.14. Focuses are on the main stages of the process adopted by DTF, which are preparation, extrusion, filter and die, casting, forward-draw, coating, stenter oven, and scanning gauge and winding. Each stage of the process is described in detail with figures for clear presentation. Difficulties and complexities associated with every stage are also presented. This chapter is essential as one of the main topics of this thesis is modelling of the process, which follows in Chapter 3.

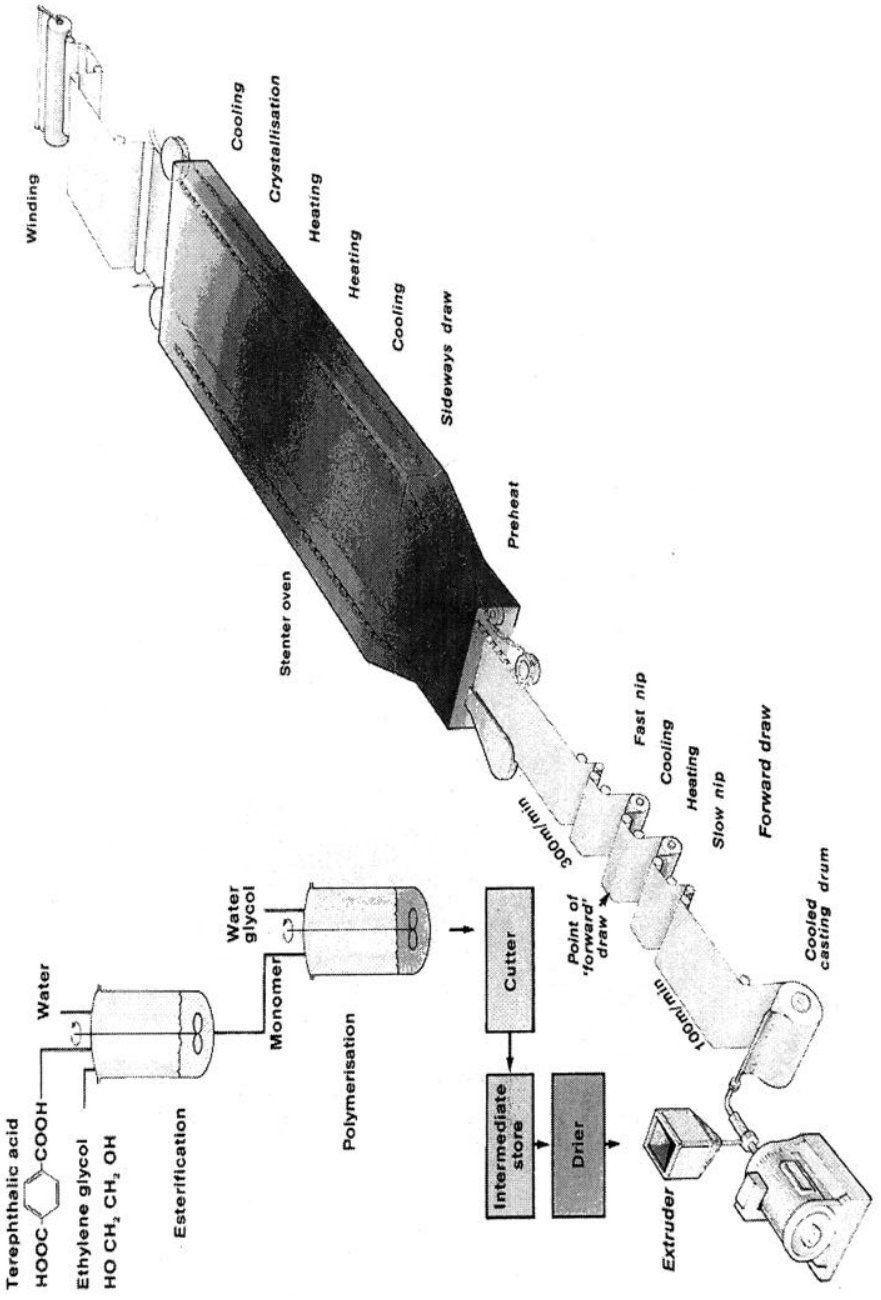

FIGURE 2.14: Plastic film manufacturing process; provided by DuPont Teijin Films Ltd

Chapter 3

First-principles Modelling

This chapter presents the development of a first-principles model of the plastic film manufacturing process reported in Chapter 2. Some progress has been made in the first-principles modelling of plastic film manufacturing processes (Featherstone et al., 2000; Kanai and Campbell, 1999; Pirkle and Braatz, 2003), but these models are still very rare as the first-principles modelling of a large-scale process is often regarded as complex and time consuming. However, when such a model becomes available, it can bring many benefits.

Most model-based control and fault monitoring algorithms, such as various types of observers, parity relations, Kalman filters, and internal model control (IMC), require a state-space or transfer function model identified from the plant using a system identification technique (Featherstone et al., 2000; Gorinevsky and Gheorghe, 2003). By employing a first-principles model to simulate the plant, system identification experiments can be applied to the model as opposed to the plant, enabling shorter and more flexible identification experiments leading to less wasted product. The model also allows new and existing control and fault monitoring algorithms to be tested without wasting product, and by adding disturbances and faults, realistic scenarios where faults and disturbances are present can be simulated without the need for experiments on the real-life process (plant). Moreover, the model would be useful for tuning the process and training the plant operators and allow for the determination of the optimal design, position, and spacing of sensors and actuators (Jai and Pritchard, 1987; VanAntwerp et al., 2007).

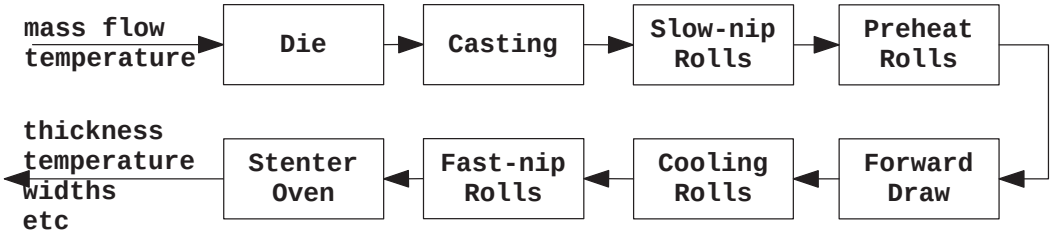

FIGURE 3.1: Process flow diagram

The model developed in this chapter is large-scale and based on the first-principles of chemical and mechanical engineering such mass transfer, heat transfer, flow of viscous fluid, and deformation in addition to empirical knowledge related to the behaviour of polymer. Incorporating as many phenomena as possible into the model would increase the accuracy of the model, but at the same time, it would make the model become over-complex and thus impractical. Therefore, the model has been developed to be as simple as possible while ensuring that all the important phenomena required to achieve the objectives of this thesis are captured.

This chapter starts with presenting key modelling assumptions in Section 3.1 which summarises modelled and neglected phenomena. Furthermore, the section points out what the inputs, outputs, and disturbances are for each unit operation. Sections 3.2 and 3.3 introduce the mass and heat transfer modules (or sub-models), which are common to all the unit operations except die. The following sections describe how these modules can be incorporated into each unit operation, and Section 3.10 summarises this chapter.

3.1 Key Modelling Assumptions

For modelling purposes, the process is decomposed into a series of unit operations as depicted in Figure 3.1. Within each of these unit operations except for die, the film is meshed in the MD (x-direction) and CD (y-direction) using a uniform rectangular mesh as shown in Figure 3.2. The film is divided into 4 CD sections in the figure for brevity, but the number can be much higher. The mass transfer, heat transfer, and deformation modules are subsequently formulated for each unit

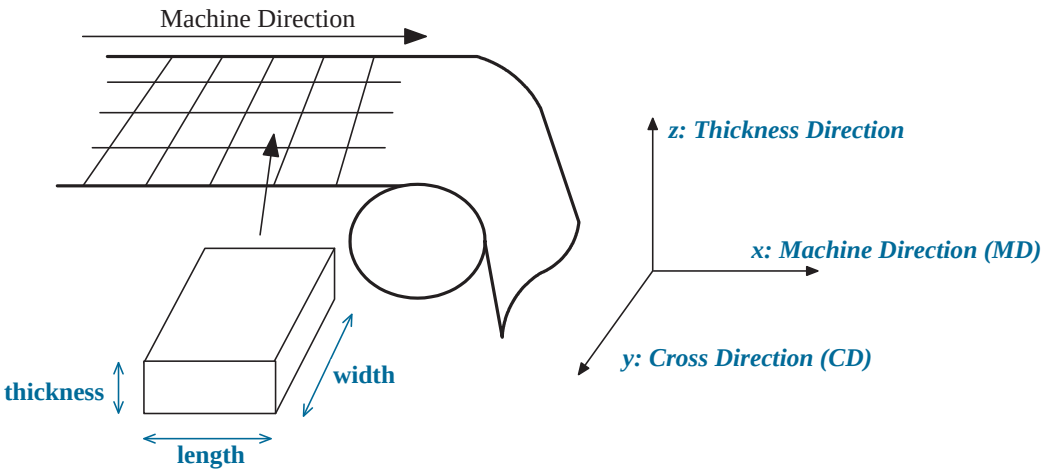

FIGURE 3.2: Film mesh and orientation

operation and fitted to the mesh. The film orientation is also shown in the figure and can be summarised as follows:

- x-axis
  - Machine direction (MD)
  - Positive in the direction of flow (i.e., from die to stenter oven)
- y-axis
  - Cross direction (CD)
  - Positive direction from feed-side (the side of die through which the polymer is fed) to blank-side
- z-axis
  - Thickness direction
  - Positive direction from bottom to top

Although the heat and mass transfer modules are common to every unit operation except for die, deformation modules are incorporated into the casting drum, forward-draw, and sideways-draw unit operations only – each deformation module is unique. The die unit operation, however, is modelled using none of the heat

transfer, mass transfer, and deformation modules. Instead, the flow of viscous fluid (i.e., polymer) and the actuator movements are modelled as presented in Section 3.4.

The resulting model of the process consists of a number of smaller models, one for each unit operation, such as die model, casting model, forward-draw model, and sideways-draw model. Each of these smaller models is composed of one or more modules, such as mass and heat transfer modules.

Finally, for the purpose of this thesis:

- A parameter is defined as a quantity which is already present and cannot vary during a simulation such as the total width (before and after stretching), heat transfer coefficient, stretch ratio, and conductivity – see Appendix A
- An input variable or input is a quantity which can vary during a simulation such as the width in each CD section, process speed, input mass flow rate, and input temperature – see Table 4.1

3.2 Mass Transfer Module

In order to capture the dynamic variation in film thickness throughout the process, the mass per unit area, known as basis weight (W in kg/m^2), of the film at

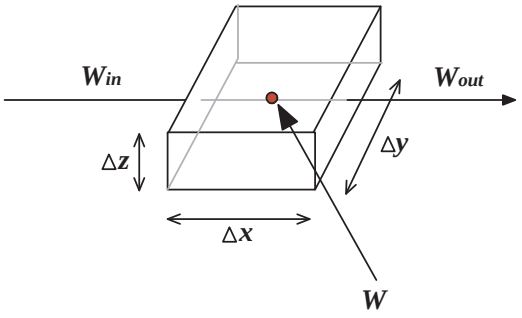

FIGURE 3.3: Mass transfer

positions along the MD and CD of the film path can be tracked. The derivation of the rate of basis weight change (in kg/m^2s) is thus presented here.

Figure 3.3 depicts a box extracted from the mesh shown in Figure 3.2. As depicted in the figure, it is assumed that the basis weight of the 3D box is the basis weight of the centre of the box. Tracking the basis weight variation throughout the process is equivalent to tracking the thickness variation as thickness can readily be derived from basis weight – basis weight (in kg/m^2) divided by density (in kg/m^3) equals thickness (Δz in m).

Taking account of the law of mass conservation and assuming that the film travels in the MD only, the following equation can be derived (Coulson and Richardson, 1999; Incropera et al., 2007; Lydersen, 1983):

$$\frac{\partial m}{\partial t} = \dot{m}_{in} - \dot{m}_{out} \tag{3.1}$$

where $\dot{m}$ denotes mass flow rate (in kg/s).

The linear relationship between mass (m in kg) and basis weight is

$$m = W\Delta x\Delta y \tag{3.2}$$

where Δx and Δy respectively denote the length and the width of a box as shown in Figure 3.3.

Dividing both sides by time, the equations for the input and output mass flow rates are

$$\dot{m}_{in} = W_{out}v\Delta y \tag{3.3}$$

$$\dot{m}_{out} = W_{in}v\Delta y \tag{3.4}$$

Substituting Equations 3.2, 3.3, and 3.4 into Equation 3.1 yields

$$\Delta x\Delta y\frac{\partial W}{\partial t} = W_{in}v\Delta y - W_{out}v\Delta y \tag{3.5}$$

Furthermore, the following equations can be derived from Figure 3.3:

$$W_{in} = W + 0.5\frac{\partial W}{\partial x}\Delta x \tag{3.6}$$

$$W_{out} = W - 0.5\frac{\partial W}{\partial x}\Delta x \tag{3.7}$$

Substituting Equations 3.6 and 3.7 into 3.5 yields

$$\begin{aligned}\Delta x\Delta y\frac{\partial W}{\partial t} &= (W - \frac{\partial W}{2\partial x}\Delta x)v\Delta y - (W + \frac{\partial W}{2\partial x}\Delta x)v\Delta y \\ &= -v\Delta y\Delta x\frac{\partial W}{\partial x}\end{aligned} \tag{3.8}$$

Hence,

$$\frac{\partial W}{\partial t} = -v\frac{\partial W}{\partial x} \tag{3.9}$$

By discretising Equation 3.9, the mass at position $(i\Delta x, j\Delta y)$ of the mesh is governed by the following differential equation:

$$\frac{\partial W_{i,j}}{\partial t} = -v\frac{W_{i,j} - W_{i-1,j}}{\Delta x} \tag{3.10}$$

Finally, the mass transfer module described by Equation 3.10 computes for $W_{i,j}$ from its previous value $W_{i-1,j}$ taking account of the process speed (v) and the step size (Δx).

3.3 Heat Transfer Module

There are three different types of heat transfer as follows (Janna, 2000; Nellis and Klein, 2008; Skogestad, 2008):

1. Conductive heat transfer
2. Convective heat transfer
    - Natural convection

- Forced convection

3. Radiation heat transfer

Conductive heat transfer can be defined as the transition of heat energy from a region of higher temperature to that of lower temperature through direct molecular communication within a medium or between mediums in direct physical contact without a flow of the material medium. Convection heat transfer, on the other hand, can be defined as the transition of heat energy by fluid movement within a medium or between a medium and the neighbouring fluid. For natural convection, the fluid surrounding a heat source receives heat and cooler fluid in turn moves towards the heat source. In contrast, forced convection occurs when fluid is propelled artificially by the likes of a pump or a fan. In common usage, "fluid" is often used as a synonym for "liquid", but in physics, fluid includes gas (or air) as well as liquid (Coulson and Richardson, 1999). This thesis also considers air as fluid and therefore heat transition from air to polymer is also defined as natural convection. Finally, radiation can be defined as the transition of heat energy through radiation.

For modelling purposes, it is assumed that there is no heat transfer in y-direction. Every type of heat transfer occurs in z-direction and only forced convective heat transfer takes place in x-direction. The underlying expressions describing these types of heat transfer can be summarised as follows.

3.3.1 Natural Convective Heat Transfer and Conductive Heat Transfer

$$Q = hA\Delta T \tag{3.11}$$

where Q denotes heat transfer (in W or J/s), h heat transfer coefficient (in W/m^2K), A cross sectional surface area (in m^2), and T temperature (in K). Heat transfer coefficient from air to polymer is different from that from water to roll, and they further vary throughout the process as summarised in Appendix A.

For conductive heat transfer, h is replaced by k/L, where k denotes material conductivity (in W/mK), and d is the distance of heat transition.

3.3.2 Forced Convective Heat Transfer

$$Q = \dot{m} C_p \Delta T \tag{3.12}$$

where $\dot{m}$ and C_p denote mass transfer (in kg/s) and specific heat capacity (in $J/kg/K$ or $J/kg/°C$), respectively. Specific heat capacity of PET polymer at and below its glass transition temperature is 1300 $J/kg/°C$; otherwise, the following equation can be applied (DTF, 2007b):

$$C_p = C_{p,a}(T)(1 - M_c) + C_{p,c}(T) M_c \tag{3.13}$$

where M_c denotes mass fraction crystalline, which varies through the process depending on crystallinity and is summarised in Appendix A. Amorphous and crystalline heat specific capacity, $C_{p,a}(T)$ and $C_{p,c}(T)$ (in $J/kg/°C$) are dependent on temperature, T and given by

$$C_{p,a}(T) = \kappa_1 + \psi_1 T \tag{3.14}$$

$$C_{p,c}(T) = \kappa_2 + \psi_2 T \tag{3.15}$$

where κ_1, κ_2, ψ_1, and ψ_2 are some constants, which cannot be shown due to confidentiality reasons.

3.3.3 Radiation Heat Transfer

$$Q = \epsilon \sigma A (T_1^4 - T_2^4) \tag{3.16}$$

where ϵ denotes the emissivity ($0 \leq \epsilon \leq 1$) of polymer, and σ refers to the Stefan-Boltzmann constant (in W/m^2K^2).

3.3.4 Relation between Heat Transfer and Temperature Changes

In order to capture the variation in temperature throughout the process, the temperature of the film at positions along the MD and CD of the film path can be tracked. Consequently, the derivation of the rate of temperature change is presented here.

Figure 3.4 represents a box extracted from the mesh shown in Figure 3.2. As depicted in the figure, it is assumed that the temperature of the 3D box is the temperature of the centre of the box. For each box in the figure, Equations 3.11, 3.12, and 3.16 can be related to the following heat energy equation (Coulson and Richardson, 1999; Holman, 2001):

$$Q = C_p m \frac{\partial T}{\partial t} \tag{3.17}$$

As shown in Figure 3.5, a side of the polymer film is either exposed to air or in contact with the roll surface which may contain water or air. Taking account of the law of energy conservation, Equation 3.17 can be related to Equations 3.11, 3.12, and 3.16 as follow:

$$C_p m \frac{\partial T}{\partial t} = Q_{mt} + Q_{sp} + Q_{wp} \tag{3.18}$$

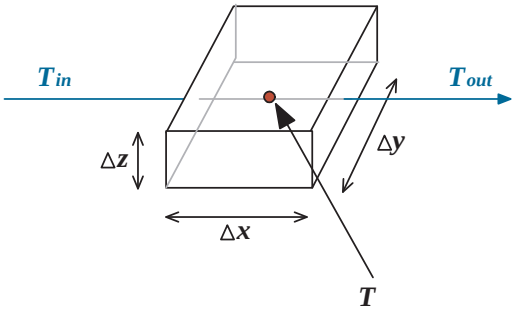

FIGURE 3.4: Heat transfer

where Q_{mt} denotes forced convective heat transfer in the MD (x-axis), Q_{wp} is heat transfer from the water inside the roll to polymer, Q_{sp} refers to heat transfer from the surrounding air to polymer.

Q_{mt}, Q_{wp}, and Q_{sp} can be computed as follows: Since Q_{mt} is forced convective heat transfer, Equation 3.12 is employed to find Q_{mt} such that

$$Q_{mt} = \dot{m} C_p (T_{in} - T_{out}) \tag{3.19}$$

Similarly to Equations 3.6 and 3.7, T_{in} and T_{out} can be defined as

$$T_{in} = T - 0.5 \frac{\partial T}{\partial x} \Delta x \tag{3.20}$$

$$T_{out} = T + 0.5 \frac{\partial T}{\partial x} \Delta x \tag{3.21}$$

By substituting T_{in} and T_{out} in Equations 3.20 and 3.21 and $\dot{m}$ in Equation 3.3 into Equation 3.19, the following equation for Q_{mt} can be obtained:

$$Q_{mt} = -W C_p v \Delta x \Delta y \frac{\partial T}{\partial x} \tag{3.22}$$

Heat transfer from the surrounding air to polymer may involve radiation heat transfer as well as heat transfer by air-flow (i.e., natural convection). Both Equations 3.11 and 3.16 are thus employed to give

$$Q_{sp} = \epsilon \sigma A (T_s^4 - T_p^4) + h_{sp} A (T_s - T_p) \tag{3.23}$$

where h_{sp} represents the heat transfer coefficient (W/m^2K) from the surrounding air to polymer, which varies throughout the process as summarised in Appendix A. For instance, heat transfer within the stenter oven is mainly carried out by blowing hot or cold air onto the surfaces of the film, and in such a case, only the second term of the equation is used.

Since heat transfer from the water inside the roll to polymer involves natural convection and conduction, Equation 3.11 is employed to find Q_{wp} as

$$Q_{wp} = h_{wp} A (T_w - T_p) \tag{3.24}$$

where T_w and T_p denote the temperatures of water and polymer, respectively, h_{wp} refers to the heat transfer coefficient (in W/m^2K) from water to polymer, which varies throughout the process, and the area (A) is given by $\Delta x \Delta y$.

h_{sp} in Equation 3.23 can be calculated referring to Figure 3.5 as follow (Incropera et al., 2007):

$$\frac{1}{h_{sp}} = \frac{1}{h_{isp}} + \frac{1}{k_p/(d_p/2)} \tag{3.25}$$

where k_p represents the conductivity (in W/Km) of polymer, d_p is the polymer thickness, and h_{isp} denotes the heat transfer coefficient from the surrounding air to roll surface.

The first term is responsible for heat transfer from the surrounding air to polymer, and the second term is for heat transfer within the half thickness of the polymer. The half thickness ($d_p/2$) is used because the heat transfer coefficient from the surrounding air to the centre of polymer (in the thickness direction) is needed. In this manner, h_{wp} in Equation 3.24 can also be calculated as follows:

$$\frac{1}{h_{wp}} = \frac{1}{h_{irp}} + \frac{1}{h_{iwr}} + \frac{1}{k_p/(d_p/2)} + \frac{1}{k_r/d_r} \tag{3.26}$$

where h_{irp} denotes the heat transfer coefficient from roll surface to polymer, h_{iwr} is the heat transfer coefficient from water to roll surface, and k_r represents the conductivity of the roll surface.

By substituting Equations 3.22, 3.23, and 3.24 into Equation 3.18, the following can be obtained:

$$\begin{aligned} C_p m \frac{\partial T}{\partial t} = &- W C_p v \Delta x \Delta y \frac{\partial T}{\partial x} + h_{wp} A (T_w - T_p) \\ &+ \epsilon \sigma A (T_s^4 - T_p^4) + h_{sp} A (T_s - T_p) \end{aligned} \tag{3.27}$$

Then, substituting Equation 3.2 into Equation 3.27 yields the following equation for the heat transfer module:

$$\frac{\partial T}{\partial t} = -v \frac{\partial T}{\partial x} + \frac{h_{wp}(T_w - T_p)}{C_p W} + \frac{\epsilon \sigma (T_s^4 - T_p^4)}{C_p W} + \frac{h_{sp}(T_s - T_p)}{C_p W} \tag{3.28}$$

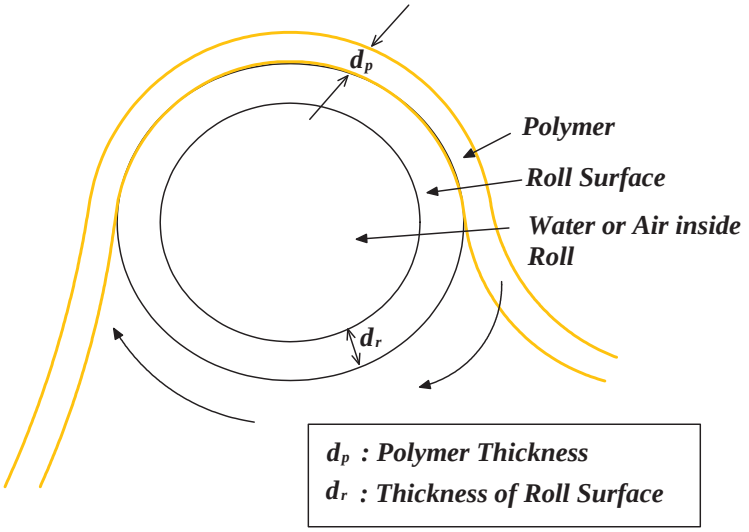

FIGURE 3.5: Film in contact with a roll

Finally, by discretising Equation 3.28, the temperature at position $(i\Delta x, j\Delta y)$ of the mesh (Figure 3.2) is governed by the following differential equation:

$$\begin{aligned}\frac{\partial T_{i,j}}{\partial t} &= -v\frac{T_{i,j} - T_{i-1,j}}{\Delta x} + \frac{h_{wp}(T_{w,i,j} - T_{p,i,j})}{C_p W_{i,j}} \\ &+ \frac{\epsilon\sigma(T^4_{s,i,j} - T^4_{p,i,j})}{C_p W_{i,j}} + \frac{h_{sp}(T_{s,i,j} - T_{p,i,j})}{C_p W_{i,j}}\end{aligned} \tag{3.29}$$

The heat transfer module described by Equation 3.29 computes for $T_{i,j}$ from its previous value $T_{i-1,j}$ taking account of a number of model parameters including the heat transfer coefficients, air temperature, water temperature, heat capacity, emissivity, and the geometry of the unit operation over and above the model inputs such as the process speed and basis weight, which can be tracked using the mass transfer module described by Equation 3.10.

3.4 Die

The geometry used for the die model is depicted in Figure 3.6. For modelling purposes, the front view of the die is simplified and re-drawn in 2-dimension in Figure 3.7. Polymer is fed into the die through "Input section/Body row" (feed

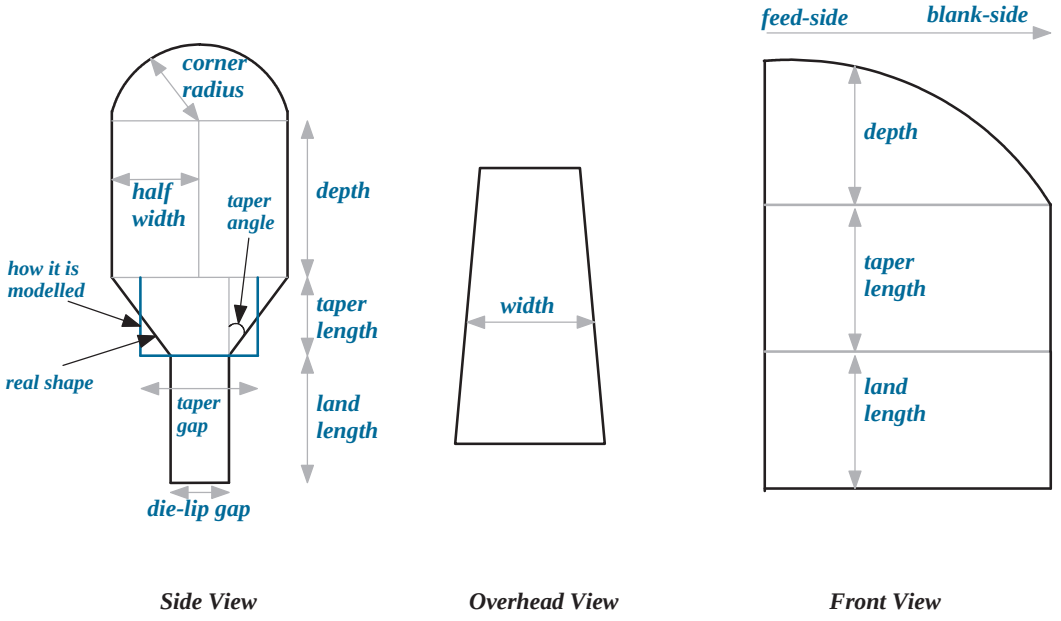

FIGURE 3.6: Die geometry

side) and flows out of the die through the output row (die-lip gap). For brevity, the die is divided into 5 CD sections, but the number can be much higher up to 49, which is the number of die bolt heaters (actuators) employed in real life. The die is viewed as being comprised of a set of interconnected pipes that form a flow mesh as shown in Figure 3.7. Therefore, the die model in the figure comprises a number of square cells, and the mathematics used for the die model relies on the following assumptions (DTF, 2006a):

1. Flow travels only horizontally and vertically in the body row
2. Flow travels only vertically through the others

The die model requires mass flow rate (in kg/s) as the only input and produces the mass flow rate (in kg/s) for each CD section for the output row. Furthermore, pressure (P in Pa) at the inlet (Input section/Body row) is also calculated and can be employed to validate the die model as discussed in Chapter 4. The underlying equations used for the die model are as follows.

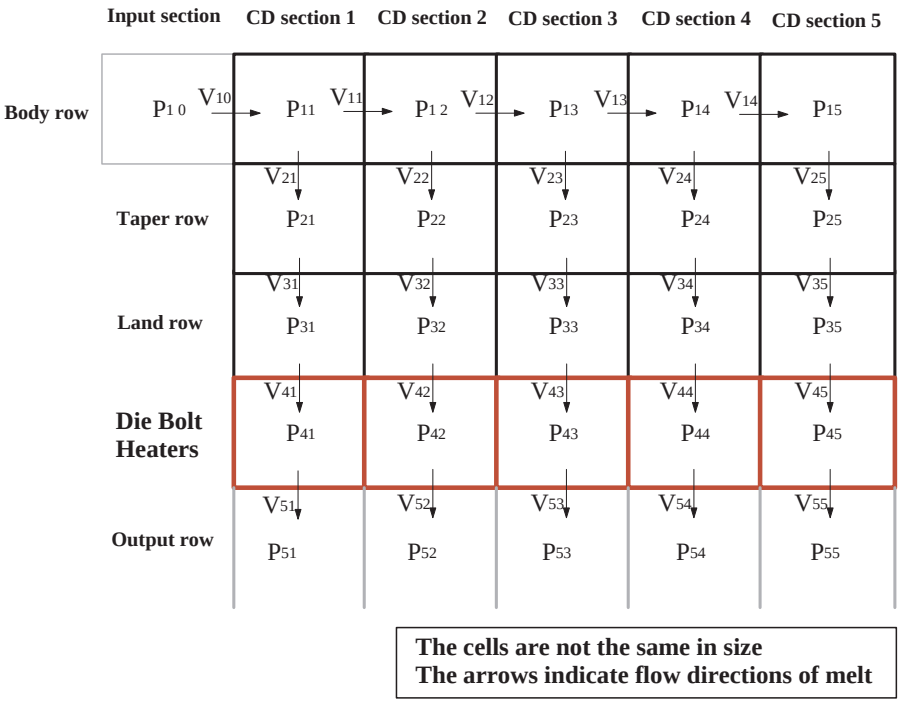

FIGURE 3.7: Die in 2D

3.4.1 Horizontal Flow

The following equation that is a modification of Poiseuille's equation for laminar horizontal flow in a circular pipe is used to mathematically describe the flow in the body row depicted in Figure 3.7 (DTF, 2006a):

$$P_{i,j+1} - P_{i,j} = \frac{\mu(3 + X_j)(1 + \sqrt{X_j})}{H_j^2 A_{i,j}} V_{i,j+1} \tag{3.30}$$

where subscripts i and j denote row and column respectively, V represents volumetric flow (in m^3/s), μ is the polymer viscosity, H_j refers to the half-width at position j along the die body as shown in Figure 3.6, and A is the cross-directional area. X is given by

$$X_j = \frac{2H_j}{w_j + H_j} \tag{3.31}$$

where w_j is the greater of the depth and the half-width at position j along the die body row.

3.4.2 Vertical Flow

The flow within the other rows of the die are modelled as parallel flow using Poiseuille's equation for flow between two plates as follows (Sutera and Skalak, 1993; Tucker, 1989):

$$P_{i+1,j} - P_{i,j} = \frac{3\mu L_{i,j}}{g_{i,j}^2 A_{i,j}} V_{i+1,j} \tag{3.32}$$

where L denotes the taper or land length, and g represents the taper or die-lip gap.

3.4.3 Die Bolt Heaters

As the polymer melt is discharged through the die-lip gap, additional heat is transmitted to the polymer from the die bolt heaters mounted across the width of the die-lip gap. Increasing the set-point of a heater decreases the viscosity of the local polymer, thereby increasing the local thickness formed on the surface of the casting drum, or vice versa. The actuator set-points are determined by the CD controller, taking account of the measured CD thickness profile of finished product ($\mathbf{y} \in \mathbb{R}^M$) such that the CD thickness profile of finished product remains as flat as possible (Chapter 5).

The effect of die bolt heaters can be empirically modelled as

$$V_{i,j} = \frac{P_{i,j} - P_{i-1,j}}{f_j} \tag{3.33}$$

for $i = 5$, where f_j denotes the viscosity factor at position j along the row. The equation implies that the volumetric flow increases as the viscosity factor decreases, or vice versa.

The viscosity factor, $\mathbf{f}$ is then given by the following equation:

$$\mathbf{f} = k_g \mathbf{G}_r \mathbf{u} \tag{3.34}$$

where $\mathbf{u} \in \mathbb{R}^N$ denotes the actuator set-points, k_g is the scalar gain, and $\mathbf{G}_r$ represents the $(M \times N)$ interaction matrix representing the steady state spatial

response, which gives each die bolt heater the response of a Gaussian curve. By employing this interaction matrix, the die model simulates what happens in real life, that is, a single actuator affects not only the corresponding sensor measurements but also the neighbouring sensor measurements. The interaction matrix and k_g used to tune the die model are discussed in Section 4.2.

3.4.4 The Law of Mass Conservation

In addition to the equations used for vertical and horizontal flow and die bolt heaters, the die model utilises equations that can be derived from the law of mass conservation as follows.

For the body row (for $i = 1$), the following equation is employed:

$$V_{i+1,j} = V_{i,j-1} - V_{i,j} \tag{3.35}$$

for $j = 1, \cdots, N-1$, where N is the number of CD sections. For $j = N$, the last term on the right-hand side is zero.

For "Taper row", "Land row", "Die Bolt Heaters", and "Output row" (for $i = 2, 3, 4$) in Figure 3.7, the following equation is employed:

$$V_{i+1,j} = V_{i,j} \tag{3.36}$$

for each CD section $j = 1, \cdots, N$.

N equations from Equation 3.30, $3 \times N$ equations from Equation 3.32, $4 \times N$ equations from Equations 3.35 and 3.36, and N equations from Equation 3.33 can be obtained, hence $9 \times N$ equations in total. Unknowns are all P's and V's except $V_{1,0}$ and $P_{5,j}$ (for $j = 1, \ldots, N$) and add up to $9 \times N$ in total, too – $P_{5,j}$ (for $j = 1, \ldots, N$) is simply the atmospheric pressure (101 kPa). Consequently, all the unknowns can be calculated, and the die model can produce $V_{5,j}$ (for $j = 1, \cdots, N$) given the input, $V_{1,0}$. $P_{1,0}$, which is one of the unknowns that die model calculates, can be used to validate the die model as discussed in Chapter 4.

3.5 Casting Drum

When the polymer melt is discharged through the die-lip gap onto the surface of the casting drum, a thick film is formed. The thickness of this film is determined by the mass flow rate leaving the die-lip gap and the speed of the casting drum. In order to compute the mass per unit area deposited onto the casting drum at a position $j\Delta y$ along the width of the casting drum, the following equation can be used:

$$W_j(t) = \frac{\dot{m}_j}{v_{cd} w \eta_j} \tag{3.37}$$

where $\dot{m}_j$ denotes the mass flow rate (in kg/s) discharged through the die-lip gap at position j, v_{cd} represents the velocity of the casting drum, w denotes the film width, and $\boldsymbol{\eta} \in \mathbb{R}^M$ refers to the correction factor that compensates for the fact that the film shrinks in the width direction near the edges (i.e., neck-in introduced in Section 2.5). As a result, the section width decreases towards the edges from the centre.

The following equation can be used to derive $\dot{m}_j$ from the output (volumetric flow) of the die model:

$$\dot{m}_j = \rho V_{5,j} \tag{3.38}$$

where ρ denotes density (ρ in kg/m^3).

Equation 3.37 implies that the film thickness is determined by the mass flow rate leaving the die-lip gap, neck-in correction factor, and casting drum speed. Furthermore, Equation 3.37 is combined in series with the mass and heat transfer modules described in Sections 3.2 and 3.3 to form a casting drum model. The geometry required for the mass and heat transfer modules is depicted in Figure 3.8.

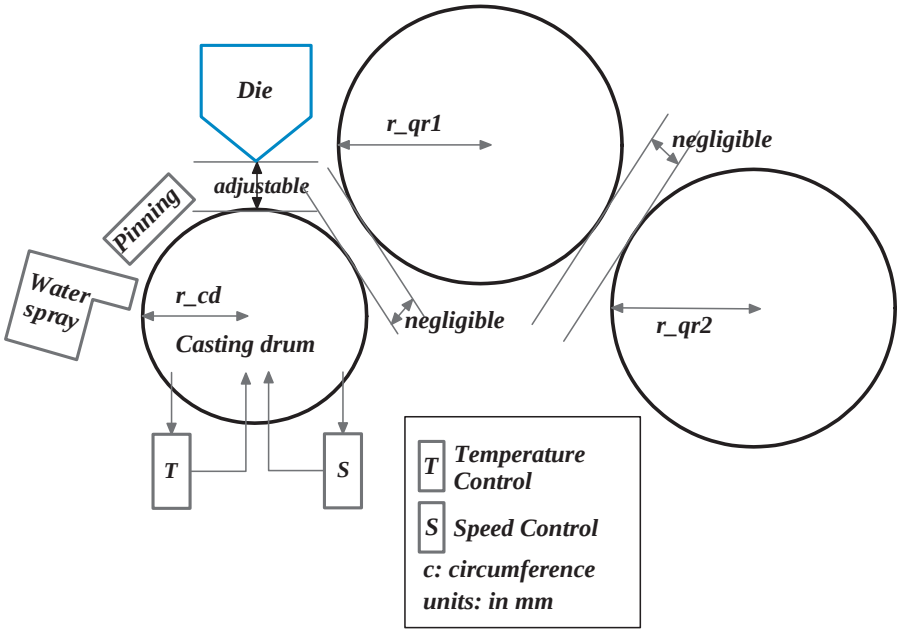

FIGURE 3.8: Die to casting - geometry

3.6 Pre-heat, Slow-nip, Fast-nip, and Cooling Rolls

These unit operations are modelled using the the mass and heat transfer modules described in Sections 3.2 and 3.3.

Additionally, in order to take account of the gaps between the rolls, it is assumed that the film takes off a roll at 3 o'clock position and lands on the next roll at 9 o'clock position as depicted in Figure 3.9. With this assumption, the following equations can be employed to compute the distances (d in m) between the rolls:

$$d = \sqrt{x_3^2 + x_5^2} \tag{3.39}$$

where $x_3 = x_1 - x_2 - x_4$. The equation is always valid regardless of the positions of the rolls.

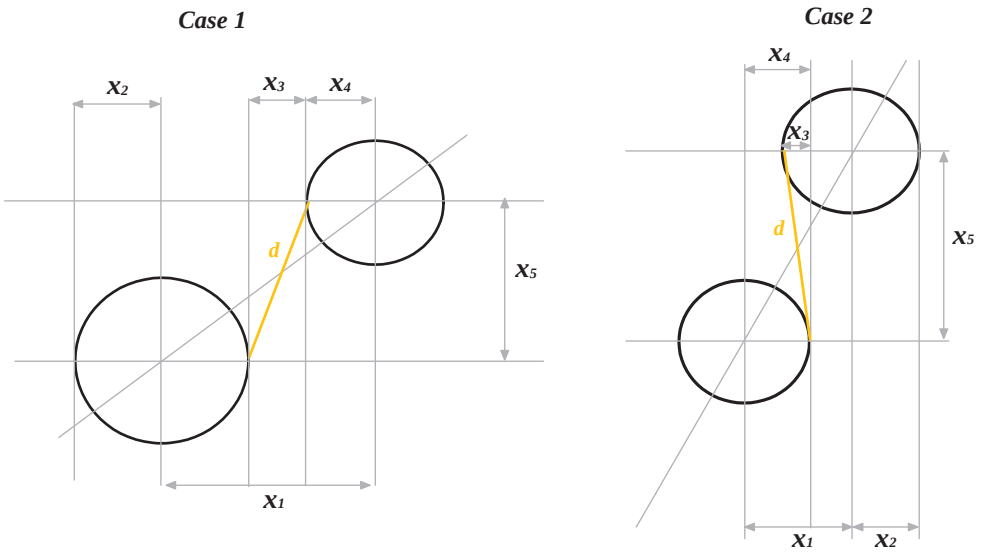

FIGURE 3.9: Geometry between rolls

3.7 Forward-draw

The speed difference between the sets of slow and fast-nip rolls causes the film to stretch in the MD as discussed in Section 2.5. As the film is stretched, the film tends to shrink in the CD, and this phenomenon (neck-in) was introduced in Section 2.4. Section 3.5 showed that neck-in also occurred as the polymer fell onto the casting drum through the die-lip gap. The edges of the film tend to shrink more than the centre, and the neck-in correction factor, which has been derived empirically based on laboratory experiments, is employed to take account of the phenomenon as

$$w_{u,j} = \eta_j w_{s,j} \tag{3.40}$$

where $w_{u,j}$ and $w_{s,j}$ respectively denote the width of the film in section j before and after the draw.

The mass flow rate in section j before ($\dot{m}_{u,j}$) and after ($\dot{m}_{s,j}$) the draw can be given by

$$\dot{m}_{u,j} = W_{u,j} v_{u,j} w_{u,j} \tag{3.41}$$

$$\dot{m}_{s,j} = W_{s,j} v_{s,j} w_{s,j} \tag{3.42}$$

where $W_{u,j}$ and $W_{s,j}$ denote the basis weights in section j before and after the draw, and v represents velocity.

Due to the law of mass conservation, the following equation needs to be satisfied (Hertzberg, 1996):

$$W_{u,j} v_{u,j} w_{u,j} = W_{s,j} v_{s,j} w_{s,j} \tag{3.43}$$

Taking account of neck-in described by Equation 3.40, the equation for the basis weight in section j can be derived as follows:

$$W_{s,j} = W_{u,j} \frac{v_{u,j}}{v_{s,j}} \eta_j \tag{3.44}$$

This deformation module calculates the basis weight of the film after the draw ($W_{s,j}$) based on the basis weight before the draw, taking account of the speeds before and after the draw and the neck-in correction factor. It is then combined with the mass and heat transfer modules described in Sections 3.2 and 3.3 to form a forward-draw model.

3.8 Coaters

Since the amount of coating material deployed on the surfaces of film is relatively small, the slight increase in the film thickness due to the coating material can be neglected. Therefore, the coaters are modelled simply by employing the mass and heat transfer modules described in Sections 3.2 and 3.3.

3.9 Stenter Oven

As described in Section 2.7, the stenter oven is composed of pre-heat, sideways-draw, buffer, crystallisation, and cooling stages. Apart from sideways-draw, these unit operations can be modelled using the mass and heat transfer modules.

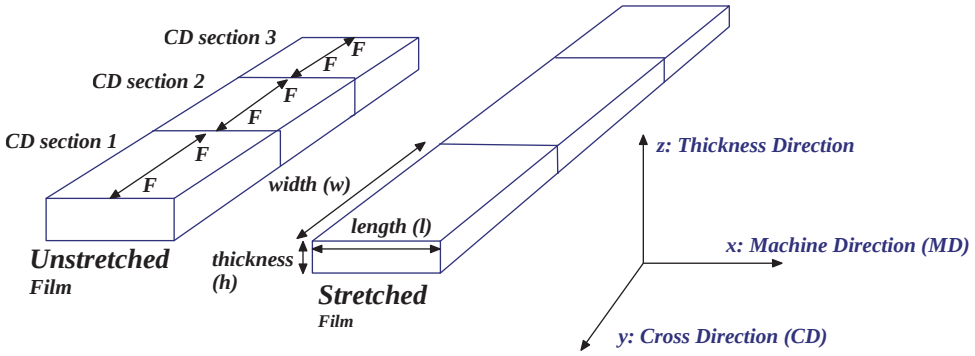

FIGURE 3.10: Sideways-draw

3.9.1 Sideways-draw

During this unit operation, the film stretches in the CD. The behaviour of the film during the draw depends on many factors including the process speed, temperature, and thickness. In order to develop a deformation model of this unit operation, a CD strip of the film is considered as shown in Figure 3.10. For brevity, the film strip depicted in the figure assumes that it is divided into three CD sections, but the number is higher in real life. Subsequently, the following simplifying assumptions are made:

1. The film stretches instantaneously.
2. The film stretches in the CD (width direction) only; therefore, the length (l or Δx in Figure 3.10) remains intact.

The figure illustrates the effect of CD stretching. It is important to observe that the un-stretched film is divided into sections with a uniform width but different thicknesses. The stretched film, on the other hand, exhibits non-uniform section widths and thicknesses. Since the same stretching force acts upon each section, thinner sections are more prone to stretch than thicker sections. Because the relationship between force and stretched width is a non-trivial function of many factors, exact predictions are difficult to make without resorting to mathematics.

In order to develop a mathematical model of the sideways-draw, the concept of strain (i.e., stretched width) needs to be introduced first. Strain (ϵ_j in %) can be

defined as (Hearn, 2001; Tucker, 1989)

$$\epsilon_j = \frac{\tilde{w}_j - w_j}{w_j} \tag{3.45}$$

where $\tilde{w}_j$ denotes the width of the stretched film in section j, and w_j is the width of the un-stretched film in section j.

Using Equation 3.45, the stretched width in each section ($\tilde{w}_j$) can be given as

$$\tilde{w}_j = w_j(\epsilon_j + 1) \tag{3.46}$$

Because every section of the un-stretched film has the same width, the equation can be re-written as follows:

$$\tilde{w}_j = \frac{w_T}{N}(\epsilon_j + 1) \tag{3.47}$$

where w_T is the total width of the un-stretched film such that

$$w_T = \sum_{j=1}^{N} w_j \tag{3.48}$$

The total width of the stretched film, $\tilde{w}_T$ can now be expressed as

$$\begin{aligned} \tilde{w}_T &= \sum_{j=1}^{N} \tilde{w}_j \\ &= \sum_{i=j}^{N} \frac{w_T}{N}(\epsilon_j + 1) \end{aligned} \tag{3.49}$$

where N denotes the number of CD sections. In this equation, the only unknowns are ϵ_j (for $j = 1, \ldots, N$) because $\tilde{w}_T$ and w_T are known.

Further, stress (σ in *bar*) applied on each CD section can be defined as follows (Balderud, 2004; Hertzberg, 1996):

$$\sigma_j = \frac{F}{A_{xz,j}} \tag{3.50}$$

where σ_j denotes the stress on section j, F is the force which is the same on every section, and $A_{xz,j}$ refers to the cross-sectional area ($l \times h$ in Figure 3.10).

Moreover, the following stress-strain equation, which has been derived empirically based on laboratory experiments (DTF, 2006b), provides stress given strain taking account of temperature, stretch rate, draw ratio, and draw speed as follows:

$$\sigma_j = C_1(1 - e^{-C_2\epsilon_j}) + C_3\epsilon_j^3 \tag{3.51}$$

C_k (for $k = 1, 2, 3$) is given by

$$C_k = \alpha_k - \beta_k T + \chi_k R \tag{3.52}$$

where α_k, β_k, and χ_k (for $k = 1, 2, 3$) are some constants, which cannot be shown due to confidentiality reasons, and R is given by

$$R = (\Lambda - 1) \times 100 v_{exit} \tag{3.53}$$

where Λ denotes the stretch ratio.

With all the parameters given in DTF (2006b), Equation 3.51 produces the response depicted in Figure 3.11. This response is known as stress-strain curve.

By combining Equations 3.50 and 3.51, N equations can be derived as follows:

$$\frac{F}{A_{xz,j}} = C_1(1 - e^{-C_2\epsilon_j}) + C_3\epsilon_j^3 \tag{3.54}$$

for $j = 1, \ldots, N$.

The unknowns are ϵ_j (for $j = 1, \ldots, N$) and F. Together with Equation 3.49, there are $N + 1$ equations for $N + 1$ unknowns, and the system of non-linear equations can be solved.

Due to the law of volume conservation (Hertzberg, 1996; Shames and Cozzarelli, 1992), the volume in each section before and after the draw must be the same such that

$$w_j l_j h_j = \tilde{w}_j \tilde{l}_j \tilde{h}_j \tag{3.55}$$

where l and h denote the length and thickness before the draw, and $\tilde{l}$ and $\tilde{h}$ represent the length and thickness after the draw.

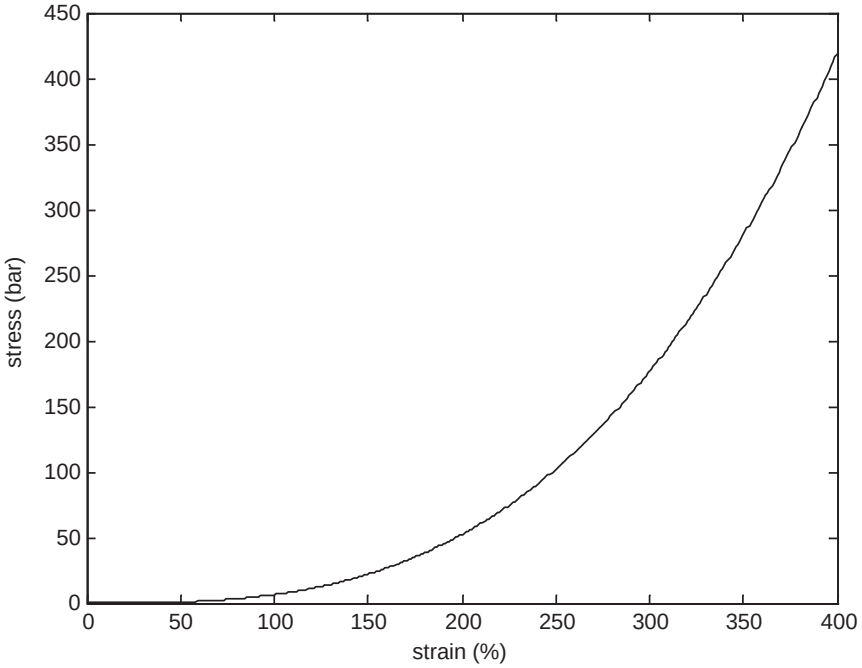

FIGURE 3.11: Stress-strain curve

Because the length before and after the draw is assumed to be the same, the thickness in each section after the draw can be obtained using

$$\tilde{h}_j = \frac{w_j h_j}{\tilde{w}_j} \tag{3.56}$$

where w_j are h_j are known, and ϵ_j (for $j = 1, \ldots, N$) allows the calculation of $\tilde{w}_j$ by employing Equation 3.47.

Finally, $\tilde{h}_j$ can be multiplied by the density to give the basis weight in each section after the draw, $\tilde{W}_j$. This deformation module is combined in series with the mass and heat transfer modules described in Sections 3.2 and 3.3 to form a sideway-draw model.

3.10 Summary

This chapter has reported the development of a first-principles model. The process, and hence the model, are large-scale and the model comprises several smaller models, such as the die model, forward-draw model, and sideways-draw model. Further, these smaller models are made of one or more modules, some of which are common to most unit operations (i.e., mass and heat transfer modules).

First-principles models of plastic film manufacturing processes are very rare as the first-principles modelling of a large-scale model such as the one concerned in this thesis is often regarded as difficult and time-consuming. Therefore, it is more common to employ an empirical model, but its suitability in control and fault monitoring can be limited because physical understanding of the process cannot be incorporated into the model.

The model introduced in this chapter is mostly based on the first-principles of chemical and mechanical engineering, taking account of the behaviour of polymer and the characteristics of most unit operations introduced in Chapter 2. When developing such a model, it is important to ensure that the model does not grow too complex, hence impractical.

This model can be utilised in many ways. For instance, most control and fault monitoring algorithms such as the ones introduced in Chapters 5 and 6 require either a state-space or transfer function model identified from the plant. Instead, the model can be used to simulate the plant enabling shorter and more flexible identification experiments, leading to less wasted product. Also, simulating the plant allows control and monitoring algorithms to be developed and tested safely and flexibly as discussed in Chapters 5 and 6. Furthermore, the model would be valuable for tuning the process and training the plant operators and allow for the determination of the optimal design, position, and spacing of sensors and actuators.

The implementation, validation, and simulation of the model are presented in the following chapter.

Chapter 4

Implementation and Validation of the Model

The implementation of the first-principles model reported in Chapter 3 and its performance are presented in Section 4.1. In order that the first-principles model can be utilised for developing and testing CD controllers, as in Chapter 5, the first-principles model is tuned until the die response of the first-principles model closely follows that of a die response model (DTF, 2007a), which is used to simulate the plant in real life, in Section 4.2.

Subsequently, the validation of the first-principles model is carried out also in Section 4.2 by comparing the estimates of final CD thickness profile with real-life measurements. However, the validation of the model at other locations throughout the model can be difficult or even impossible due to the limited number of sensors available online. This characteristic of the plastic film manufacturing process makes the validation of the model restricted to the operators' knowledge and limited data available. In compensation, a number of step tests have been performed at various locations, and the results have been validated against real-world process understanding. These results are also presented in Section 4.2, followed by the summary of this chapter in Section 4.3.

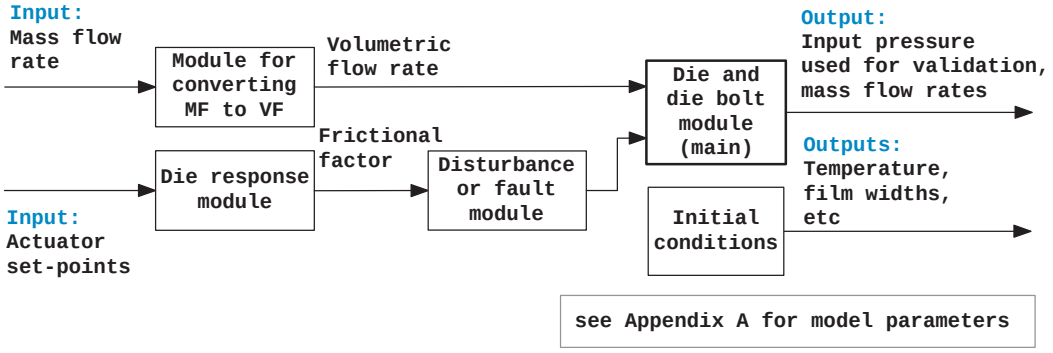

FIGURE 4.1: Die model

4.1 Implementation of the first-principles model

The first-principles model is implemented in Matlab/Simulink®. As depicted in Figure 4.5, the Simulink model comprises a number of smaller models, each of which is responsible for a unit operation introduced in the previous chapters. Each model contains one or more modules (or sub-models), such as deformation and heat transfer modules, depending on the unit operation – this was explained in Chapter 3. Inputs to and outputs from the model of each unit operation are summarised in Table 4.1, which also outlines modelled disturbances and faults and modelling assumptions associated with the model of each unit operation. The model parameters are not shown in the table but are listed in Appendix A. As presented in the table, tracked is process array (PA) which contains film width, temperature, and mass, from which thickness can be derived as shown in Section 3.2, of each CD section.

Modules which combine to form the die model shown in Figure 4.5 are depicted in Figure 4.1. Each module is designed to perform a different task. One performs conversion from mass flow to volumetric flow, and another models the disturbances summarised in Table 4.1. Moreover, the spatial and dynamic responses of the die explained in Section 4.2 are included in the module named "Die response module", and the module named "Die and die bolt module" is modelled using all the equations described in Section 3.4.

The first-principles model makes extensive use of s-functions (system functions) in Simulink. An s-function can be defined as a computer language description of

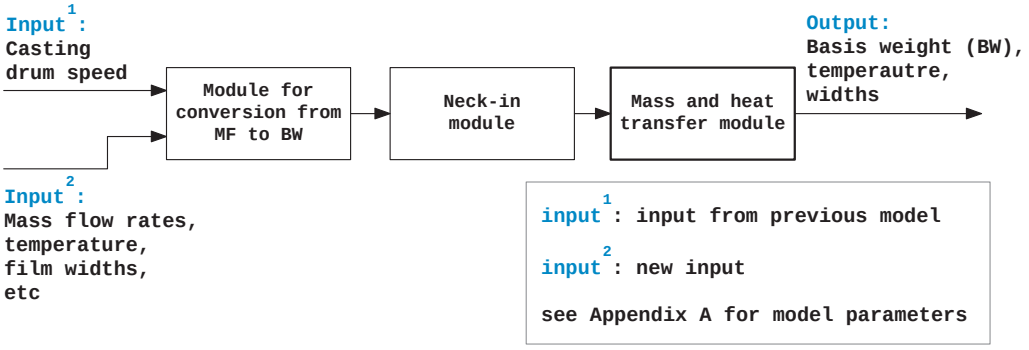

FIGURE 4.2: Casting model

a Simulink block and allows users to write their own codes to create their own Simulink blocks. All the equations are contained in s-functions, which can be found inside every module in Figure 4.1, for example. All the parameters including the geometrical data, which vary throughout the process (i.e., geometry of casting drums, rolls, or stenter oven), temperature of air and water, conductivity, heat transfer coefficients, and mass fraction crystalline, required for the calculation of specific heat capacity, (see Appendix A for more) are retrieved by the s-functions from the initialisation file which needs to be run before starting the Simulink model.

The casting model shown in Figure 4.5 (i.e., the block named "Casting to take-off rolls") contains three modules responsible for conversion from mass flow rate to basis weight, neck-in, and mass and heat transfer as depicted in Figure 4.2. The mass and heat transfer module contains an s-function, in which all the equations, introduced in Sections 3.2 and 3.3 are stored, while those described in Section 3.5 are contained in the modules named "Module for conversion from MF to BW" and "Neck-in module".

The model named "Stenter oven" in Figure 4.5 contains three smaller models for the stages prior to sideways-draw, for sideways-draw, and for the stages posterior to sideways-draw as depicted in Figure 4.3. The first and third models are modelled using the mass and heat transfer module, but the second model (i.e., sideways-draw) is modelled using the mass and heat transfer module as well as a deformation module as depicted in Figure 4.4. The deformation module includes an s-function that contains all the equations reported in Section 3.9.1.

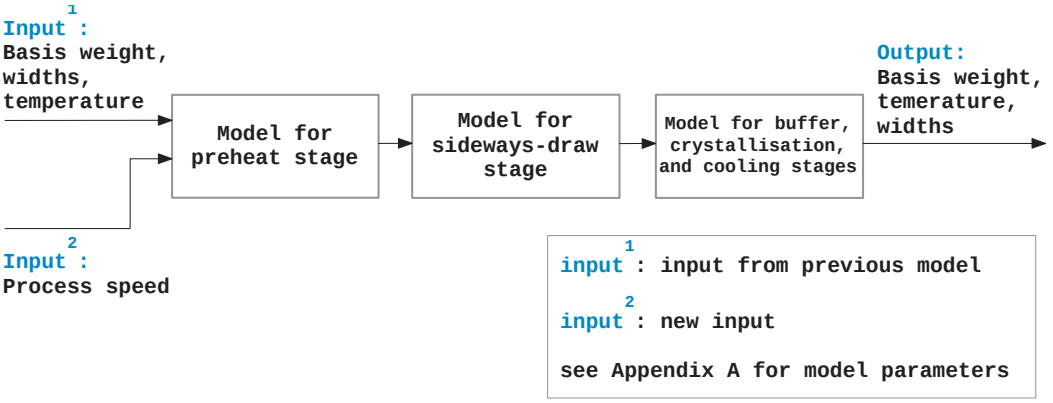

FIGURE 4.3: Stenter oven model

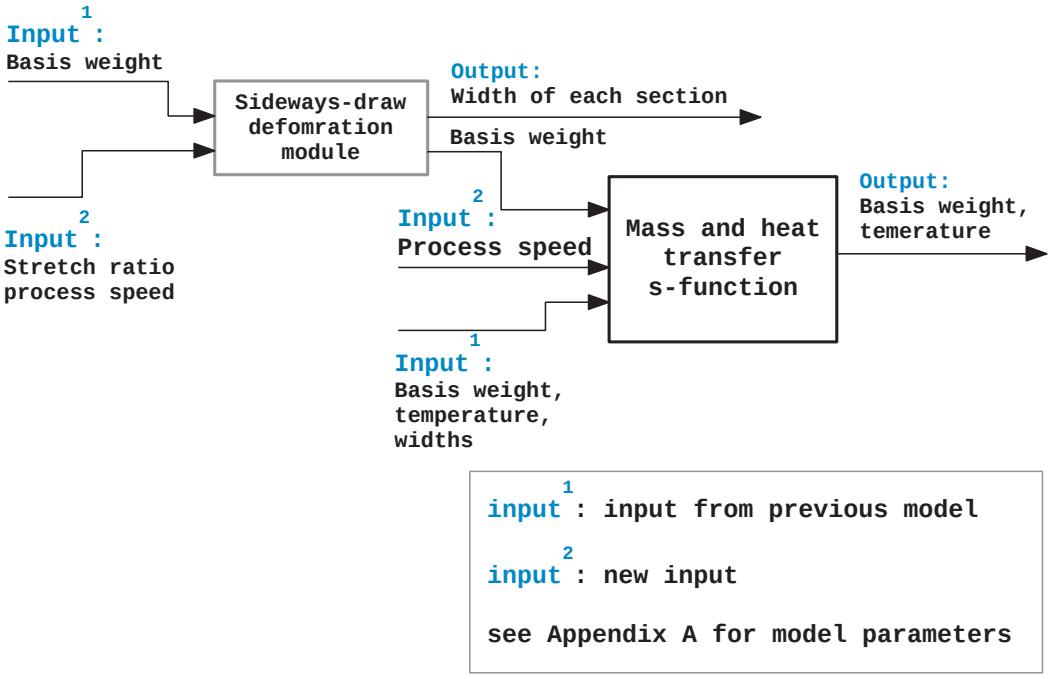

FIGURE 4.4: Sideways-draw model with 2 modules

The remaining models shown in Figure 4.5 are implemented in the same manner using the equations presented in Chapter 3, and a few samples of the Simulink models and Matlab files are included in Appendix D.

TABLE 4.1: Model Definition of Unit Processes

Unit Operation	Inputs	Outputs	Disturbances & Faults	Modelling Assumptions
Die	1. Mass flow rate 2. Temperature 3. Die bolt heater set-points	1. Mass flow rates 2. Temperature	1. Mass flow rate variation 2. Deposits on die-lip 3. Failed die bolt heater(s)	See Section 3.4
Casting drum & Quench rolls	1. Mass flow rates 2. Temperature 3. Casting drum speed	*PA* [1]	1. Temperature variation 2. Speed variation	Water spray effect neglected
Slow-nip & Preheat rolls	1. *PA* [1] 2. Slow-nip roll speed	*PA* [1]	1. Temperature variation 2. Speed variation	1. Even temperature across the rolls 2. Even speed across the rolls
Forward-draw	1. *PA* [1] 2. Fast-nip roll speed	*PA* [1]	1. Temperature variation	See Section 3.7
Cooling & Fast-nip rolls	*PA* [1]	*PA* [1]	1. Temperature variation 2. Speed variation	1. Even temperature across the rolls 2. Even speed across the rolls
Coaters	*PA* [1]	*PA* [1]	1. Variation in amount of coating material deployed	1. No change in film properties 2. Even speed across the rolls
Stenter oven	1. *PA* [1] 2. Stenter speed	*PA* [1]	1. Temperature variation 2. Speed variation 3. Stretch ratio variation	Bowing effect neglected

[1] *Process Array (PA) includes mass, film Width, and temperature of each CD section*

See Appendix A for model parameters

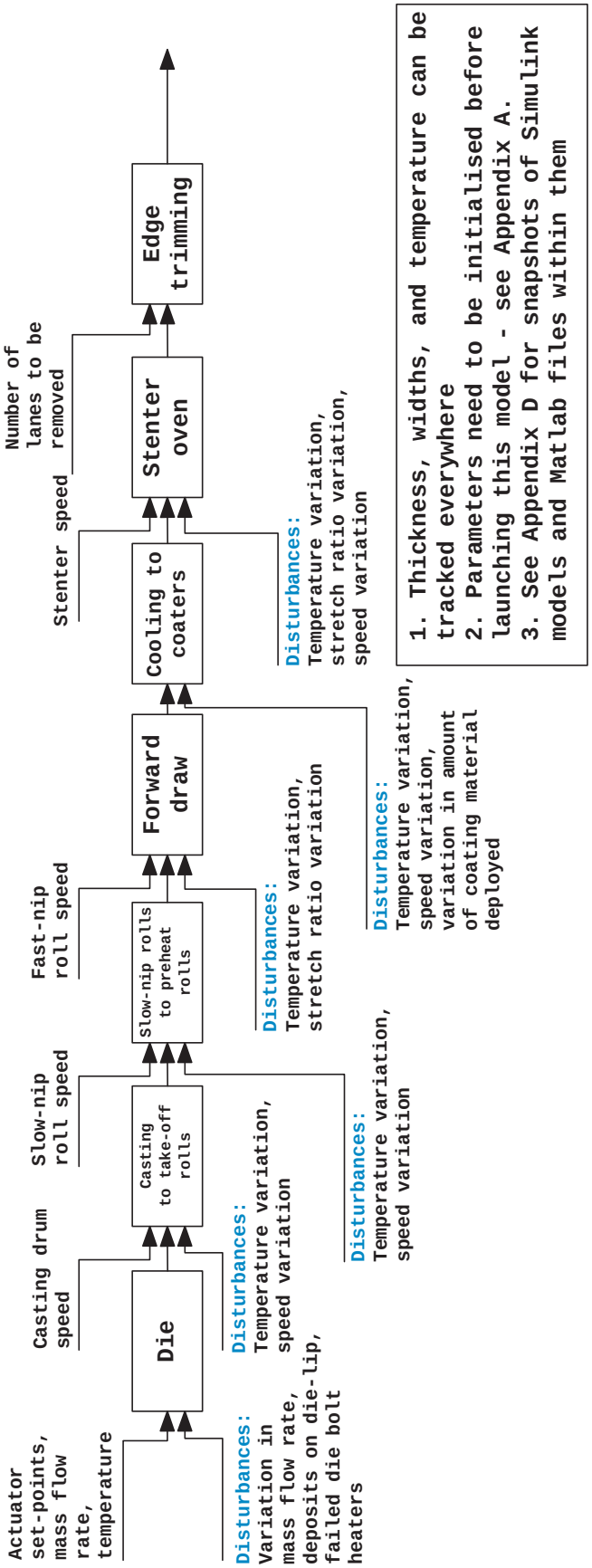

FIGURE 4.5: First-principles model

4.1.1 Model Performance

For all simulations presented in this thesis, it is assumed that there are 10 die bolt heaters and the model divides the film into 10 lanes (CD sections), but the model is capable of handling any number subject to speed constraints. Recall that in real life, there are 49 die bolt heaters and the film is divided into 245 lanes for controlling purposes. "10" is chosen because it strikes a good balance between simulation time and complexity. The completion time for the model when 10 lanes are used is 380 seconds in real-time to simulate 500 seconds in simulation-time on a AMD™Phenom X4 955 GHz machine.

4.2 Parameter Tuning and Model Validation

A die response model, which is utilised in real life to simulate the plant, has been provided (DTF, 2007a). This model generates CD thickness profiles given actuator (die bolt heater) set-points. In Section 4.2.1, these CD thickness profiles are compared with those generated by the first-principles model when the same actuator set-points are employed. The first-principles model is tuned until its thickness profiles follow the die response model's closely.

Once the model has been tuned to give a similar die response to the die response model, as a validation experiment, the model employs real-life operational and geometrical data, and then the model estimates of thickness profiles are compared with the real-life thickness profiles as reported in Section 4.2.2. As discussed in Chapter 3, the real-life process employs only one gauging sensor towards the end of the process prior to the winder. This implies that further validation of the first-principles model is not straightforward.

In compensation, step response tests have been carried out at various locations of the first-principles model. The results, which have been validated against the process, are tabulated and discussed in Section 4.2.3.

4.2.1 Die Response

The die response model considered in this study can be defined as

$$\mathbf{y}(t) = q^{-d} g(q^{-1}) k_p \mathbf{G}\mathbf{u}(t) \tag{4.1}$$

where $\mathbf{u}(t) \in \mathbb{R}^N$ and $\mathbf{y}(t) \in \mathbb{R}^M$ respectively represent the actuator set-points and thickness profile. The set-points have a range between 0 and 100%, k_p represents the process gain, d is the process delay, $g(q^{-d})$ denotes the discrete form of a first order model, and $\mathbf{G}$ is the interaction matrix representing the spatial response, which gives each actuator the response of a Gaussian curve as follows:

$$G(m,n) = exp(\frac{-(m-5n)^2}{2\sigma^2}) \tag{4.2}$$

where m and n denote the row-column index. $y_j(t)$ is represented as a percentage deviation from full scan mean thickness such that

$$y_j(t) = \frac{h_j(t) - \bar{h}(t)}{\bar{h}(t)} \times 100 \tag{4.3}$$

where $h_j(t)$ denotes the thickness in section j, and $\bar{h}(t)$ represents the mean thickness in the width direction (CD).

$5n$ determines the centre position of the response of n^{th} actuator in the measurement vector, $\mathbf{y}(t)$. For instance, the response of 30^{th} actuator (i.e., $u_j(t) = 1$ for $j = 30$ and $u_j(t) = 0$ for $j \neq 30$) is depicted in Figure 4.6 (solid line) when the interaction matrix, $\mathbf{G}$ is employed. The number 5 is due to the fact that each actuator covers 5 measurements – the number of actuators (N) and that of measurements (M) are respectively 49 and 245 (Section 4.1.1) – and $\sigma^2 = 5.5$ is assumed to be the same for all n. The equation for the interaction matrix implies that n^{th} actuator affects the thickness not only in sections $(5n-2)$, $(5n-1)$, $(5n)$, $(5n+1)$, and $(5n+2)$ but also in the neighbouring sections due to the interactions.

Before tuning the first-principles model using the die response model such that the response of the first-principles model's die model follows that of the die response model, small modification needs to be made to the interaction matrix, $\mathbf{G}$ as follows.

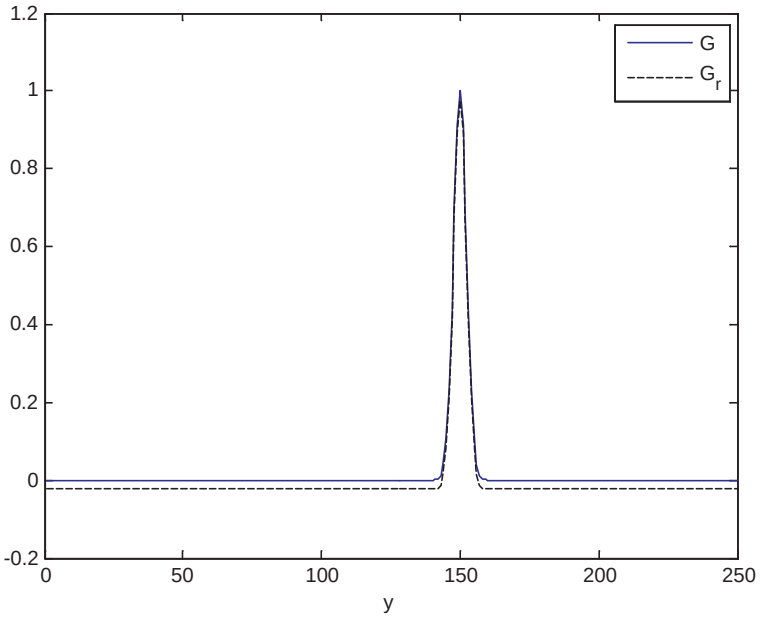

FIGURE 4.6: CD profiles for both G and G_r when $u_j(t) = 1$ for $j = 30$ and $u_j(t) = 0$ for $j \neq 30$

Since mean thickness changes require either changes to the input mass flow rate into the die or process speed, the die response should not change the mean thickness of the film, that is, the mean in percentage deviation from full scan mean thickness always needs to be zero. However, the interaction matrix, $\mathbf{G}$ does not ensure mean zero. Therefore, the interaction matrix, $\mathbf{G}$ is modified by subtracting the mean of each column (μ_n) from every element of $\mathbf{G}$, where the mean of each column can be defined as follows:

$$\mu_n = \frac{1}{M} \sum_{m=1}^{M} G(m, n) \tag{4.4}$$

for $n = 1, \ldots, N$.

For example, the response of 30^{th} actuator (i.e., $u_j(t) = 1$ for $j = 30$ and $u_j(t) = 0$ for $j \neq 30$) is depicted in Figure 4.6 (dashed line) when the modified interaction matrix, $\mathbf{G}_r$ is employed. The interaction matrix, $\mathbf{G}_r$ now ensures that the mean thickness of the film remains intact unless the mass flow rate or process speed is

altered. Note that the mean of the dashed line is zero while that of the solid line is not.

Having introduced a new interaction matrix, the first-principles model can be tuned to follow the die response model. The module named "Die response module" in Figure 4.1 comprises the spatial and dynamic components of the die model. The spatial component is modelled using Equation 3.34 except that the interaction matrix in the equation is replaced by the new interaction matrix, $\mathbf{G}_r$ whose numbers of columns and rows are 10 because both the number of actuators (N) and size of the measurement vector (M) are assumed to be 10. The dynamic component is modelled using the first-order model in Equation 4.1. Now, the response of the first-principles model is able to follow that of the die response model by tuning k_g in Equation 3.34.

k_p in Equation 4.2 is typically set to 0.15 in implementations on the process. This implies that 10% increase in j^{th} actuator setting, $u_j(t)$ should result in 1.5% *increase* in j^{th} measurement, $y_j(t)$. However, since the die model of the first-principles model employs viscosity factor, introduced in Section 3.4, 10% increase in j^{th} actuator setting, $u_j(t)$ should result in 1.5% *decrease* in j^{th} measurement, $y_j(t)$, instead. This is carried out by trial and error. Figure 4.7 depicts the measurements when 10% increase has been applied to 3^{rd} actuator setting only. The result implies that k_g has been configured properly as 10% increase in 3^{rd} actuator setting decreases 3^{rd} measurement by 1.5%. The similar results can be obtained with the rest of the actuator settings since they all produce similar dynamic and spatial responses. Furthermore, to mimic what happens in real life, the edges (1^{st} and 10^{th} lanes) are removed, and all the figures in this thesis depict 8 lanes only.

Moreover, the die model needs to produce a uniform mass flow profile across the die-lip gap when the actuator set-points are uniform. Equation 3.34 therefore needs to be modified as follows:

$$\mathbf{f} = k_g \mathbf{G}_r \mathbf{u}(t) + \boldsymbol{\xi} \tag{4.5}$$

where $\boldsymbol{\xi} \in \mathbb{R}^N$ is the mass flow correction factor which ensures uniform mass flow rates of polymer at the die-lip gap. Figure 4.8 depicts the mass flow rates once

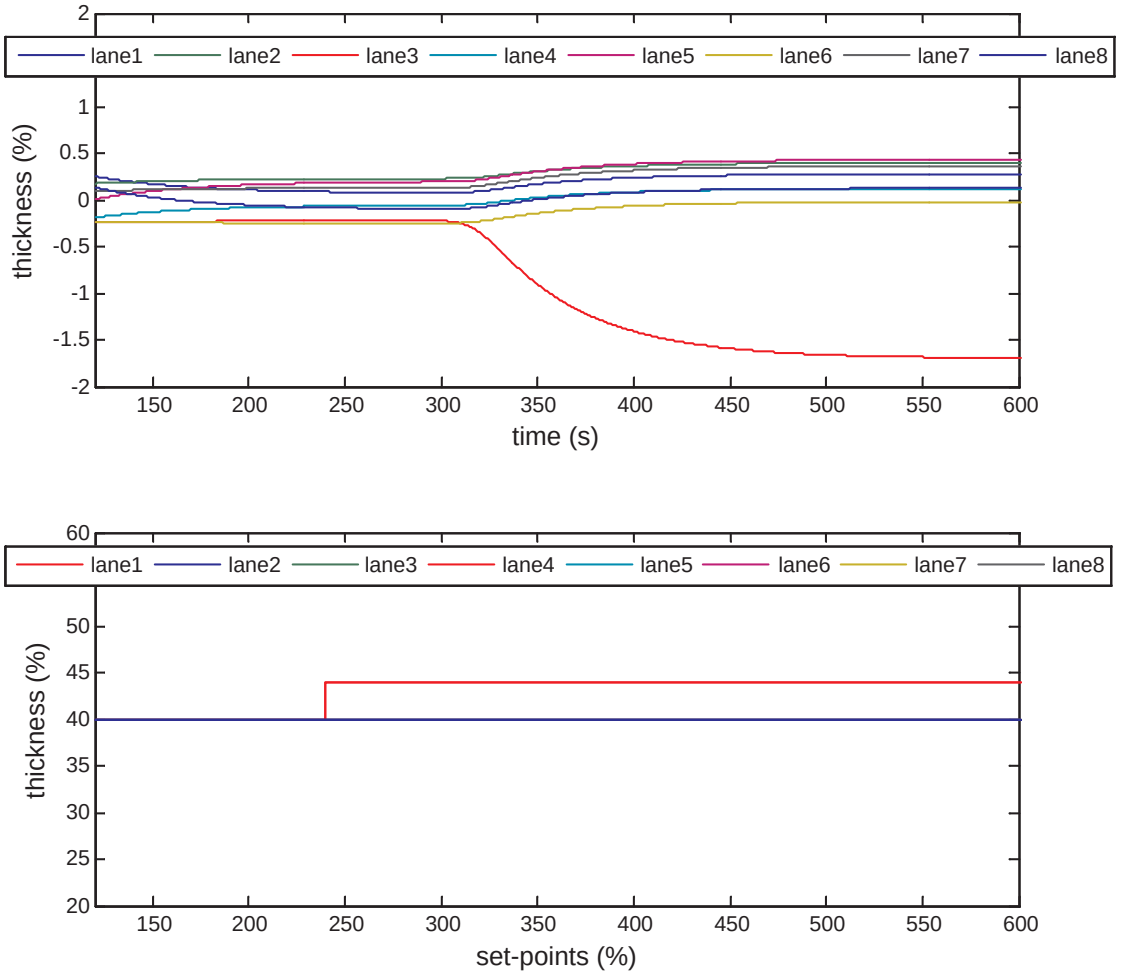

FIGURE 4.7: Upper plot: set-points, Lower plot: measurements; 10% step increase applied to 3^{rd} lane

Equation 4.5 has been configured properly. It shows that the deviation in mass flow rate remains within 0.5% when the actuator set-points are uniform.

In addition to the mass flow rates at the die outlet, the die model produces pressure at the inlet, which can be employed in a validation experiment as follows. At a certain mass flow rate, $x_m kg/s$ (which cannot be shown due to confidentiality reasons), pressure at the die inlet has been measured in the range from 10 to 20 bar on the real-life process. Although further validation is required, the die model produces 13.8 bar, which is at least within the range.

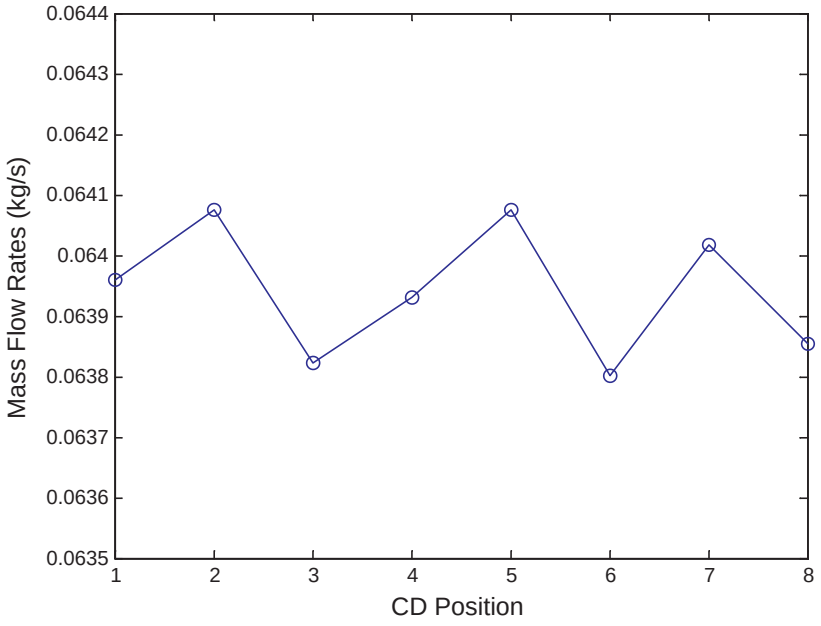

FIGURE 4.8: Mass flow rates at die-lip

After all, the first-principles model has been tuned to produce a response that is close to the response of the model described by Equation 4.1, which is used to simulate the plant in real life. After further validation of the model in the following subsections, the model should be capable of simulating the plant for developing and testing control and fault monitoring algorithms as reported in Chapters 5 and 6.

4.2.2 Product Thickness

All the parameters and input variables required for the first-principles model are summarised in Appendix A and Table 4.1, respectively. Two different sets of these parameters and input variables employed in real life and the resulting mean thicknesses have been provided – these sets are referred to as standard conditions (SC) 1 and 2 (DTF, 2007c,d), and see Section 3.1 for the definition of parameter and input variable. The same sets have been employed by the model and the resulting mean thicknesses, which the model estimates, are compared to the ones given in SC1 and SC2 as shown in Table 4.2. The table only shows the parameters

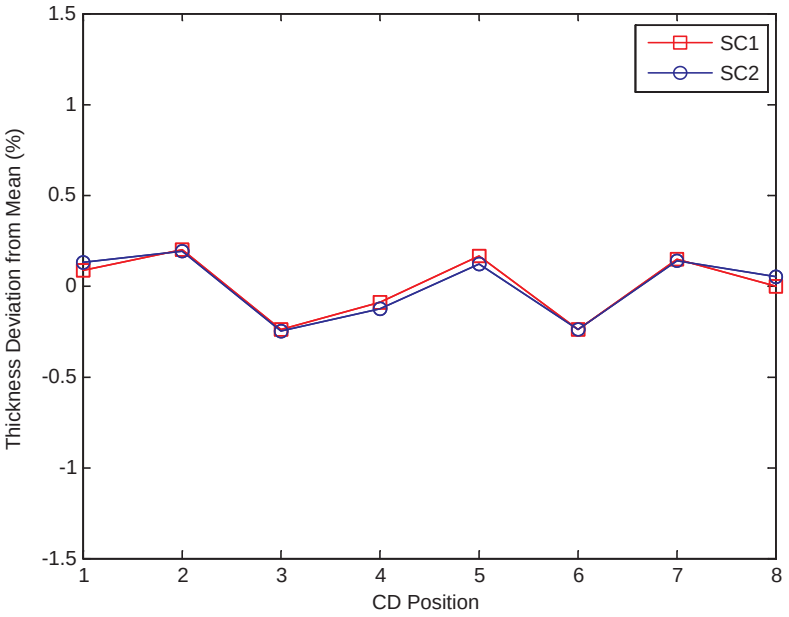

FIGURE 4.9: CD thickness profiles of final product when data from SC1 and SC2 are used

and input variables which are frequently altered, but all other parameters of the model listed in Appendix A are also the same as those used in real life for each simulation.

The results present that the difference between the real-life measurements and the model estimates of the mean thickness remained within 8% when the parameters from the SC1 are used and 2% when the parameters from the SC2 are used.

Moreover, the corresponding CD thickness profiles generated by the first-principles model are depicted in Figure 4.9. Although the mean thicknesses are different as shown in Table 4.3, the thickness profiles depicted in the figure are almost identical because they are in percentage deviation (%) from full scan mean thickness rather than in basis weight (kg/m^2) or thickness (m). The figure indicates that the thickness deviation remained within 0.5%, but this can still be improved by the use of a CD controller. When disturbances are present, the thickness profiles can be worsened significantly, and this leads to the design of a CD controller as presented in Chapter 5.

TABLE 4.2: Validation using Standard Conditions

	Mass flow (kgs^{-1})	**Casting speed** (ms^{-1})	**Slow-nip rolls speed** (ms^{-1})	**Fast-nip rolls speed** (ms^{-1})	**Stenter oven speed** (ms^{-1})	**Sideways-draw ratio**	**Initial width** (m)	**Final width** (m)	**Mean thickness** (μm)
SC1[1]	x_m	v_1	v_1	$\tilde{v}_1$	$\tilde{v}_1$	Λ_1	w_1	$\tilde{w}_1$	79
SIM1[2]	x_m	v_1	v_1	$\tilde{v}_1$	$\tilde{v}_1$	Λ_1	w_1	$\tilde{w}_1$	85
SC2[1]	x_m	v_2	v_2	$\tilde{v}_2$	$\tilde{v}_2$	Λ_2	w_2	$\tilde{w}_2$	250
SIM2[2]	x_m	v_2	v_2	$\tilde{v}_2$	$\tilde{v}_2$	Λ_2	w_2	$\tilde{w}_2$	255

[1] *SC: Standard conditions used in real life*

[2] *SIM: Model simulation*

Input and parameter values are not shown due to confidentiality reasons

4.2.3 Step Responses at Various Locations

As reported in Chapter 2, the thickness profile is measured only by the scanning gauge. Moreover, although the temperature of many locations, such as different regions inside the stenter oven, is controlled, the exact temperature of the plastic film rather than the surrounding air or water inside the rolls is usually not measured. However, the temperature tracked throughout the model is the film temperature. These characteristics of the process limit the validation of the model.

In compensation, a number of open-loop step tests have been carried out at various locations. The results are presented in Table 4.3 and have been validated against real-world process understanding. The test scenarios, abbreviations and symbols used, and the descriptions of the results are presented as follows.

Abbreviations and Symbols used in Table 4.3

- $-$: decrease in mean thickness or temperature
- $+$: increase in mean thickness or temperature
- **Cast**: casting drum
- **Cool**: cooling rolls
- **FD**: forward-draw
- **FR**: fast-nip rolls
- **MF**: mass flow rate
- **N**: no change in mean thickness or temperature
- **N**$-$: no change in mean thickness or temperature as $t \to \infty$ with $-$ve overshoot
- **N**$+$: no change in mean thickness or temperature as $t \to \infty$ with $+$ve overshoot
- **PH**: pre-heat rolls

- **SD**: sideways-draw
- **SR**: slow-nip rolls
- **ST1**: stenter oven – prior to SD
- **ST2**: stenter oven – posterior to SD
- **ST3**: stenter oven – exit
- **T**: temperature (in °C)
- **W**: basis weight (in kg/m^2)

Step Test Scenarios

1. Step increase in MF only by 10% at 1500s
2. Step increase in CD/SR speed only by 10% at 1500s – CD speed is assumed to be the same as SR speed
3. Step increase in FR/ST speed only by 10% at 1500s – FR speed is assumed to be the same as ST speed
4. Step increase in SD ratio only by 10% at 1500s
5. Step increase in die temperature only by 10% at 1500s
6. Step increase in PH temperature only by 10% at 1500s
7. Step increase in Cool temperature only by 10% at 1500s

Descriptions of Results

- *Step 1*: The step increase in MF into the die results in thickness increases at every location as shown. The temperature increase is also experienced everywhere because the thicker film is cooled more slowly by the casting drum, and the film thus starts with higher temperature. Adversely, the subsequent pre-heat rolls heat the thicker film more slowly, but apparently the effect of the casting drum seems more prominent; therefore, temperature increase rather than temperature decrease is experienced at every location.

- *Step 2*: The step increase in CD/SR speed decreases the film thickness before forward-draw but does not affect the thickness after forward-draw because the thickness is dependent on the current speed. Moreover, the thinner film is cooled more quickly by the casting drum but also heated more quickly by the pre-heat rolls. For the same reason as *Step 1*, the temperature decreased by the casting drum affects the film more than the temperature increased by the pre-heat rolls. The step increase thus decreases the film temperature as it passes over the casting drum, and this effect continues throughout the process. However, it has no impact on the final product (i.e., "T ST3") because the temperature increased by the crystallisation stage and the temperature decreased by the subsequent cooling stage seem relatively higher than the temperature reduction caused by the step test.

- *Step 3*: The step increase in FR/ST speed affects the thickness after forward-draw but has no impact on the thickness before forward-draw for the same reason as *Step 2*. The thinner film is cooled more quickly by the cooling rolls but, at the same time, heated more quickly by the pre-heat oven inside the stenter oven. Apparently, the film seems to be affected more by the former and thus has lower temperature at "Cool", "ST1", and "ST2". For the same reason as *Step 2*, the film temperature remains intact at "ST3".

- *Step 4*: The step increase in SD ratio allows the film to become thinner once the film has been stretched by sideways-draw. The temperature of thinner film is heated more quickly by the crystallisation stage but, at the same time, cooled even more by the cooling stage towards the end of the process. The effect of the final cooling stage seems to be slightly higher than that of the crystallisation stage, thereby indicating a slight decrease at "ST3", although this did not show in *Step 2* and *Step 3*.

- *Step 5*: The step increase in the temperature of the polymer entering the die has no effect on the film thickness throughout the process but increases the film temperature at every location.

- *Step 6*: The step increase in the temperature of the film passing over the pre-heat rolls has no effect on the film thickness throughout the process but increases the film temperature at every location after the step increase.

- *Step 7*: The step increase in the temperature of the film passing over the cooling rolls has no effect on the film thickness throughout the process but increases the film temperature at every location after the step increase.

TABLE 4.3: Step Tests at Various Locations

	W Cast	**W PH**	**W FD**	**W Cool**	**W ST1**	**W ST2**	**W ST3**	**T Cast**	**T PH**	**T FD**	**T Cool**	**T ST1**	**T ST2**	**T ST3**
Step 1: MF into Die	+	+	+	+	+	+	+	+	+	+	+	+	+	+
Step 2: CD/SR Speed	−	−	N+	N+	N+	N+	N+	−	−	−	−	−	−	N+
Step 3: FR/ST Speed	N	N	−	−	−	−	−	N	N	−	−	−	−	N
Step 4: SD Ratio	N	N	N	N	N	−	−	N	N	N	N	N	+	−
Step 5: T @ die	N	N	N	N	N	N	N	+	+	+	+	+	+	+
Step 6: T @ PH	N	N	N	N	N	N	N	N	+	+	+	+	+	+
Step 7: T @ Cool	N	N	N	N	N	N	N	N	N	N	+	+	+	+

Refer to Section 4.2.3 for the step test scenarios, abbreviations and symbols, and explanation

4.3 Summary

This chapter begins with the implementation of the first-principles model presented in the previous chapter in Matlab/Simulink. A die response model used in real life has been provided, and the first-principles model is tuned until its response matches that of the die response model. This is important as the die response is responsible for the CD control of the process as discussed in the previous chapters.

The model is then validated using real-life measurements of CD thickness profile of final product. Due to the limited number of sensors available online in real life, obtaining the measurements at other locations has not been possible. In compensation, a number of open-loop step response tests at various locations are carried out, and the results are validated against the process. In closed-loop, the controller design is a regulator problem as discussed in Chapter 5. The controller studied in this thesis is a CD controller, which only ensures that the film is flat in the CD by manipulating the actuator set-points but does not have any impact on the mean thickness. Because the step tests are concerned with the mean thickness and temperature, the closed-loop step response tests produce the same results as the open-loop step response tests. Therefore, only the open-loop test results are included in this chapter.

The model can be utilised in many ways as discussed in Section 3.10, but the subsequent chapters employ the model to simulate the plant to allow control and fault monitoring algorithms to be developed and tested safely and flexibly.

Chapter 5

Cross-directional Control

Plastic film manufacture, like other sheet-forming processes such as papermaking (Kristinsson and Dumont., 1996; Mijanovic et al., 2002) and metal-rolling (Goodwin et al., 1990; Grimble, 2001; Ringwood, 1995), employs arrays of actuators across a continuously moving sheet to control the cross-directional (CD) thickness profile of the finished product as measured by a scanning gauge downstream from the actuators towards the end of the process as discussed in Section 1.2. CD control has received a considerable attention in the control systems community, and there have been many papers published studying various CD controller designs (Featherstone and Braatz, 1998; Gorinevsky et al., 2000; Heath, 1996; Stewart et al., 2003b; Wills and Heath, 2002).

This chapter reports the development and implementation of a model-based CD controller. The proposed controller design has a similar structure to that of the controller summarised in Section 5.1.2 since both are modifications to internal model control (IMC) (Arkun and Kayihan, 1998; VanAntwerp and Braatz, 1999), which can be regarded as a dynamic compensator. The controller presented here requires the solution of a new quadratic programming problem online to achieve optimal steady state performance which is subject to actuator and bending constraints. Model-based CD controllers require an accurate reference model and controller performance can be improved by minimising the effect of model-plant mismatch and that of disturbances. Consequently, the proposed controller design employs an observer (Kokotovic et al., 1999; Ogata, 2002; O'Reilly, 1983) in place of the reference model in order to reduce the effect of model-plant mismatch as

well as that of disturbances. Moreover, the optimal steady state performance is encouraged and the actuator saturation is discouraged by introducing a new objective function which needs to be optimised online.

Section 5.1 summarises existing industrial and model-based controllers. Section 5.2 presents the new CD controller, and not only is this applied to the first-principles model – which is developed in Chapters 3 and 4 and is used to simulate the plant throughout this thesis – but the controllers summarised in Section 5.1 are also applied in order to demonstrate the performance of the new controller relative to the existing controllers in Section 5.3. Section 5.4 summarises this chapter.

5.1 Existing Controllers

The two existing controllers summarised here make a standard assumption that the open-loop behaviour of the output profile can be well approximated by the model

$$\mathbf{y}(t) = z^{-d} g(z^{-1}) k_p \mathbf{G}\mathbf{u}(t) \tag{5.1}$$

which has already been introduced in the previous chapter, and the first-order transfer function, $g(z^{-1})$ can be expressed as

$$g(z^{-1}) = \frac{1-\alpha}{1-\alpha z^{-1}} \tag{5.2}$$

5.1.1 Industrial Controller

The industrial controller presented here is used for a plastic film manufacturing process in real life and can be found in Taylor and Duncan (2006). It has a very similar structure to the controllers studied in Duncan and Bryant (1997) and Stewart et al. (2003a). The CD thickness profile at uniform CD intervals measured by the scanning gauge is mapped to the actuator array for the set-points calculation. The actuator set-points, $\mathbf{u}(t) \in \mathbb{R}^N$ are calculated based on

the measured profile, $\mathbf{y}(t) \in \mathbb{R}^M$ using

$$\mathbf{u}(t) = \mathbf{K}(q^{-1})\mathbf{y}(t) \tag{5.3}$$

The controller, $\mathbf{K}(q^{-1})$ can be written in terms of numerator and denominator polynomials as follow:

$$\mathbf{u}(t) = (\mathbf{L}_A(q^{-1}))^{-1}\mathbf{L}_B(q^{-1})\mathbf{y}(t) \tag{5.4}$$

where

$$\begin{aligned}\mathbf{L}_A(q^{-1}) = \mathbf{I}_N - \mathbf{\Gamma}q^{-1} + \beta k(1-q^{-d})g(q^{-1}) \\ + (1-\beta)\mathbf{\Gamma}k(1-q^{-d})g(q^{-1})\end{aligned} \tag{5.5}$$

$$\mathbf{L}_B(q^{-1}) = \beta\mathbf{K} + (1-\beta)\mathbf{\Gamma}\mathbf{K}q^{-1} \tag{5.6}$$

and

$$\mathbf{K} = kk_p^{-1}(\mathbf{G}_r^T\mathbf{G}_r + \mu\mathbf{I}_N)^{-1}\mathbf{G}_r^T \tag{5.7}$$

The tri-diagonal matrix, $\mathbf{\Gamma}$ containing main diagonal elements of $1-\gamma$ and off-diagonal elements of $\gamma/2$ performs set-point smoothing (Stewart et al., 2003a) in order to discourage actuator saturation, thereby improving the robustness of the controller. The interaction matrix, $\mathbf{G}_r$ and the term, k_p are given in Equation 4.5 in the previous chapter and Equation 5.1. k is the main tuning factor of the controller, and the last two terms on the right hand side of $\mathbf{L}_A(q^{-1})$ denote the dead time compensator based on the assumed first order dynamics, $g(q^{-1})$ and the process delay, d, both of which are also given in Equation 5.1. The term, μ further improves the robustness by reducing the magnitude of the set-point changes, thereby reducing the chance of the actuator set-points becoming unbounded (Duncan and Bryant, 1997).

5.1.2 Model-based Controller

The model-based controller studied in Heath and Wills (2002, 2003, 2004) is depicted in Figure 5.1. It is a modification to internal model control (IMC). $\mathbf{Q}(z^{-1})$ in Figure 5.1 is a dead time compensator based on $g(q^{-1})$ and the process

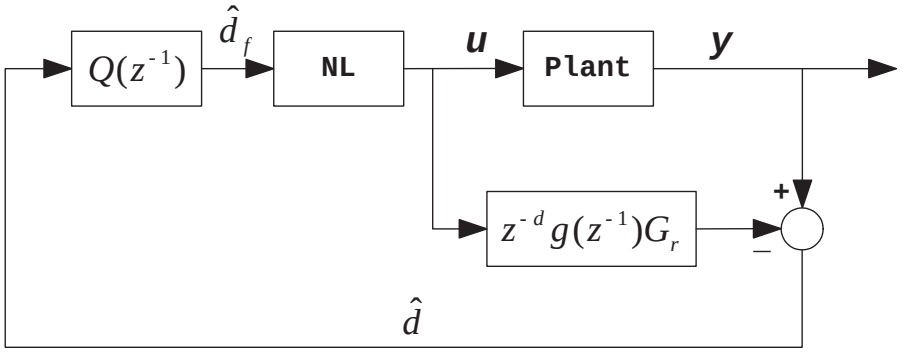

FIGURE 5.1: IMC configuration with non-linear element for steady state performance and anti-windup

delay, d, both of which are given in Equation 5.1. This dead time compensator (or dynamic compensator) is utilised by the proposed controller design and is thus explained in the following section.

Assuming that a steady state estimate of $\hat{\mathbf{d}}(t) \in \mathbb{R}^M$ exists, the optimal actuator setting of the controller shown in Figure 5.1 can be obtained with

$$\mathbf{u}_{ss}(t) = \arg\min_{\mathbf{u}(t)} \left\| \mathbf{G}_r \mathbf{u}(t) + \hat{\mathbf{d}}(t) \right\|_2 \tag{5.8}$$

where $\|.\|_2$ denotes L_2 norm. $\mathbf{u}(t) \in \mathbb{R}^N$ is subject to constraints, such as actuator saturation and bending constraints. However, bending constraints are usually related to other sheet-forming processes such as metal rolling rather than plastic film manufacturing processes. The non-linear element (NL) in Figure 5.1 continuously produces the optimal control action using Equation 5.8 and also discourages actuator saturation by ensuring that the set-points, $\mathbf{u}(t)$ are within the physical limit.

The structure of the controller presented here is the most basic version of the kind, and a few other versions (Heath and Wills, 2002, 2003, 2004) are available but not presented in this thesis.

5.2 Proposed Controller

While the industrial controller summarised in the previous section is often used in industry, the model-based controller has not been used as frequently for two reasons. Firstly, for high-speed plastic film manufacturing processes, it has not been feasible to solve the optimisation problem such as Equation 5.8 online within the sampling interval (VanAntwerp et al., 2007). Secondly, the reference model, for instance $z^{-d}g(z^{-1})\mathbf{G}_r$ in Figure 5.1, requires to be very accurate, but it is not easy to obtain such a model.

The first problem is now less restrictive since the computer processor speed has improved dramatically over the last decade. For the second problem, the proposed controller design illustrated in Figure 5.2 attempts to improve the accuracy of the reference model by constructing an observer whose gain is designed to minimise model-plant mismatch.

Another advantage of the proposed controller design is that for the reference model, which is used for the controller design, there is no need to separate the dynamic component from the spatial component unlike the controller designs summarised in Section 5.1. The derivation of a model in such a form requires a system identification process such as the ones described in Featherstone et al. (2000) and Gorinevsky and Gheorghe (2003). Instead, the proposed controller design utilises the System Identification Toolbox™7 in Matlab®, which is more widely available, to derive a state space model directly from the first-principles model (Chapter 3) or the plant. Derivation of this state space model using subspace method included in the System Identification Toolbox™7 is presented in Appendix B.

This state space model is used to construct an observer which is then employed as the reference model for the proposed controller design. The observer can be designed to reduce not only the effect of the model-plant mismatch, but also the effect of disturbances. Moreover, for the optimal steady state actuator setting of the controller, a new objective function is introduced and optimised online.

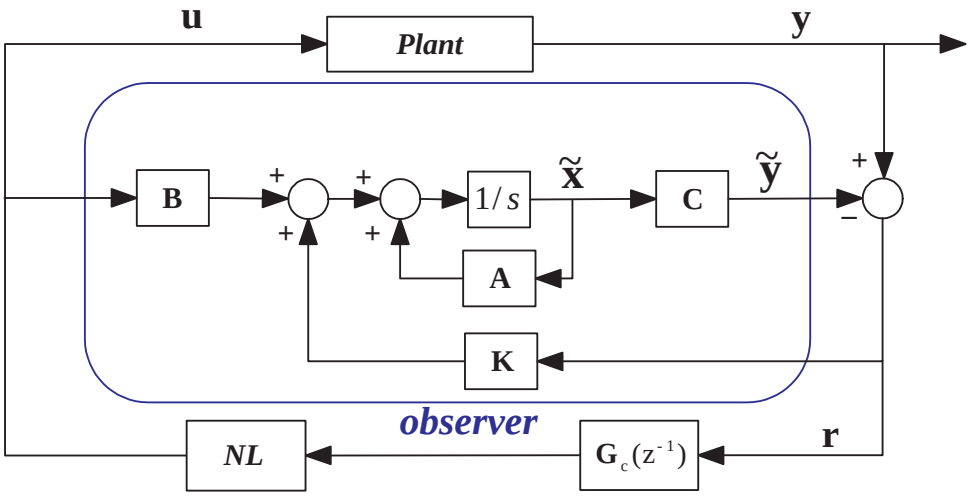

FIGURE 5.2: Proposed controller

5.2.1 Obsever Design

The mathematical description of the observer is as follows:

$$\begin{aligned}\dot{\tilde{\mathbf{x}}}(t) &= \mathbf{A}\tilde{\mathbf{x}}(t) + \mathbf{B}\mathbf{u}(t) + \mathbf{K}(\mathbf{y}(t) - \tilde{\mathbf{y}}(t)) \\ \tilde{\mathbf{y}}(t) &= \mathbf{C}\tilde{\mathbf{x}}(t)\end{aligned} \tag{5.9}$$

where $\mathbf{y}(t) \in \mathbb{R}^N$ and $\tilde{\mathbf{y}}(t) \in \mathbb{R}^N$ denote the plant (the first-principles model simulates the plant in this thesis) measurements and model estimates, respectively. $\mathbf{u}(t) \in \mathbb{R}^M$ represents the control action, and $\mathbf{A}$, $\mathbf{B}$, and $\mathbf{C}$ are the state space matrices given in Appendix B. The term with the observer gain, $\mathbf{K}$ continuously corrects the observer estimate, $\tilde{\mathbf{y}}(t)$ such that it follows $\mathbf{y}(t)$ more closely. This implies that the effects of model-plant mismatch and disturbances can be reduced by the optimisation of $\mathbf{K}$.

Derivation of an optimal gain, $\mathbf{K}$ is summarised in this section. $\mathbf{G}_c(z^{-1})$ and the non-linear element (NL) depicted in Figure 5.2 are responsible for dynamic compensation and steady state performance, respectively, and are presented in Sections 5.2.2 and 5.2.3.

5.2.1.1 Observer Gain in Frequency Domain

Assuming that the plant can be represented in the state space form, model-plant mismatch and disturbances may be described by additional terms, $\mathbf{d}_1(t) \in \mathbb{R}^R$ and $\mathbf{d}_2(t) \in \mathbb{R}^N$ as

$$\begin{aligned} \dot{\mathbf{x}}(t) &= \mathbf{A}\mathbf{x}(t) + \mathbf{B}\mathbf{u}(t) + \mathbf{d}_1(t) \\ \mathbf{y}(t) &= \mathbf{C}\mathbf{x}(t) + \mathbf{d}_2(t) \end{aligned} \tag{5.10}$$

The vectors, $\mathbf{d}_1(t)$ and $\mathbf{d}_2(t)$ can represent any unknown input such as model-plant mismatch and disturbances as follows:

$$\begin{aligned} \mathbf{d}_1(t) &= \Delta\mathbf{A}\mathbf{x}(t) + \Delta\mathbf{B}\mathbf{u}(t) + \mathbf{E}_1\tilde{\mathbf{d}}_1(t) \\ \mathbf{d}_2(t) &= \Delta\mathbf{C}\mathbf{x}(t) + \mathbf{E}_2\tilde{\mathbf{d}}_2(t) \end{aligned} \tag{5.11}$$

where $\mathbf{E}_1$ and $\mathbf{E}_2$ are the disturbance distribution matrices, and $\tilde{\mathbf{d}}_1(t)$ and $\tilde{\mathbf{d}}_2(t)$ are the disturbance signals. $\Delta\mathbf{A}$, $\Delta\mathbf{B}$, and $\Delta\mathbf{C}$ are the parameter errors or variation that represents model-plant mismatch.

Subtracting $\dot{\hat{\mathbf{x}}}(t)$ in Equation 5.9 from $\dot{\mathbf{x}}(t)$ in Equation 5.10, the equation for the residual, $\mathbf{r}(t)$ can be derived as follows:

$$\begin{aligned} \dot{\mathbf{e}}(t) &= (\mathbf{A} - \mathbf{K}\mathbf{C})\mathbf{e}(t) + \mathbf{d}_1(t) - \mathbf{K}\mathbf{d}_2(t) \\ \mathbf{r}(t) &= \mathbf{C}\mathbf{e}(t) + \mathbf{d}_2(t) \end{aligned} \tag{5.12}$$

where

$$\dot{\mathbf{e}}(t) = \dot{\mathbf{x}}(t) - \dot{\hat{\mathbf{x}}}(t) \tag{5.13}$$

Taking the Laplace transform of Equation 5.12 yields

$$\begin{aligned} \mathbf{r}(s) = {} & \mathbf{C}(s\mathbf{I} - \mathbf{A} + \mathbf{K}\mathbf{C})^{-1}\mathbf{d}_1(s) \\ & + (\mathbf{I} - \mathbf{C}(s\mathbf{I} - \mathbf{A} + \mathbf{K}\mathbf{C})^{-1}\mathbf{K})\mathbf{d}_2(s) \end{aligned} \tag{5.14}$$

Subsequently, the effects of model-plant mismatch and disturbances can be minimised by minimising the following performance indices:

$$J_1(\mathbf{K}) = \left\|\mathbf{C}(s\mathbf{I} - \mathbf{A} + \mathbf{KC})^{-1}\right\|_\infty \tag{5.15}$$

$$J_2(\mathbf{K}) = \left\|\mathbf{I} - \mathbf{C}(s\mathbf{I} - \mathbf{A} + \mathbf{KC})^{-1}\mathbf{K}\right\|_\infty \tag{5.16}$$

where $\|.\|_\infty$ denotes L_∞ norm, also known as the infinity norm. By minimising $J_1(\mathbf{K})$ and $J_2(\mathbf{K})$, the maximums of the largest singular values of $\mathbf{C}(s\mathbf{I} - \mathbf{A} + \mathbf{KC})^{-1}$ and $\mathbf{I} - \mathbf{C}(s\mathbf{I} - \mathbf{A} + \mathbf{KC})^{-1}\mathbf{K}$, which correspond to the peak gains of the frequency response, are minimised. Hence, the effects of model-plant mismatch and disturbances can be minimised.

If enough information is given to determine $\Delta\mathbf{A}$, $\Delta\mathbf{B}$, $\Delta\mathbf{C}$, $\mathbf{E}_1$, and $\mathbf{E}_2$, these matrices can be incorporated into Equation 5.14. As a result, the effects of model-plant mismatch and disturbances may be minimised even further resulting in improved controller performance. If exact values of these matrices can be found, the performance of the new controller design would be nearly perfect. However, it can be very difficult to determine the matrices that describe modelling errors and disturbances precisely. Nonetheless, even without the incorporation of these matrices, the controller still performs very well as simulation results demonstrate in Section 5.3.

The problem now is to find $\mathbf{K}$ such that $J_1(\mathbf{K})$ and $J_2(\mathbf{K})$ are minimised. However, it is likely that $\mathbf{K}$ causes instability which can be prevented by parameterising $\mathbf{K}$ via the eigenstructure assignment method summarised below.

5.2.1.2 Parameterisation via Eigenstructure Assignment Method

When conducting an optimisation to minimise $J_1(\mathbf{K})$ and $J_2(\mathbf{K})$ in Equations 5.15 and 5.16, it is important to ensure that the stability of the observer is always guaranteed, and this leads to more complex constrained optimisation problem. To guarantee the stability condition, Chen and Patton (1999) suggest the use of the eigenstructure assignment method which parameterises $\mathbf{K}$. The method has an advantage of allowing the eigenvalues in predefined regions and is summarised here. Before describing the eigenstructure assignment method, the concept of "duality" is revised as follows.

Lemma 5.1. *The problem of designing an observer is equivalent to solving the pole-placement problem of the dual system.*

Proof. Consider a regulator system (Grimble and Johnson, 1988; Ogata, 2002) described by the following equations

$$\begin{aligned} \dot{\mathbf{x}}(t) &= \mathbf{A}\mathbf{x}(t) + \mathbf{B}\mathbf{u}(t) \\ \mathbf{y}(t) &= \mathbf{C}\mathbf{x}(t) \end{aligned} \tag{5.17}$$

where the control signal is given by

$$\mathbf{u}(t) = -\mathbf{K}_f\mathbf{x}(t) \tag{5.18}$$

Its dual system can be written as follows (O'Reilly, 1983):

$$\begin{aligned} \dot{\mathbf{z}}(t) &= \mathbf{A}^T\mathbf{z}(t) + \mathbf{C}^T\mathbf{v}(t) \\ \mathbf{n}(t) &= \mathbf{B}^T\mathbf{z}(t) \end{aligned} \tag{5.19}$$

where the control signal can be defined as

$$\mathbf{v}(t) = -\mathbf{K}_e\mathbf{z}(t) \tag{5.20}$$

The pole-placement technique (Dorf and Bishop, 2008; Wilkie et al., 2002) demonstrates that the stability of the regulator system is determined by the eigenvalues of $\mathbf{A} - \mathbf{B}\mathbf{K}_f$, and the stability of the dual system must therefore be determined by the eigenvalues of $\mathbf{A}^T - \mathbf{C}^T\mathbf{K}_e$. Since the eigenvalues of a square matrix, $\mathbf{X}$ are the same as the eigenvalues of the inverse of $\mathbf{X}$, the eigenvalues of $\mathbf{A}^T - \mathbf{C}^T\mathbf{K}_e$ must equal the eigenvalues of $\mathbf{A} - \mathbf{K}_e^T\mathbf{C}$.

Moreover, the first line of Equation 5.12 suggests that the stability of the observer is determined by the eigenvalues of $\mathbf{A} - \mathbf{K}\mathbf{C}$. Therefore, using the matrix $\mathbf{K}_e$ determined by the pole-placement approach in the dual system, the observer gain matrix, $\mathbf{K}$ for the original system can be determined by using the relationship $\mathbf{K} = \mathbf{K}_e^T$. □

The proposed controller design makes a simplifying assumption that the eigenvalues are always real. Since the observer design problem is the dual problem of the controller design, $\mathbf{v}_i$ is the i_{th} eigenvector of $\mathbf{A}^T - \mathbf{C}^T\mathbf{K}^T$ corresponding to the i_{th} eigenvalue, λ_i as follows:

$$(\mathbf{A}^T - \mathbf{C}^T\mathbf{K}^T)\mathbf{v}_i = \lambda_i\mathbf{v}_i \tag{5.21}$$

$$\mathbf{v}_i = -(\lambda_i\mathbf{I} - \mathbf{A}^T)^{-1}\mathbf{C}^T\mathbf{w}_i \tag{5.22}$$

where $\mathbf{w}_i = \mathbf{K}^T\mathbf{v}_i$. In turn, there are two design parameters, $\mathbf{w}_i$ and λ_i instead of one design parameter, $\mathbf{K}$. These design parameters still do not guarantee the stability of the observer.

The eigenvalue, λ_i, one of the design parameters, is generally not required to be placed at a specific point in the s or z-planes but is generally required to be placed rather in a predefined region to satisfy the stability condition. This in turn provides more relaxed design freedom as

$$\lambda_i \in [L_i, U_i] \tag{5.23}$$

where L_i and U_i (for $i = 1, \ldots n$) respectively denote the upper and lower bounds. By defining an equation for the eigenvalue as

$$\lambda_i = L_i + (U_i - L_i sin^2(z_i)) \tag{5.24}$$

$z_i \in \mathbb{R}$ $(i = 1, \ldots, n)$ becomes a design parameter replacing λ_i. Any z_i ensures that λ_i is always within the bounds, thereby guaranteeing the stability condition.

Finally, the two design parameter vectors, $\mathbf{W}$ and $\mathbf{Z}$ have been defined, and the performance indices in Equations 5.15 and 5.16 can be rewritten as follows:

$$J_1(\mathbf{W}, \mathbf{Z}) = \left\|\mathbf{C}(s\mathbf{I} - \mathbf{A} + \mathbf{KC})^{-1}\right\|_\infty \tag{5.25}$$

$$J_2(\mathbf{W}, \mathbf{Z}) = \left\|\mathbf{I} - \mathbf{C}(s\mathbf{I} - \mathbf{A} + \mathbf{KC})^{-1}\mathbf{K})\right\|_\infty \tag{5.26}$$

where

$$\mathbf{K} = [\mathbf{W}\mathbf{V}^{-1}]^T \tag{5.27}$$

Having redefined the multi-objective optimisation problem as finding **Z** and **W** from finding **K** only, the stability condition is always guaranteed.

Since, two performance indices Equations 5.25 and 5.26 need to be minimised simultaneously, a multi-objective optimisation technique can be useful. However, unlike the multi-objective problem addressed in Chapter 6, the minimisation of J_1 does not tend to contradict with that of J_2. This implies that the minimisation of either J_1 or J_2 can be sufficient. Still, if the multi-objective optimisation was required, the method reported in Section 6.2 could be used.

5.2.2 Dynamic Compensation

Bump test results can be used to approximate the dynamic response of the plant as

$$h(z^{-1}) = \frac{1-\alpha}{1-\alpha z^{-1}} z^{-k} \tag{5.28}$$

which has the same structure as the dynamic component of the model given in Equation 5.1. One of the benefits of utilising the proposed controller design was not having to separate the spatial component from the dynamic component of the reference model. Although the bump tests provide the dynamic response of the model, the benefit claimed is still valid as the spatial component of the model is still unknown.

The generic IMC design illustrated in Figure 5.3 usually designs $G_c(z^{-1})$ as the inverse of the reference model $\tilde{G}_p(z^{-1})$ so that if $\tilde{G}_p(z^{-1})$ is equal to $G_p(z^{-1})$, $y(t)$

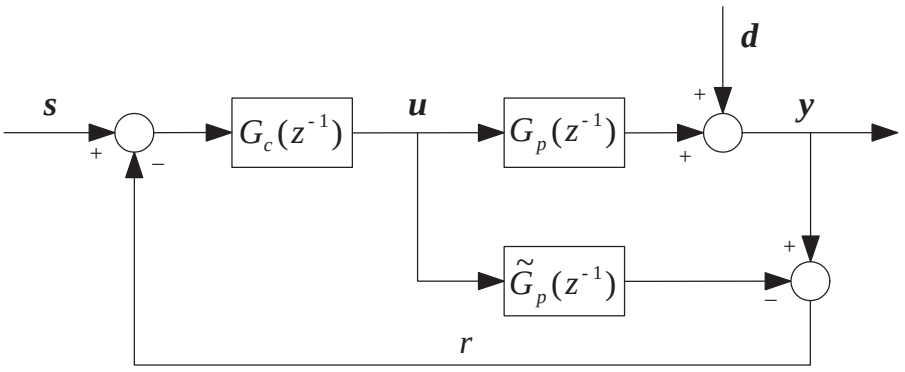

FIGURE 5.3: Generic IMC design

is also equal to $s(t)$ when there is no disturbance. However, $\tilde{G}_p(z^{-1})$ is usually non-invertible and thus needs to be factorised into invertible and non-invertible components beforehand as follows:

$$\tilde{G}_p(z^{-1}) = \tilde{G}_p^+(z^{-1})\tilde{G}_p^-(z^{-1}) \tag{5.29}$$

where the invertible component is given by

$$\tilde{G}_p^+(z^{-1}) = \frac{1-\alpha}{1-\alpha z^{-1}} \tag{5.30}$$

Non-invertible components may contain terms which lead to stability or realisability problems if inverted, such as terms containing positive zeros and time delays (Tham, 2002). In this example, the non-invertible component contains z^{-1}, which leads to a realisability problem.

Subsequently, $G_c(z^{-1})$ can be designed as the inverse of $\tilde{G}_p^+(z^{-1})$. Furthermore, the effect of model-plant mismatch can be minimised to improve robustness. Since mismatches generally occur at the high frequency region of the frequency response, a low-pass filter, $G_f(z^{-1})$ is usually added to attenuate the effect of model-plant mismatch as follows:

$$G_c(z^{-1}) = [\tilde{G}_p^+(z^{-1})]^{-1} G_f(z^{-1}) \tag{5.31}$$

where

$$G_f(z^{-1}) = \frac{1-\beta}{1-\beta z^{-1}} \tag{5.32}$$

Substituting Equation 5.30 into Equation 5.31, the equation for the dynamic compensator is

$$G_c(z^{-1}) = \left(\frac{1-\alpha z^{-1}}{1-\alpha}\right)\left(\frac{1-\beta}{1-\beta z^{-1}}\right) \tag{5.33}$$

For the proposed controller design, the same dynamic compensator is used for each CD section (or lane), and the dynamic compensator, $\mathbf{G}_c(z^{-1})$ in Figure 5.2 is therefore given as follows:

$$\mathbf{G}_c(z^{-1}) = G_c(z^{-1})\mathbf{I}_N \tag{5.34}$$

where $\mathbf{I}_N$ is the identity matrix, and β is the only tuning parameter for the proposed controller design.

5.2.3 Steady State Performance

For the optimal steady state actuator setting of the controller, a new objective function needs to be introduced as follows.

Optimal steady state performance can be achieved by minimising $\|\mathbf{y}(t)\|_2 = \|\tilde{\mathbf{y}}(t) + \mathbf{r}(t)\|_2$ where $\tilde{\mathbf{y}}(t)$ is given in Equation 5.9 and $\|.\|_2$ denotes L_2 norm.

In the steady state, $\dot{\tilde{\mathbf{x}}}(t)$ in Equation 5.9 is equal to zero and therefore the equation becomes

$$\tilde{\mathbf{x}}(t) = -\mathbf{A}^{-1}\mathbf{B}u(t) - \mathbf{A}^{-1}\mathbf{K}\mathbf{r}(t) \tag{5.35}$$

Substituting Equation 5.35 into the following

$$\tilde{\mathbf{y}}(t) = \mathbf{C}\tilde{\mathbf{x}}(t) \tag{5.36}$$

$\tilde{\mathbf{y}}(t)$ can be derived as

$$\tilde{\mathbf{y}}(t) = -\mathbf{C}\mathbf{A}^{-1}\mathbf{B}\mathbf{u}(t) - \mathbf{C}\mathbf{A}^{-1}\mathbf{K}\mathbf{r}(t) \tag{5.37}$$

Since $\mathbf{y}(t) = \tilde{\mathbf{y}}(t) + \mathbf{r}(t)$, the equation for $\mathbf{y}(t)$ is as follows:

$$\mathbf{y}(t) = -\mathbf{C}\mathbf{A}^{-1}\mathbf{B}\mathbf{u}(t) + (\mathbf{I} - \mathbf{C}\mathbf{A}^{-1}\mathbf{K})\mathbf{r}(t) \tag{5.38}$$

Hence, optimal steady state performance can be attained with

$$\mathbf{u}_{ss}(t) = \arg\min_{\mathbf{u}(t)} \left\| -\mathbf{C}\mathbf{A}^{-1}\mathbf{B}\mathbf{u}(t) + (\mathbf{I} - \mathbf{C}\mathbf{A}^{-1}\mathbf{K})\mathbf{r}(t) \right\|_2 \tag{5.39}$$

where $\mathbf{u}(t) \in \mathbb{R}^N$ is subject to constraints, such as actuator saturation, fixed mean set-point, and bending constraints. As mentioned in Section 5.1.2, bending constraints usually do not apply to plastic film manufacturing processes, and in

practice, the mean of the set-points is constrained to equal the fixed "operating mean", which can range from 40% to 60%, in order to discourage actuator saturation.

The non-linear element (NL) in Figure 5.2 continuously produces the control action using Equation 5.39. In order to solve the quadratic programming required for Equation 5.39, " fmincon" function provided by the Optimization Toolbox™4.3 can be utilised.

5.2.4 Computational Structure of the Controller

The proposed controller design can be summarised as follows (Figure 5.2):

1. *Derivation of a reference model*: Using the System Identification Toolbox™7 in Matlab, a reference model in the state space form is derived (Appendix B).

2. *Construction of an observer and derivation of an optimal observer gain*, **K**: An observer is constructed in order to find **K** for minimising the effects of model-plant mismatch and disturbances. The stability of the observer is guaranteed by the use of the eigenstructure assignment method summarised in Section 5.2.1.

3. *Dynamic compensation*: For dynamic compensation, the IMC design is employed (Section 5.2.2). At this stage, β in Equation 5.32 is determined.

4. *Steady state performance*: Online optimisation is conducted to calculate optimal control action, $\mathbf{u}_{ss}(t)$ by continuously solving Equation 5.39.

5.3 Simulation and Implementation

A number of simulations have been conducted to demonstrate how the controller performs, and three of these simulations are presented here. These simulations have been conducted not only for the proposed controller but also for the industrial controller and model-based controller reported in Section 5.1 for comparison purposes.

Figures 5.4, 5.6, and 5.8 show the steady state CD thickness profile measured by the scanning gauge and the corresponding actuator set-points. Red plots are for the proposed controller and labelled "Proposed" ; blue plots are for the industrial controller and labelled "Industrial"; and black plots are for the model based controller and labelled "IMC". It is assumed that the film is divided into 10 lanes (Section 4.1.1). To simulate what happens in real life, the edges – the first and last lanes – are not controlled and left open-loop instead. Therefore, the figures do not show the first and last lanes. The y-axes represent thickness in percentage deviation from the mean, and the x-axes denote the CD position.

The existing controllers reported in Section 5.1 employ the model given in Equation 5.1 as the reference model. However, for the proposed controller design, the System Identification Toolbox™7 has been utilised to identify a reference model in the state-space form directly from the first-principles model, which is introduced in the previous chapters and is used to simulate the plant throughout this thesis. The model in Equation 5.1, on the other hand, has been identified directly from the real plant as opposed to the first-principles model. Although the first-principles model has been developed to simulate the plant, a mismatch between the plant and the first-principles model still exists. Therefore, the existing controllers would experience larger model-plant mismatch than the proposed controller making the comparison unfair. As a result, the reference model for all controllers has been identified using the model in Equation 5.1 instead of the first-principles model to make the comparison fairer.

If the reference model is identified from the first-principles model, improved performance of the proposed controller can be expected. It is also important to point out that the industrial controller has been tuned to work optimally with the plant as opposed to the first-principles model, which implies that improved performance of the industrial controller can also be expected with improved tuning parameters. Furthermore, the IMC controller reported in Section 5.1 has a number of different versions and the use of a different version may also improve the performance of the IMC controller.

Subsequently, all the controllers have been applied to the first-principles model, and the simulation results are summarised as follows.

5.3.1 Simulation 1

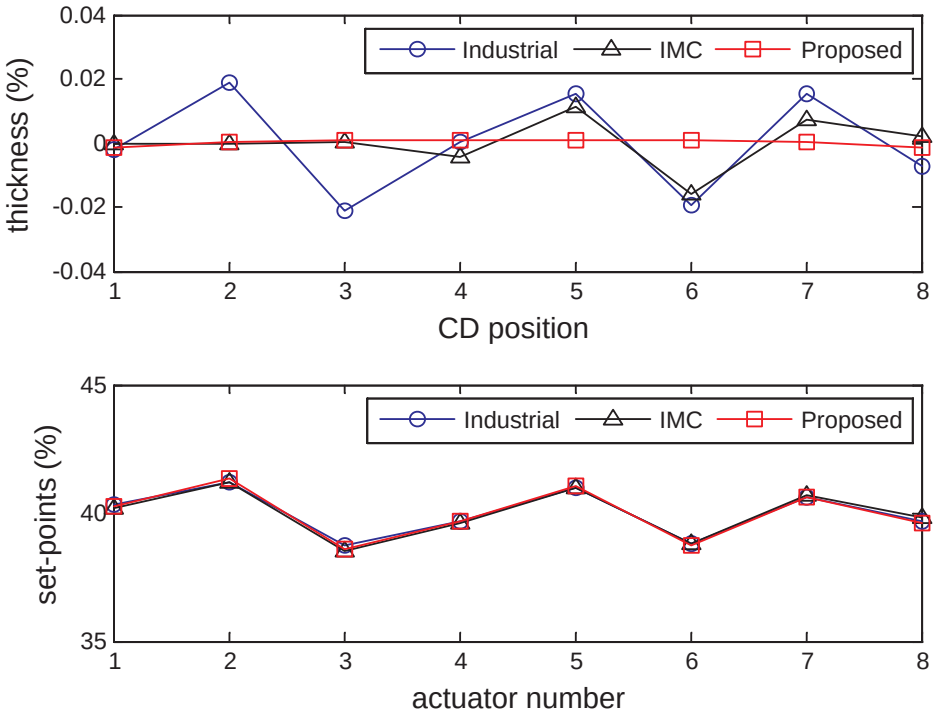

FIGURE 5.4: Simulation 1: Steady state CD thickness profile under normal operational conditions; Only model-plant mismatch exists

In Simulation 1, the proposed controller achieves a noticeable improvement over the existing controllers under normal operating conditions as shown in Figure 5.4. Although no disturbances are present, the set-points are not flat because model-plant mismatch exists under normal operating conditions since the model can never be 100% accurate. Moreover, the reference model for every controller has been identified from Equation 5.1 instead of the first-principles model leading to even larger model-plant mismatch. Although the proposed controller design aims to minimise this mismatch, it cannot be fully eliminated. The result demonstrates the insensitivity of the proposed controller to modelling errors (model-plant mismatch) relative to the existing controllers.

However, the corresponding dynamic responses depicted in Figures 5.5 demonstrate that the industrial controller has a better dynamic response than the others. This is because although the dynamic performance of the model-based controllers

is compensated to some degree by the compensator shown in Equation 5.33, these controllers focus more on the steady state performance by solving the online optimisation problems shown in Equations 5.8 and 5.39.

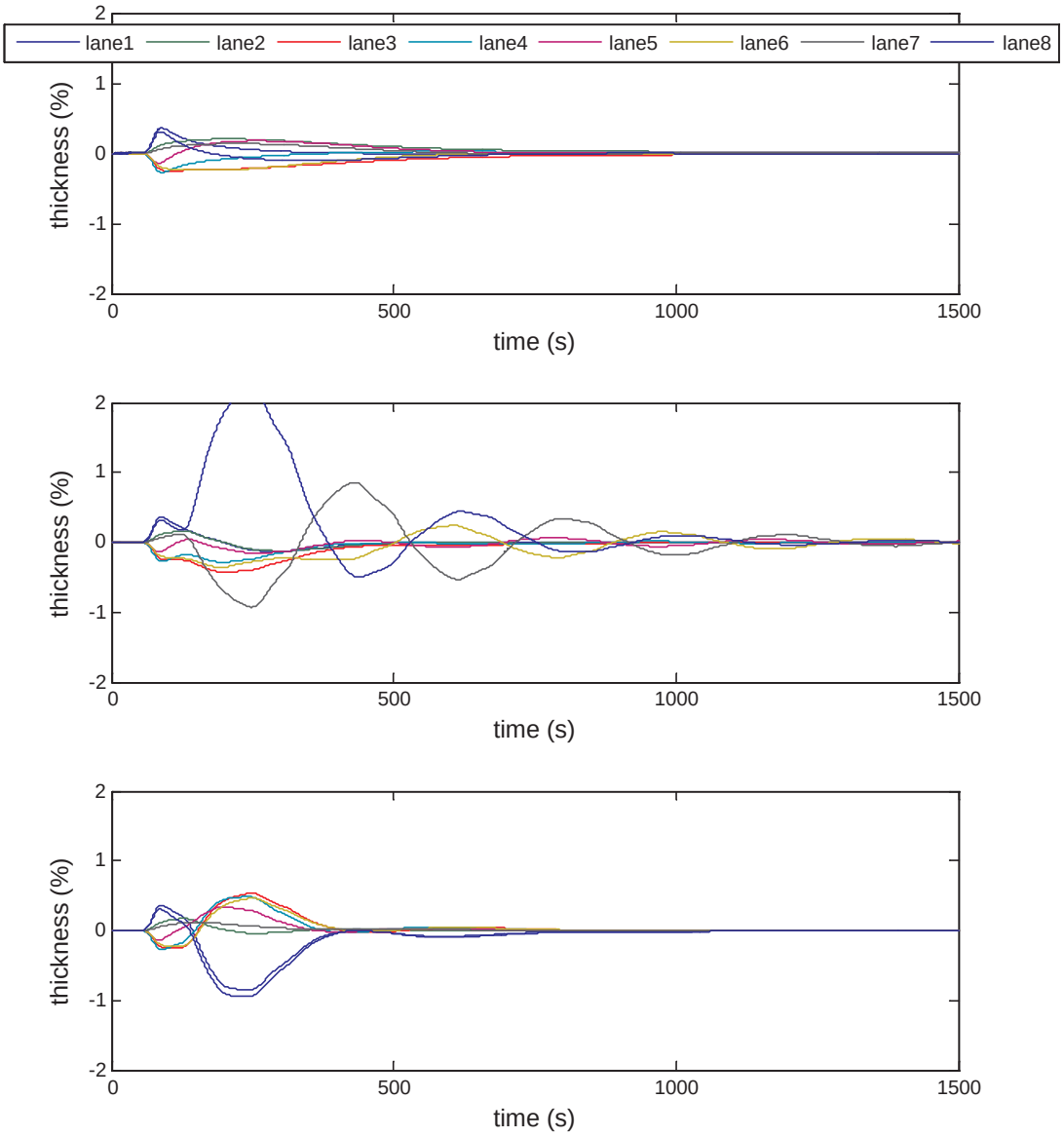

FIGURE 5.5: Simulation 1: Plots from top to bottom: dynamic response of industrial controller, IMC controller, and proposed controller

5.3.2 Simulation 2

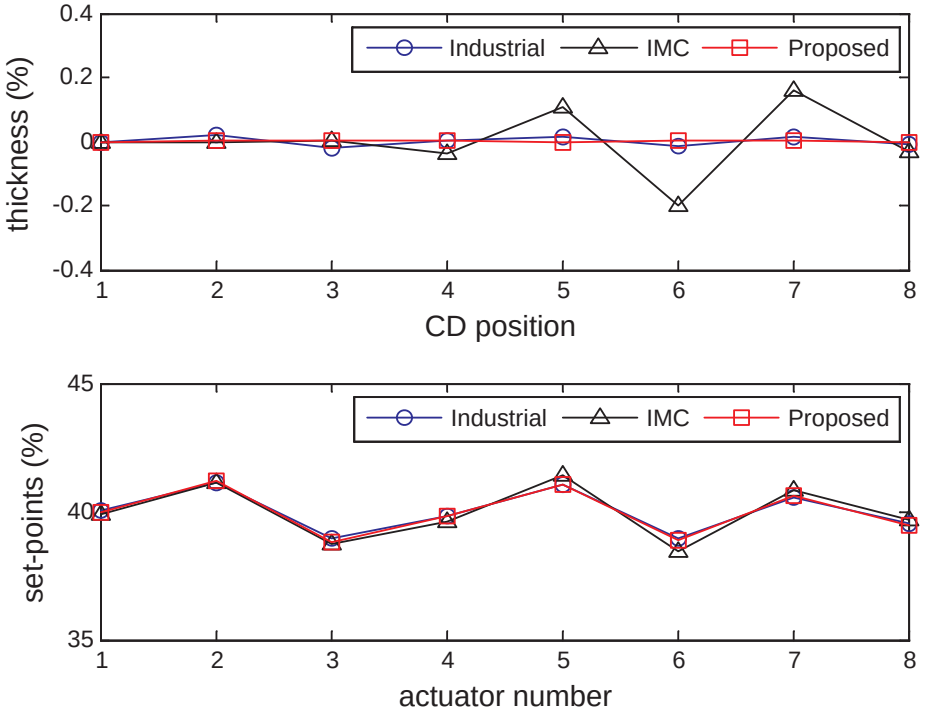

FIGURE 5.6: Simulation 2: Steady state CD thickness profile with fast-nip roll speed variation from $t = 0s$; y-axis of upper plot has a different range from those in Figures 5.4 and 5.8

In Simulation 2, there exists persistent (from $t = 0$) variation in fast-nip roll speed. The speed varies randomly within $\pm 10\%$ of the desired speed. The proposed controller achieves a noticeable improvement over the IMC controller and a slight improvement over the industrial controller as illustrated in Figure 5.6. The corresponding dynamic responses depicted in Figures 5.7 demonstrate that the industrial controller has a somewhat better dynamic response than the proposed controller because it experiences less fluctuation.

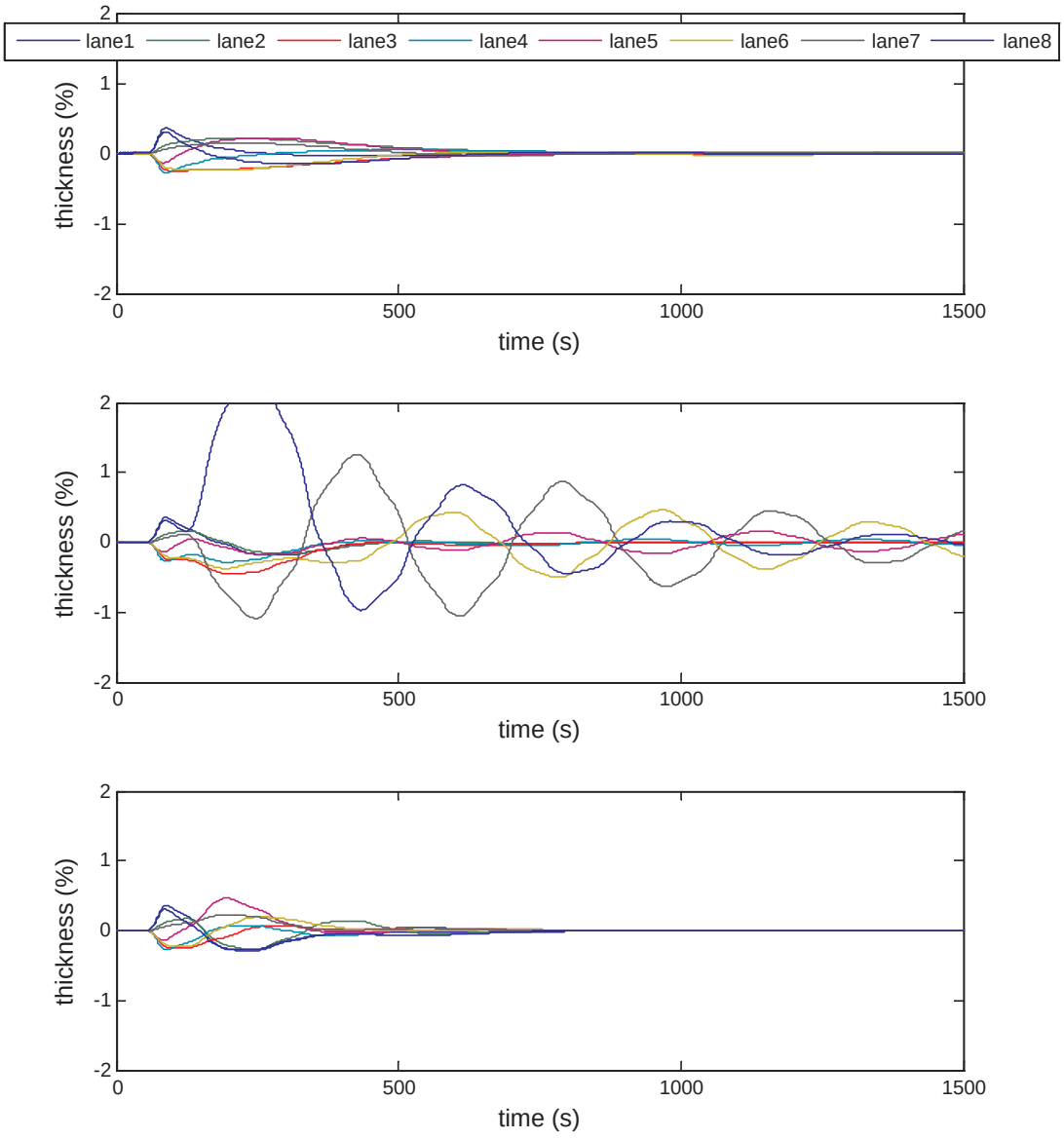

FIGURE 5.7: Simulation 2: Plots from top to bottom: dynamic response of industrial controller, IMC controller, and proposed controller

5.3.3 Simulation 3

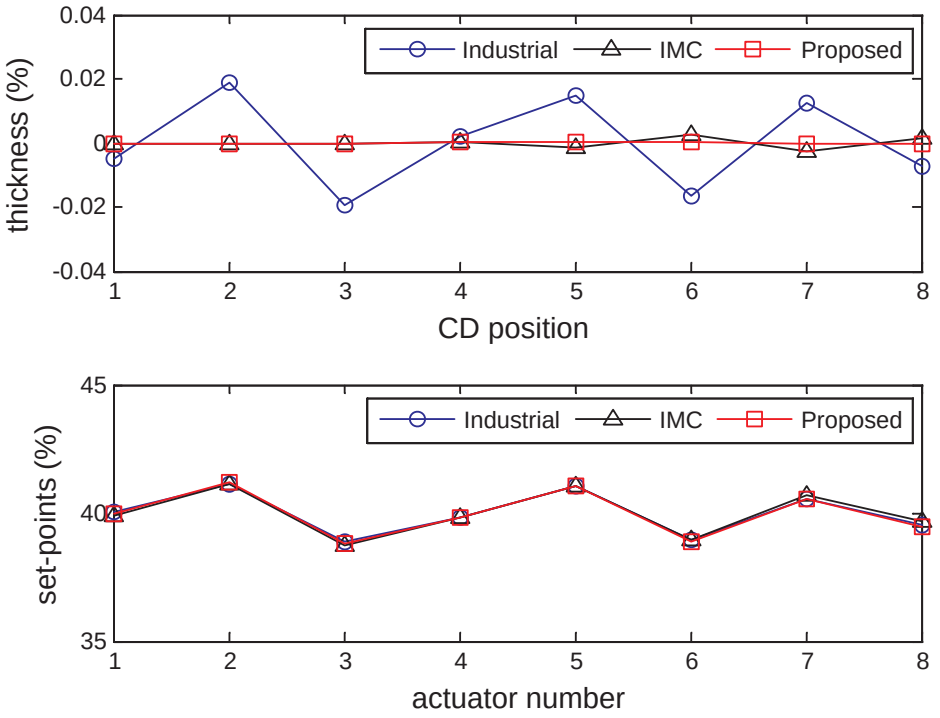

FIGURE 5.8: Simulation 3: Steady state CD thickness profile with mass flow variation from $t = 3000s$

A polymer melt is fed into the die at a certain mass flow rate (Section 2.2). In Simulation 3, mass flow rate starts to vary suddenly from $3000s$ in contrast to Simulation 2, where the variation occurs from $0s$. One purpose of this simulation is to see how the controller responds to a disturbance appearing suddenly. Mass flow rate varies randomly within $\pm 10\%$ of the desired rate. Figure 5.8 shows that the proposed controller achieves a noticeable improvement over the industrial controller but has a similar performance to the IMC controller. However, the dynamic responses depicted in Figure 5.9 indicate that the proposed controller rejects the distrubance noticeably faster than the IMC controller.

Figures 5.4, 5.6 and 5.8 depict that the steady state actuator set-points for all the controllers are close to each other for each simulation. Despite the close actuator set-points, the thickness profiles look quite different when they may be expected to be close to each other. This is because when the set-points of the industrial

controller reach the steady state, the online optimisation used for solving Equation 5.8 for the IMC controller and Equation 5.39 for the proposed controller hardly stops fine-tuning the controllers, thereby improving the thickness profiles even further as shown in Figures 5.5, 5.7, and 5.9.

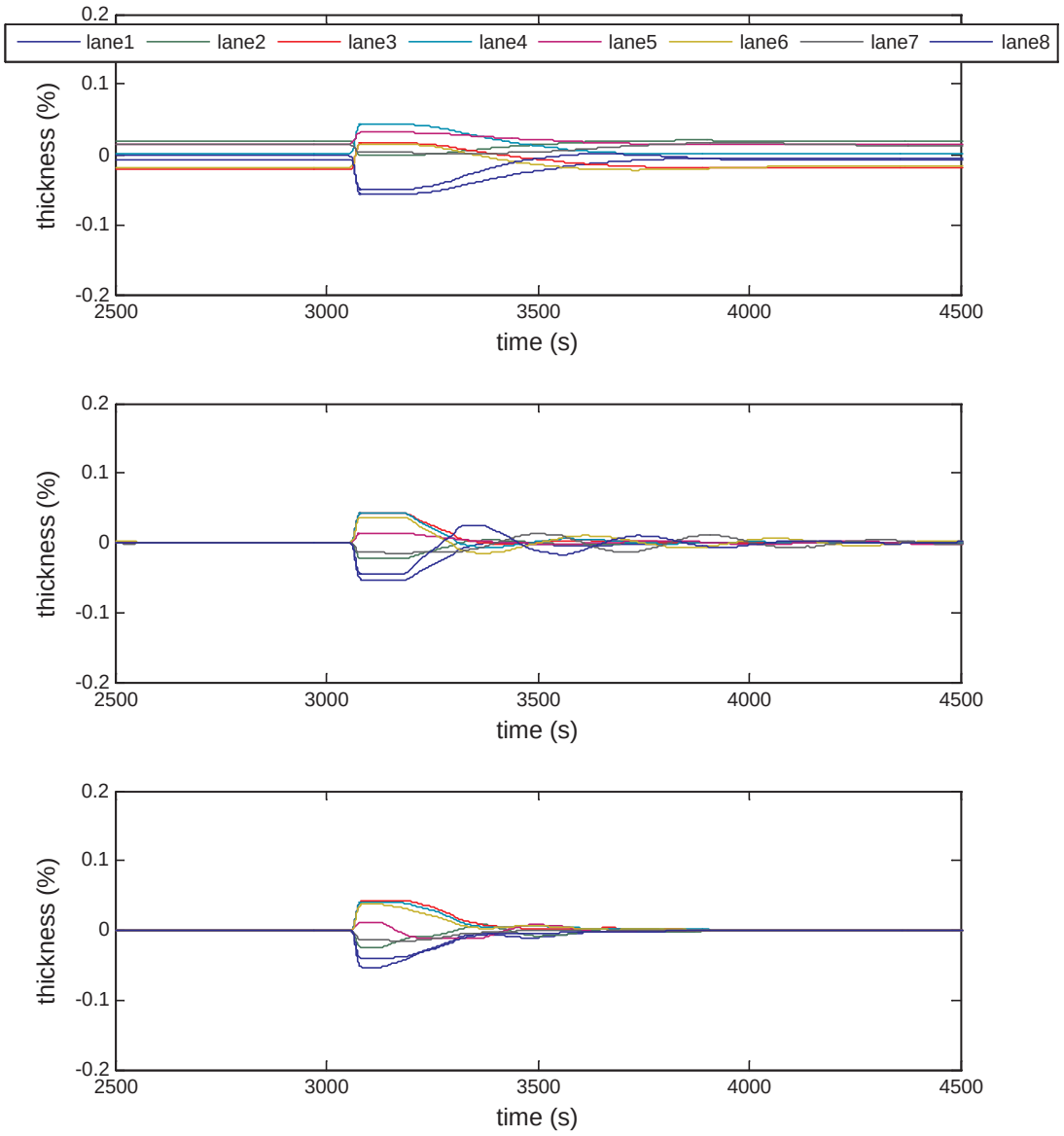

FIGURE 5.9: Simulation 3: Plots from top to bottom: dynamic response of industrial controller, IMC controller, and proposed controller; y-axes have a different range from those in Figures 5.5 and 5.7

5.4 Summary

This chapter has reported the development of a new model-based CD controller design and its application to the first-principles model introduced in the previous chapters. The controller is based on IMC to compensate for the dead time, but utilises an observer whose gain is designed to minimise the effects of model-plant mismatch and disturbances. The optimal steady state performance is encouraged and actuator saturation is discouraged by introducing a new objective function that needs to be optimised online subject to constraints. Moreover, the controller benefits from not having to separate the dynamic component from the spatial component of the reference model unlike the existing controllers studied in this chapter.

Simulations provide comparison between the proposed controller and other existing controllers under different disturbance scenarios. The results demonstrate improvements that the proposed controller can achieve compared with the existing controllers, one of which is commonly used in real life. The improvements are mainly due to the observer design.

The controller design is a novel approach since no other controller has incorporated an observer to minimise the effects of model-plant mismatch and disturbances, which leads to a new online optimisation problem for the optimal steady state actuator setting of the controller. The design can also be used for controlling other sheet-forming processes such as papermaking and metal-rolling.

Chapter 6

Fault Monitoring

Modern industrial processes include closed-loop control systems that can compensate for various types of disturbances, but there are changes in the process that the control systems are not able to compensate for adequately. These changes are referred to as faults. More precisely, a fault can be defined as an unpermitted deviation of at least one characteristic property or variable of the process (Isermann and Ball, 1996). The types of faults occurring in industrial processes include actuator faults, sensor faults, and component faults, also known as process faults. Examples of actuator, sensor, and component faults are respectively stuck die bolt, which is the actuator for the plastic film manufacturing process, a biased sensor measurement, and process parameter changes.

For industrial processes to satisfy performance specifications, any faults should be detected and diagnosed properly as discussed in Section 1.2. This process can be realised by applying a fault detection and diagnosis (FDD) system, which can be data-driven, knowledge-based, or model-based (Chiang et al., 2001). The data-driven approach requires data directly from the real-life process. Typical modern industrial systems produce very large amount of data, and thus it is usually not feasible for the plant operators to effectively assess process operations simply from observing the data. The data-driven approach therefore employs a dimensionality reduction technique, such as principle component analysis (PCA), fisher discriminant analysis (FDA), and partial least squares (PLS) (Piovoso and Kosanovich, 1994; Venkatasubramanian et al., 2005; Wise and Gallagher, 1996) to transform the high-dimensional data into a lower dimension, in which the

important information is captured. By producing some meaningful statistics for the plant operators, the performance of a FDD system can improve significantly. The main drawback of this approach is that its efficiency is highly dependent on the quantity and quality of the process data.

The knowledge-based approach employs a qualitative model using a pattern recognition technique such as neural networks and self-organising maps (Iri et al., 1979; Patton et al., 1994; Venkatasubramanian et al., 2004). Such a model is a black-box model that learns the patterns entirely from training sessions. This approach is suitable when no detailed mathematical models are available. While the data-driven approach is applicable to both large and small-scale systems, the knowledge-based approach is more suitable for small-scale systems with relatively smaller number of inputs, outputs, and states.

The model-based approach exploits a detailed mathematical model (e.g. first-principles model) to generate residuals via consistency checks between the plant observations and mathematical model. The three main ways to generate residuals are observers, parameter estimation, and parity relations (Himmelblau, 1978; Simani et al., 2003; Venkatasubramanian et al., 2003). The main drawback of this approach is that a detailed mathematical model is required, but the development of such a model for especially large-scale systems may be too costly and time-consuming. The main advantage of this approach, however, is the ability to incorporate physical understanding of the process into the FDD system. Therefore, when a detailed mathematical model is available, this approach can significantly outperform the data-driven and knowledge-based approaches.

In this chapter, a model-based FDD system is developed and applied to a data set extracted from the real-life process and also to the first-principles model reported in Chapters 3 and 4. Residual generation can be the most important task in FDD, and residual generation via parity relations is presented in Section 6.1. Optimal residuals need to be sensitive to faults but insensitive to other unknown inputs, such as disturbances and modelling errors, which leads to a multi-objective optimisation problem. Several analytical methods for solving this multi-objective optimisation problem have been suggested (Frank, 1990; Lou et al., 1986). By contrast, the FDD system proposed in this chapter utilises an evolutionary algorithm (Konak et al., 2006) or more specifically, a genetic algorithm (Davis, 1991; Frenzel, 1993), for solving this multi-objective optimisation problem in Section

6.2. The use of a genetic algorithm increases the possibility of finding the global optimisation solution – global minimum – by avoiding the calculation of cost function gradients, which can lead to local minima. Another advantage is that it is relatively straightforward to understand and implement.

Patton et al. (1997) employed the combination of a genetic algorithm, the method of inequalities, and the moving-boundaries algorithm for optimising an observer based residual generator. However, this combination has never been used to optimise a parity relation based residual generator in any literature. The parity relation based residual generation has a few advantages over the observer based residual generation. Unlike the observer approach, the parity relation approach does not convert the reference model into the frequency domain for the multi-objective optimisation. Because the conversion needs to be performed at every iteration during the multi-objective optimisation, this can increase the computation time required for the optimisation significantly. Also, there is no need to employ an extra algorithm, such as the eigenstructure assignment method (Section 5.2) for guaranteeing the stability condition. The plant observation for a plastic film manufacturing process is the cross-directional (CD) thickness profile (Featherstone et al., 2000), which needs to be divided into many sections for controlling and monitoring purposes. When the observer approach is employed, the number of the residual signals equals the number of the CD sections and, therefore, determining the thresholds can be difficult or the use of a dimensionality reduction technique (Kresta et al., 1991; Piovoso et al., 1994) is required. However, when the parity relation approach is employed, all the residuals are arranged under one signal, and this makes the parity relation approach more suitable for plastic film manufacturing and other sheet-forming processes.

The application of this FD system to the first-principles model studied in Chapters 3 and 4 is presented with simulation results in Section 6.3. The next stage is to determine which fault has occurred, and this stage is often referred to as fault diagnosis. Many books and papers focus more on fault detection, and fault diagnosis is often neglected. Nevertheless, Section 6.4 deals with fault diagnosis. The FD system is modified to a fault detection and diagnosis (FDD) system, and the application of this FDD system to the first-principles model is demonstrated in the section. Moreover, the FDD system is applied to data extracted from

the industrial process in Section 6.5, followed by the summary of this chapter in Section 6.6.

6.1 Residual Generation via Parity Relations

The residual generation via parity relation requires a model in the state space form as follows:

$$\mathbf{x}(k+1) = \mathbf{A}\mathbf{x}(k) + \mathbf{B}\mathbf{u}(k) \tag{6.1}$$

$$\mathbf{y}(k) = \mathbf{C}\mathbf{x}(k) + \mathbf{D}\mathbf{u}(k) \tag{6.2}$$

where $\mathbf{y}(k) \in \mathbb{R}^N$ denotes the process measurements, $\mathbf{u}(k) \in \mathbb{R}^N$ is the control action, $\mathbf{x}(k) \in \mathbb{R}^R$ represents the states, and $\mathbf{D}$ is a zero matrix. The identification of the continuous version of this discrete model from the first-principles model is presented in Appendix B.

Substituting Equation 6.1 into Equation 6.2 from time instant $k-s$ to time instant k to collect 's+1' samples of $\mathbf{y}$ and $\mathbf{u}$ as illustrated in Figure 6.1 gives

$$\begin{bmatrix} \mathbf{y}(k-s) \\ \mathbf{y}(k-s+1) \\ \vdots \\ \mathbf{y}(k) \end{bmatrix} - \mathbf{H} \begin{bmatrix} \mathbf{u}(k-s) \\ \mathbf{u}(k-s+1) \\ \vdots \\ \mathbf{u}(k) \end{bmatrix} = \mathbf{W}\mathbf{x}(k-s) \tag{6.3}$$

where s denotes delay, and $\mathbf{H}$ and $\mathbf{W}$ are given by

$$\mathbf{H} = \begin{bmatrix} \mathbf{D} & \mathbf{0} & \cdots & \mathbf{0} \\ \mathbf{CB} & \mathbf{D} & \cdots & \mathbf{0} \\ \vdots & \vdots & \ddots & \vdots \\ \mathbf{CA}^{s-1}\mathbf{B} & \mathbf{CA}^{s-2}\mathbf{B} & \cdots & \mathbf{D} \end{bmatrix} \tag{6.4}$$

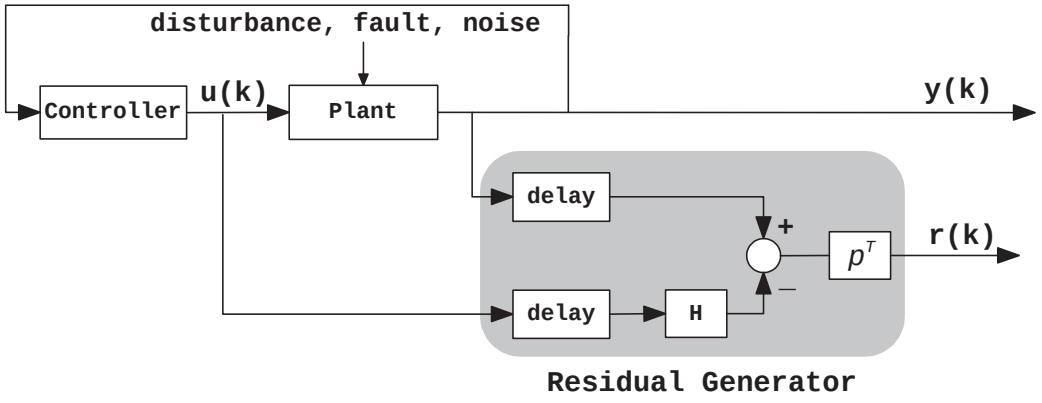

FIGURE 6.1: Parity relation based residual generation

$$\mathbf{W} = \begin{bmatrix} \mathbf{C} \\ \mathbf{CA} \\ \vdots \\ \mathbf{CA}^s \end{bmatrix} \tag{6.5}$$

To remove the non-measurable states, $\mathbf{x}(k-s)$, $\mathbf{p} \in \mathbb{R}^{N(s+1)}$ shown in the figure can be chosen such that

$$\mathbf{p}^T\mathbf{W} = 0$$

In turn, Equation 6.3 becomes

$$\mathbf{p}^T\mathbf{Y}(k) = \mathbf{p}^T\mathbf{H}\mathbf{U}(k) \tag{6.6}$$

where

$$\mathbf{Y}(k) = \begin{bmatrix} \mathbf{y}(k-s) \\ \mathbf{y}(k-s+1) \\ \vdots \\ \mathbf{y}(k) \end{bmatrix} \tag{6.7}$$

$$\mathbf{U}(k) = \begin{bmatrix} \mathbf{u}(k-s) \\ \mathbf{u}(k-s+1) \\ \vdots \\ \mathbf{u}(k) \end{bmatrix} \tag{6.8}$$

leading to an equation for the residual, $r(k) \in \mathbb{R}^1$ as

$$r(k) = \mathbf{p}^T\mathbf{Y}(k) - \mathbf{p}^T\mathbf{H}\mathbf{U}(k) \tag{6.9}$$

Thus far, unknown inputs, which can include faults, noise, and disturbances, have been neglected because Equations 6.1 and 6.2 exclude them. Modifying the equations such that the unknown inputs are taken into account, the equations become

$$\begin{aligned} \mathbf{x}(k+1) &= \mathbf{A}\mathbf{x}(k) + \mathbf{B}\mathbf{u}(k) + \mathbf{R}_1\mathbf{f}(k) + \mathbf{d}(k) \\ \mathbf{y}(k) &= \mathbf{C}\mathbf{x}(k) + \mathbf{D}\mathbf{u}(k) + \mathbf{R}_2\mathbf{f}(k) \end{aligned} \tag{6.10}$$

where $\mathbf{f}(k) \in \mathbb{R}^N$ denotes the fault signal, and the fault distribution matrices, $\mathbf{R}_1$ and $\mathbf{R}_2$ represent the influence of the faults on the process. These matrices can be determined if one has defined which faults need to be diagnosed. $\mathbf{d}(k)$ can represent any other unknown inputs such as disturbances and modelling errors as follows:

$$\mathbf{d}(k) = \Delta\mathbf{A}\mathbf{x}(k) + \Delta\mathbf{B}\mathbf{u}(k) + \mathbf{E}\tilde{\mathbf{d}}(k) \tag{6.11}$$

where $\mathbf{E}$ is a distribution matrix, and $\tilde{\mathbf{d}}(k)$ is the disturbance signal. $\Delta\mathbf{A}$ and $\Delta\mathbf{B}$ are the parameter errors or variations that represent model-plant mismatch. Although the noise term has been neglected here to simplify the algebra, it needs to be incorporated if the noise is significant compared to the faults or disturbances and if the noise distribution matrix can be approximated.

Subsequently, Equation 6.3 can be modified to

$$\mathbf{Y}(k) - \mathbf{H}\mathbf{U}(k) = \mathbf{W}\mathbf{x}(k-s) + \mathbf{L}\mathbf{N}(k) + \mathbf{M}\mathbf{F}(k) \tag{6.12}$$

where

$$\mathbf{N}(k) = \begin{bmatrix} \mathbf{d}(k-s) \\ \mathbf{d}(k-s+1) \\ \vdots \\ \mathbf{d}(k) \end{bmatrix} \tag{6.13}$$

$$\mathbf{F}(k) = \begin{bmatrix} \mathbf{f}(k-s) \\ \mathbf{f}(k-s+1) \\ \vdots \\ \mathbf{f}(k) \end{bmatrix} \tag{6.14}$$

$\mathbf{L}$ has a similar form to $\mathbf{H}$ in which $\{\mathbf{B}, \mathbf{D}\}$ are replaced by $\{\mathbf{I}_N, \mathbf{0}_{N,N}\}$, where $\mathbf{0}_{N,N}$ is a N-by-N zero matrix and $\mathbf{I}_N$ is the N-by-N identity matrix. When $\mathbf{B}$ is not a square matrix, zeros are appended below or to the right of $\mathbf{I}_N$ appropriately. Similarly, $\mathbf{M}$ is the same as $\mathbf{H}$ except that $\{\mathbf{B}, \mathbf{D}\}$ are replaced by the fault distribution matrices, $\{\mathbf{R}_1, \mathbf{R}_2\}$.

Substituting Equation 6.12 into Equation 6.9, the equation for the residual signal becomes

$$r(k) = \mathbf{p}^T \mathbf{Z} \mathbf{X}(k) + \mathbf{p}^T \mathbf{M} \mathbf{F}(k)$$

where

$$\mathbf{Z} = [\mathbf{W}\mathbf{L}] \tag{6.15}$$

$$\mathbf{X}(k) = \begin{bmatrix} \mathbf{x}(k-s) \\ \mathbf{N}(k) \end{bmatrix} \tag{6.16}$$

Subsequently, two performance indices can be defined as follows:

$$J_1 = \left\| \mathbf{p}^T \mathbf{Z} \right\|_2 \tag{6.17}$$

$$\hat{J}_2 = \left\| \mathbf{p}^T \mathbf{M} \right\|_2 \tag{6.18}$$

where $\|.\|_2$ denotes L_2 norm. Maximising $\hat{J}_2$ is equivalent to minimising

$$J_2 = -\left\|\mathbf{p}^T\mathbf{M}\right\|_2 \tag{6.19}$$

Finally, by minimising J_1 and J_2, the residual can become sensitive to faults but insensitive to disturbances and modelling errors, which is the desired property of the residuals for FDD. A multi-objective optimisation technique for minimising both performance indices at the same time is presented in the following section.

If enough information is given to determine $\Delta\mathbf{A}$, $\Delta\mathbf{B}$, and $\mathbf{E}$ in Equation 6.11, these matrices can be incorporated into Equation 6.10. If these matrices could be determined perfectly, the residual, $r(k)$ would be nearly zero where no fault is present. However, these matrices are often difficult to approximate in real life and thus assumed unknown in this chapter.

6.2 Multi-objective Optimisation

A combination of the method of inequalities (Zakian, 1979; Zakian and Al-Naib, 1973), the moving-boundaries algorithm (Maciejowski, 1989), and a genetic algorithm is exploited for solving the multi-objective optimisation problem presented in Section 6.1.

6.2.1 Method of Inequalities

The method of inequalities transforms the problem of the minimisation or maximisation of the performance indices to the problem of the satisfaction of a set of inequalities, That is, the problem becomes searching for a parameter set that satisfies the following inequalities:

$$J_i(\mathbf{p}) \leq \epsilon_i \tag{6.20}$$

where ϵ_i $(i = 1, 2)$ is the bound on the performance index, $J_i(\mathbf{p})$ chosen by the designer.

If $J_1^*(\mathbf{p})$ and $J_2^*(\mathbf{p})$ are the minimum values that can be achieved, ϵ_i $(i = 1, 2)$ should be defined as

$$J_i^*(\mathbf{p}) \leq \epsilon_i \tag{6.21}$$

By restricting or relaxing the bound, ϵ_i, a different emphasis can be placed. If J_j is important, ϵ_j needs to be let near to J_j^*, and if J_j is less important, ϵ_j needs to be let far away from J_j^*.

6.2.2 Moving-boundaries Algorithm

In order to solve the design problem posed above, Zakian and Al-Naib (1973) suggest the use of the moving-boundaries algorithm. The performance indices are first normalised as

$$\phi_i(\mathbf{p}) = J_i(\mathbf{p})/\epsilon_i \tag{6.22}$$

In turn, the problem becomes satisfying

$$\phi_i(\mathbf{p}) \leq 1 \tag{6.23}$$

To solve Equation 6.23, let $\mathbf{P}_i$ be the parameter that satisfies i^{th} performance index

$$\mathbf{P}_i = \{\mathbf{p} : \phi_i(\mathbf{p}) \leq 1\} \tag{6.24}$$

and $\mathbf{P}$ be the parameter that satisfies both performance indices

$$\mathbf{P} = \left\{\mathbf{p} : \max_{i=1}^{2} \{\phi_i(\mathbf{p}) \leq 1\}\right\} \tag{6.25}$$

The search for an optimal $\mathbf{P}$ can be achieved by solving the following optimisation problem:

$$\min \left\{\max_{i=1}^{2} \{\phi_i(\mathbf{p})\}\right\} \leq 1 \tag{6.26}$$

In order to solve Equation 6.26, let $\mathbf{P}^k$ be the parameter at step k, and define

$$\mathbf{P}_i^k = \left\{\mathbf{p} : \phi_i(\mathbf{p}) \leq \Delta^k\right\} \tag{6.27}$$

where

$$\Delta^k = \max_{i=1}^{2} \left\{\phi_i(\mathbf{p}^k)\right\} \tag{6.28}$$

Now, let the problem be to find a new parameter, $\mathbf{p}$ that reduces the largest performance index, Δ^k such that

$$\Delta^{k+1} \leq \Delta^k \tag{6.29}$$

The optimisation process terminates either when Δ^k is less than 1 or when Δ^k cannot be reduced further. If Δ^k cannot be reduced further and persists being larger than 1, the appropriate bound (ϵ_i) needs to be relaxed.

The difficult part of this process is the provision of a trial parameter, $\mathbf{P}^{k+1}$ given $\mathbf{P}^k$. As a solution, a genetic algorithm can be utilised as follows.

6.2.3 Multi-objective Optimisation via Genetic Algorithm

This chapter assumes that the readers are familiar with genetic algorithms – a brief introduction to a genetic algorithm including the terminology can be found in Appendix C.

The multi-objective optimisation procedures that utilise the combination of the method of inequalities, the moving-boundaries algorithm, and a genetic algorithm for satisfying the performance indices are summarised here.

Step 1: Determination of Bounds

The bound, ϵ_i $(i = 1, 2)$ in Equation 6.20 is chosen.

Step 2: Generation of Initial Population

A random matrix, whose numbers of columns and rows respectively represent the number of variables in the fitness function (i.e., the length of $\mathbf{p}$ in Equation 6.9) and the size of population, is generated.

Step 3: Evaluation

J_1 and J_2 in Equations 6.17 and 6.19 are calculated using each row of the matrix from *Step 2* (i.e., individual) as the variables. Using the bounds from *Step 1* and Equations 6.22 to 6.26, Δ^k in Equation 6.28 is calculated. This value, which is referred to as a "score", is used in the next step.

Step 4: Reproduction, Elitism, Recombination, and Mutation

This is where the multi-objective optimisation algorithm takes advantage of the genetic algorithm summarised in Appendix C. Tuning of the genetic algorithm is summarised in the following subsection.

Step 5: Termination Checking

Steps 3 and *4* are repeated until either the following criteria is met

$$\Delta^k \leq 1 \tag{6.30}$$

or until it cannot be minimised further, in which case, either ϵ_1 or ϵ_2 needs to be relaxed.

6.2.4 Tuning of the Genetic Algorithm

In order to execute the genetic algorithm, the Genetic Algorithm and Direct Search Toolbox™2 in Matlab® can be utilised. For all the simulations illustrated in Sections 6.3 and 6.4, the tuning parameters are set as follows:

- Population size: 20
- Number of generations: 100
- Reproduction method: ranking
- Elite count: 2 out of 20
- Cross-over fraction: 14 out of 20
- Cross-over function: scattering
- Mutation function: Gaussian distribution
- Mutation Fraction: 4 out of 20

6.3 Fault Detection

Having minimised both performance indices, J_1 and J_2 in Equations 6.17 and 6.19 at the same time using the multi-objective optimisation technique summarised in Section 6.2, the resulting FD system should produce a residual sensitive to faults but insensitive to disturbances. To assess the performance of this FD system, it has been applied to the first-principles model (Chapters 3 and 4) which has been used to simulate the plant throughout this thesis. Three of the simulations which have been conducted are summarised as follows. It is assumed that only one fault or disturbance can occur at any time.

- *Sensor fault*: The sensor measurements are perturbed by ±15% from 2000s
- *Disturbance 1*: Mass flow rate of polymer flowing into the die (Section 3.4) is perturbed by ±10% from 2000s
- *Disturbance 2*: Fast-nip roll speed (Section 3.6) is perturbed by ±10% from 2000s

Distinguishing faults from disturbances can be difficult. For instance, the above two disturbances can be regarded as either process faults or disturbances. In this chapter, anything that can be rejected by the controller (Chapter 5) eventually is

defined as a disturbance and anything else is defined as a fault. Also, recall that the number of lanes used for the model is 10 (Section 4.1.1).

$\mathbf{R}_1$ and $\mathbf{R}_2$ in Equation 6.10 have been set to $\mathbf{0}$ (zero matrix) and $\mathbf{I}_N$, respectively, because the residual needs to be sensitive to the sensor fault. The determination of these fault distribution matrices is revisited in the following section.

Figure 6.2 depicts the results for all these scenarios with one figure for comparison purposes. The upper and lower plots are the same but have different y-axes. The results show that the residual is sensitive to the fault but insensitive to both disturbances, which is the desired property of a FD system. Although, this FD system is capable of detecting faults successfully, fault diagnosis has not been addressed yet. A FDD system conducts fault diagnosis after fault detection and is presented in the following section.

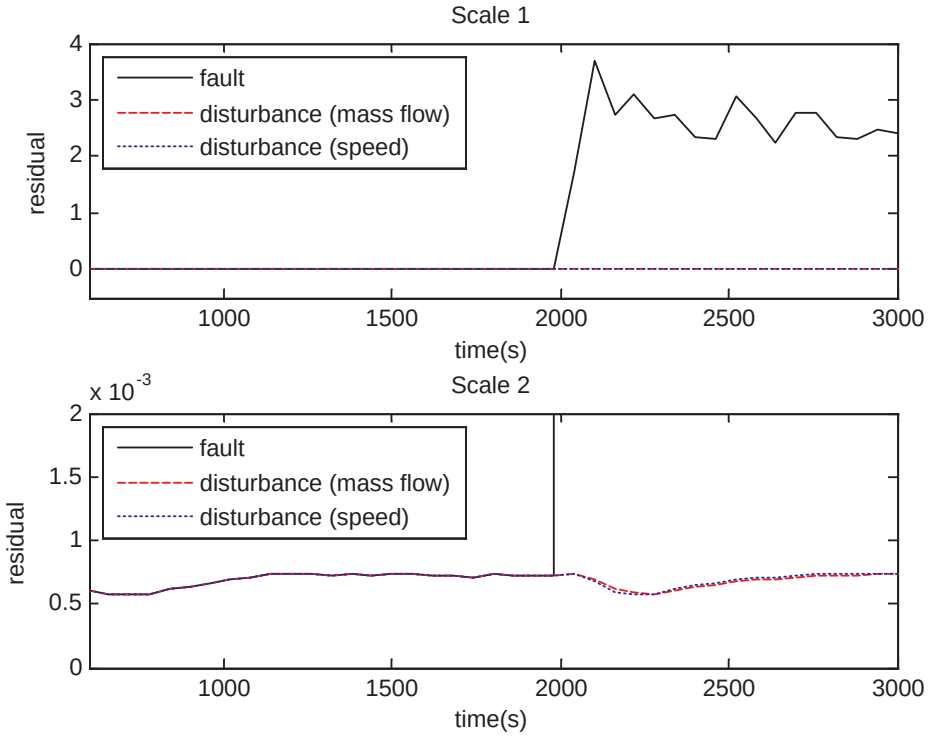

FIGURE 6.2: Upper plot: residual when fault occurs at 2000s (solid); Residual when mass flow rate is perturbed at 2000s (dashed); Residual when fast-nip roll speed is perturbed at 2000s (dotted), Lower plot: same as the upper plot with a different scale

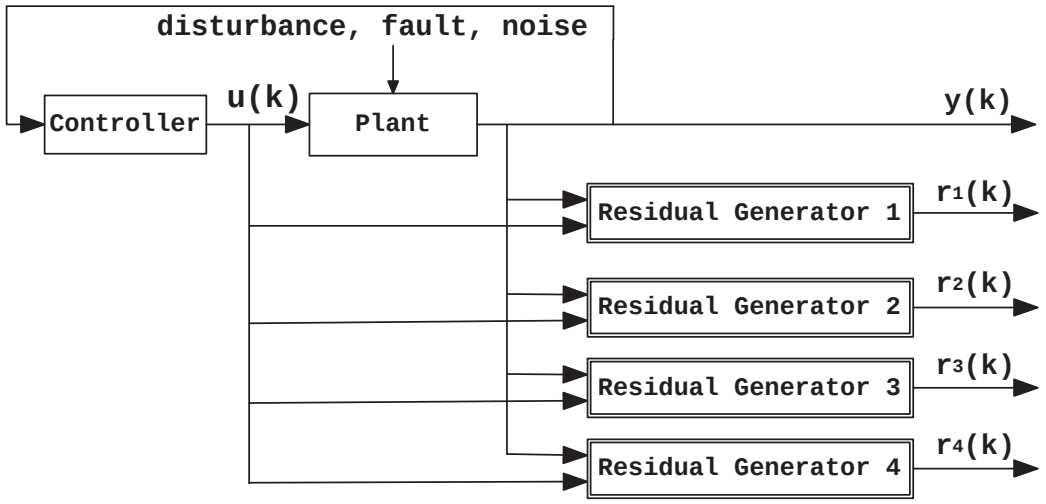

FIGURE 6.3: FDD via multiple residual generators

6.4 Fault Detection and Diagnosis

The development of a FDD system is presented in this section. This FDD system is the same as the FD system demonstrated in Section 6.3 but has more than one residual generator, each sensitive to one specific fault, as shown in Figure 6.3. Moreover, to make the scenarios more realistic, the mass flow rate of polymer flowing into the die is perturbed by $\pm 10\%$ at all times – this is regarded as a disturbance, which the FDD system requires to be insensitive to. Although this disturbance is persistent, it is assumed that only one fault can occur at any time

- *Sensor fault*: The sensor measurements are perturbed by $\pm 15\%$ from 1500s
- *Actuator fault 1*: The third die bolt becomes stuck from 1500s
- *Actuator fault 2*: The fifth die bolt becomes stuck from 1500s
- *Actuator fault 3*: The eighth die bolt becomes stuck from 1500s

If each residual generator can be made to be sensitive to one fault only, the faults can be diagnosed adequately. For each residual generator to produce a residual sensitive to a specific fault, each residual generator requires to have specific fault distribution matrices, $\mathbf{R}_1$ and $\mathbf{R}_2$ in Equation 6.10. Consequently, each residual

generator has a different $\mathbf{Z}$ and $\mathbf{M}$ in Equations 6.17 and 6.19, and $\mathbf{p}$ is thus unique for each residual generator.

The most difficult part of FDD can be the approximation of the fault distribution matrices. If these matrices could be determined 100% accurately, it would be possible to seperate faults from disturbances completely. As a result, the performance of the FDD system would be nearly perfect, but this is not feasible. Nevertheless, many books and papers assume that these matrices are known in advance because they usually employ an empirical model and faults often need to be modelled to be incorporated into the model to simulate faulty conditions. In contrast, the first-principles model developed in Chapters 3 and 4 has a feature that allows the injection of faults and disturbances similarly to the real-life process without having to develop fault models.

In this section, like a real-life situation, the fault distribution matrices cannot be given but need to be approximated for the particular FDD problem shown above as follows.

For the first residual generator in Figure 6.3 to be sensitive to the sensor fault, $\mathbf{R}_1$ and $\mathbf{R}_2$ can be approximated as

$$\begin{aligned} \mathbf{R}_1 &= \mathbf{0} \\ \mathbf{R}_2 &= \mathbf{I}_N \end{aligned} \tag{6.31}$$

This intuitive approximation is inspired by the fact that sensor faults tend to affect the output equation without affecting the states.

The three residual generators are constructed to be sensitive to the fault on a specific actuator. This is to demonstrate that the FDD system can be designed for a specific actuator among a few hundred actuators, thereby indicating which specific actuator has become faulty. However, since the sensing system employed by the first-principles model is a scanning gauge rather than an array of sensors (Section 2.8), only one residual generator is constructed for the sensor fault.

For the residual generator to be sensitive to an actuator fault, $\mathbf{R}_1$ and $\mathbf{R}_2$ can be approximated as

$$\begin{aligned} \mathbf{R}_1 &= \mathbf{B} \\ \mathbf{R}_2 &= \mathbf{D} \end{aligned} \tag{6.32}$$

where $\mathbf{D}$ is assumed to be a zero matrix in this chapter. This approximation is inspired by the fact that the actuator faults affect the input signal, $\mathbf{u}(k)$ directly, such that Equation 6.10 becomes

$$\begin{aligned} \mathbf{x}(k+1) &= \mathbf{A}\mathbf{x}(k) + \mathbf{B}(\mathbf{u}(k) + \mathbf{f}(k)) + \mathbf{d}(k) \\ \mathbf{y}(k) &= \mathbf{C}\mathbf{x}(k) + \mathbf{D}(\mathbf{u}(k) + \mathbf{f}(k)) \end{aligned} \tag{6.33}$$

For the residual generator to be sensitive to i^{th} actuator fault, every entry of the matrix, $\mathbf{R}_1$ in Equation 6.32 can be set to zero except i^{th} column – i^{th} column of $\mathbf{R}_1$ remains the same as i^{th} column of $\mathbf{B}$. In this manner, the remaining three residual generators can be constructed to be sensitive to the 3^{rd}, 5^{th}, and 8^{th} actuator faults – 3, 5, and 8 have been chosen randomly to demonstrate that a residual generator can be designed for a specific actuator among as many as a few hundreds to indicate which actuator is faulty.

The results are depicted in Figures 6.4, 6.5, 6.6, and 6.7. The thresholds are manually set to 1 for the first residual generator and 50 for the rest. If any of these thresholds is violated, a fault is detected. A fault can then be diagnosed by checking which threshold has been violated. The results successfully demonstrate that every residual generator is sensitive to a specific fault and insensitive to the disturbance.

Although only four residual generators are constructed here, the number of residual generators will be considerably higher in real life depending on the number of faults required to detect and diagnose. From the experience, the plant operators would know the types of faults which need to be detected and diagnosed. Using this information, the number and types of the residual generators can be determined appropriately.

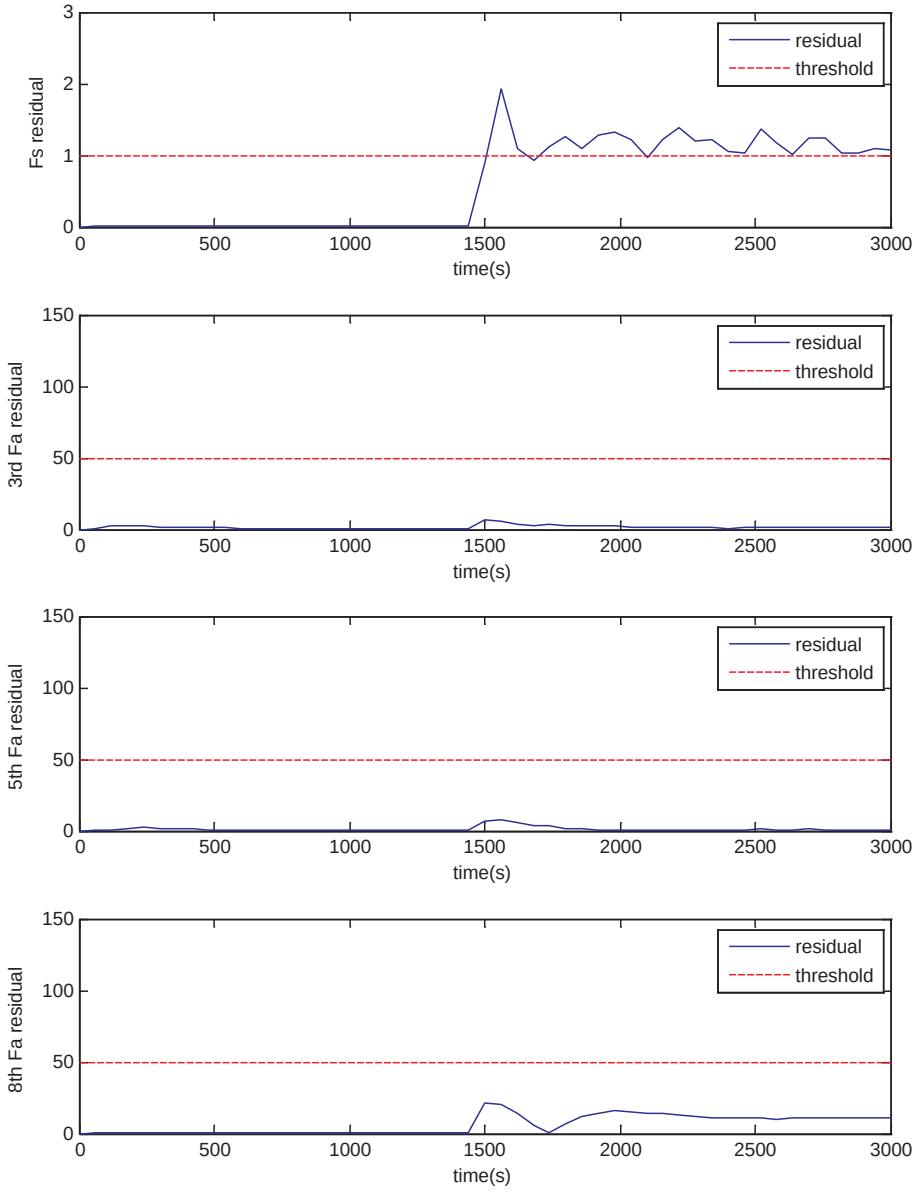

FIGURE 6.4: Residuals when sensor fault occurs at 1500s

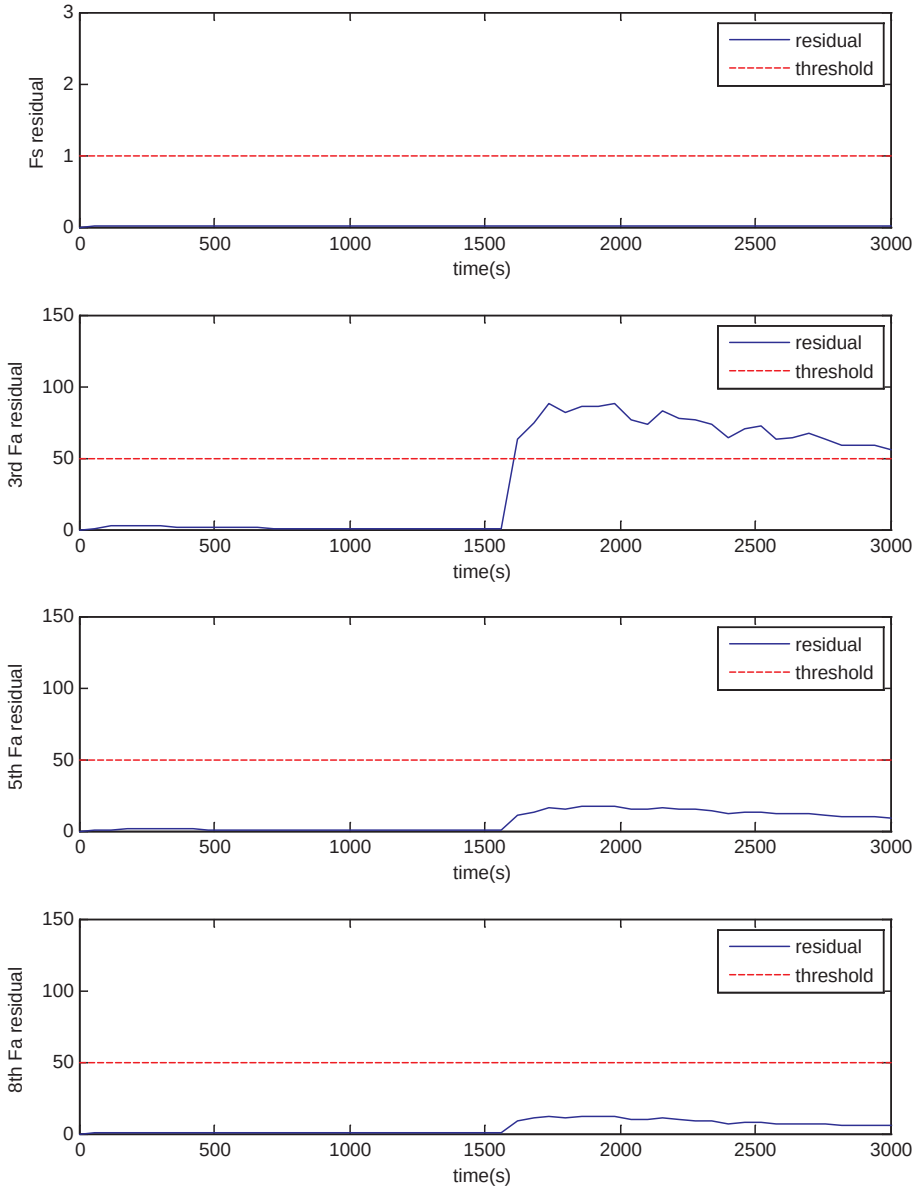

FIGURE 6.5: Residuals when 3^{rd} die bolt becomes stuck at 1500s

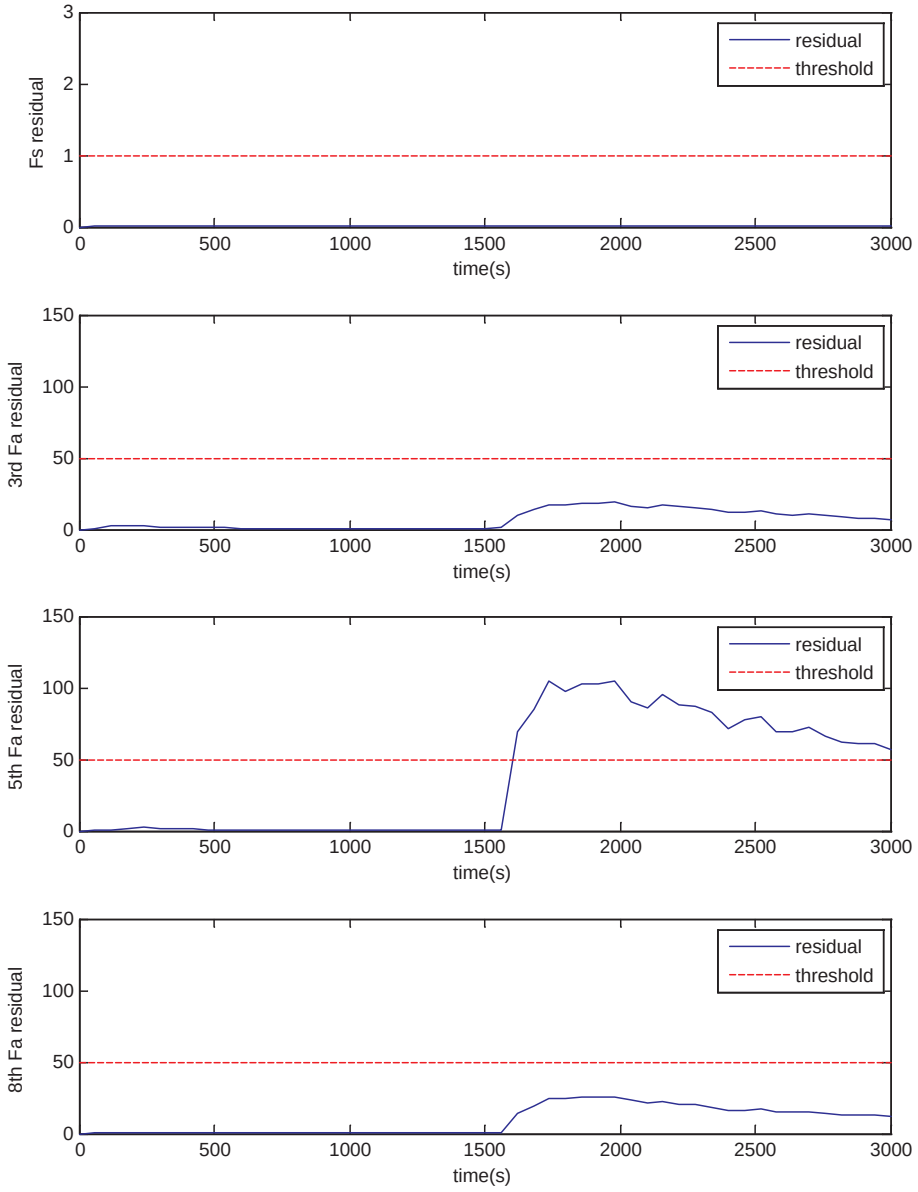

FIGURE 6.6: Residuals when 5^{th} die bolt becomes stuck at 1500s

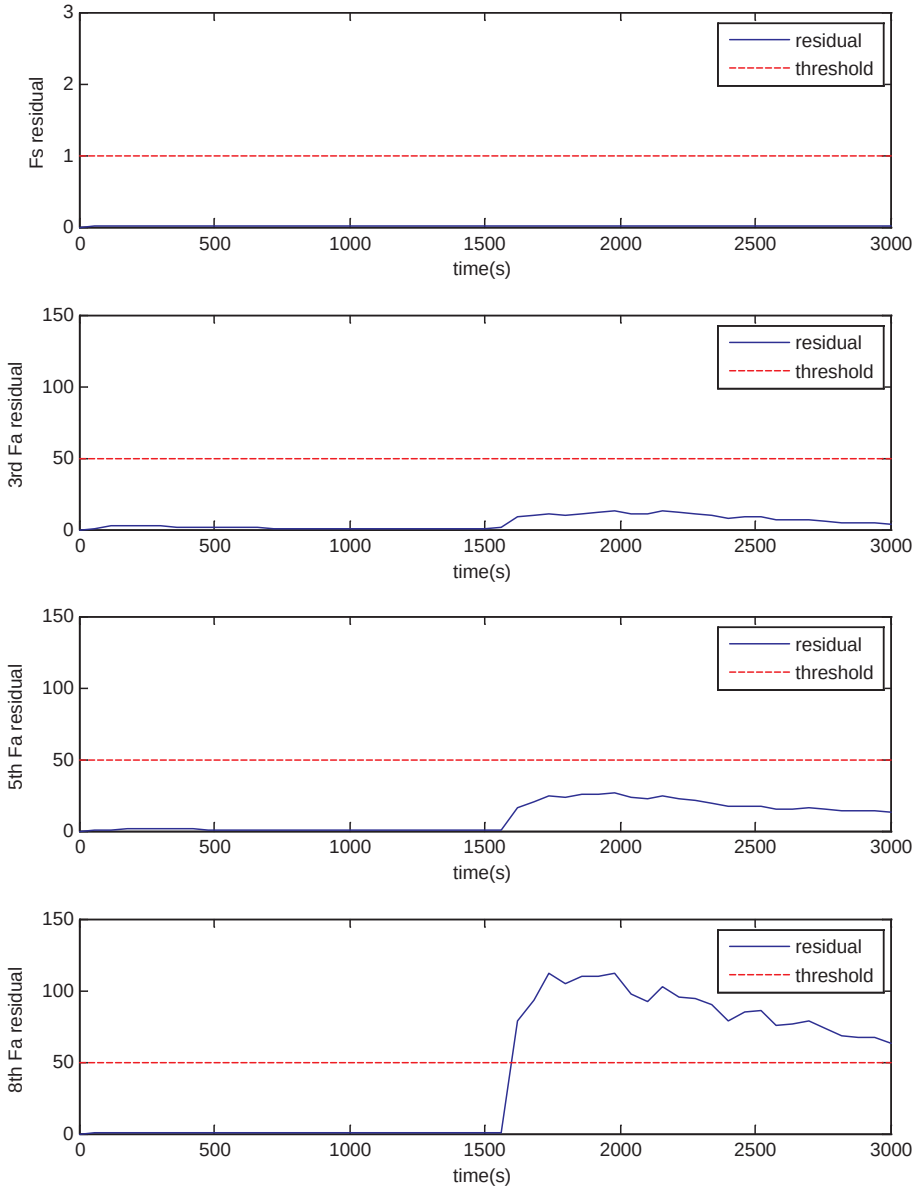

FIGURE 6.7: Residuals when 8^{th} die bolt becomes stuck at 1500s

6.5 Fault Detection and Diagnosis: Application to Real-life Measurement

In order to find out how the FDD system would perform in real life, real-life data containing the actuator set-points and measurements of CD thickness profile have been provided (DTF, 2009). The original data contained 49 set-points and 245 measurements at each time instant since there are 49 die bolt heaters and the film is divided into 245 lanes for controlling purposes in real life. However, both

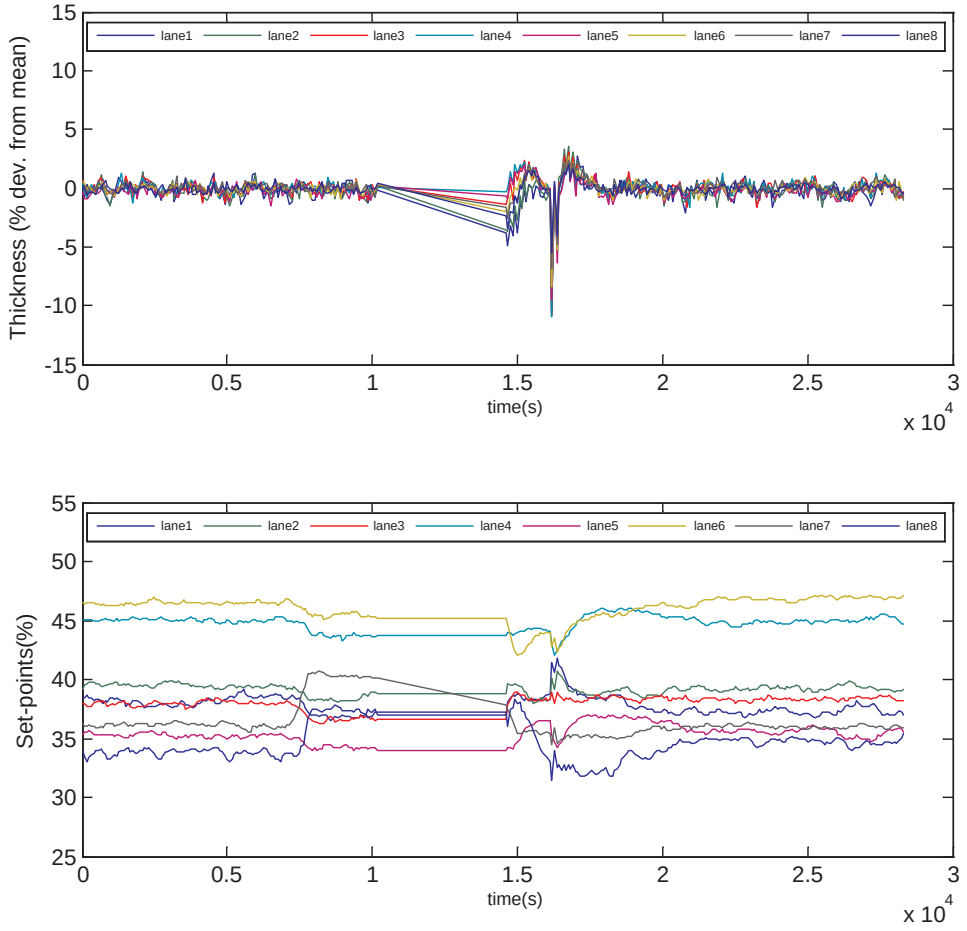

FIGURE 6.8: Industrial data; 8^{th} die bolt becomes stuck at $t \approx 7300s$ and recovery period affects the measurements at $t \approx 16000s$, Upper plot: measurements; Lower plot: set-points

are reduced to 10 since it is assumed in this thesis that the numbers of die bolt heaters and lanes are both 10 (Section 4.1.1). Furthermore, the edges are removed to mimic what happens in real life and therefore Figure 6.8 depicts 8 lanes (Section 4.2.2).

A die bolt failed at approximately 7300s, and the operators picked up the failure within a few minutes and placed the the die bolt heaters into manual to compensate before the bolt was replaced at approximately 15000s – notice a gap in the time between the scans from approximately 10000s to 15000s while the bolt was being replaced. That is, the figure depicts the set-points and measurements during normal operation before the fault, fault onset, faulty situation as dealt with by the operators, and recovery following the repair.

The FDD system presented in Section 6.4 is applied to this data, and the results are shown in Figure 6.9. Similarly to the results shown in Section 6.4, the thresholds are manually set to 5000. If any of these thresholds is violated, a fault is detected. A fault can in turn be diagnosed by confirming which threshold has been violated.

Due to the excellent work performed by the operators and their own sophisticated FDD system, the fault was detected almost immediately after the onset and the die bolt heaters were put into manual. Consequently, the fault, which appeared at approximately 7300s hardly affected the measurements as shown in Figure 6.8. For the purpose of assessing the FDD system, it would have been better if the fault was not detected as quickly but then obtaining such a data would not be easy. Nevertheless, when the operators replaced the failed die bolt, which was the 8^{th} one, the transient (or recovery) period affected the measurements at approximately 16000s as shown in Figure 6.8. This is picked up by the FDD system presented in the previous section as shown in Figure 6.9. Notice that only the residual dedicated to the 8^{th} actuator fault violates the threshold, indicating that there is a problem with the 8^{th} die bolt heater.

In conclusion, if the operators had failed to detect the fault letting it affect the measurements, the FDD system would have detected and diagnosed the fault that appeared at approximately 7300s. This is to some degree backed up by the results shown in Figure 6.9 since the recovery (of 8^{th} die bolt heater) that affected the

measurements is detected and diagnosed correctly by the FDD system introduced in this chapter.

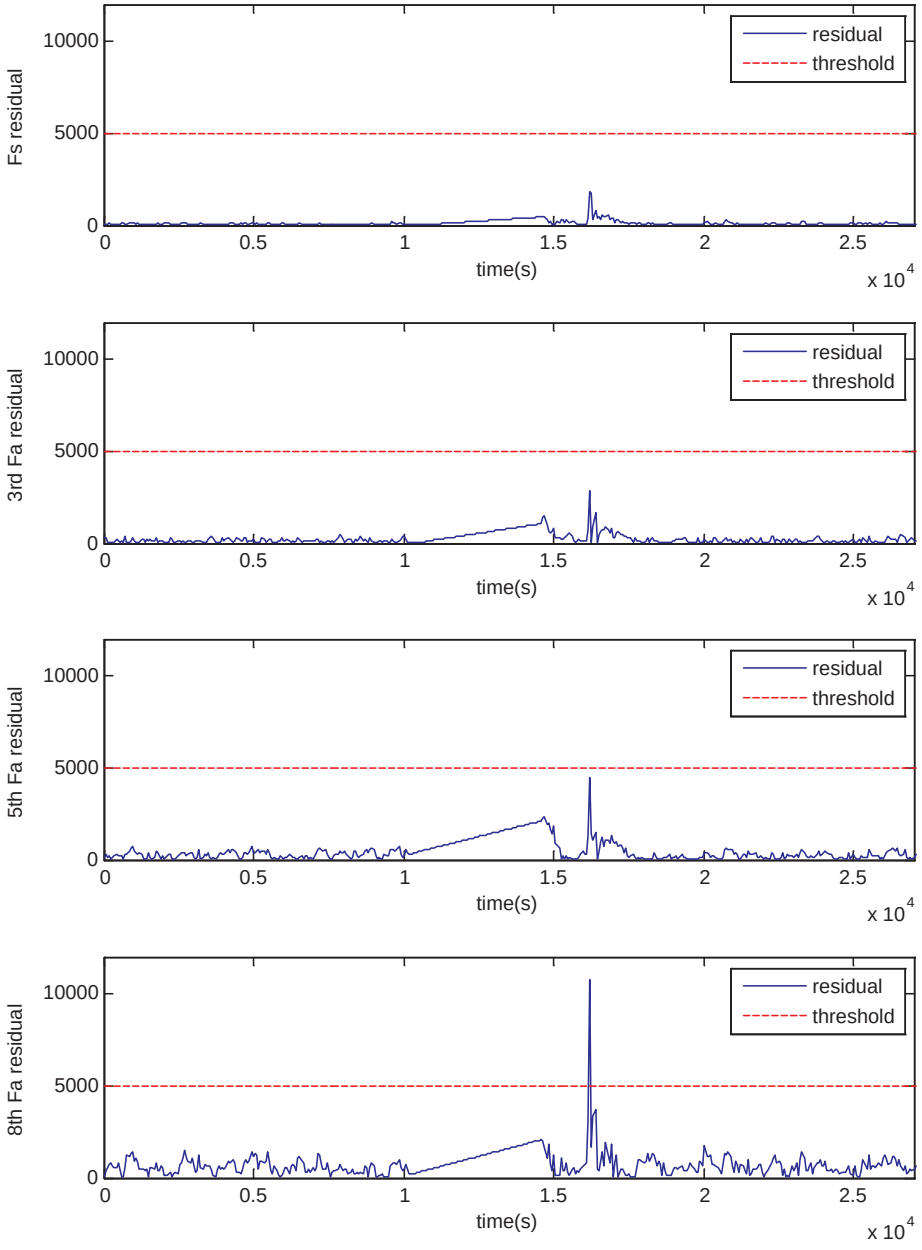

FIGURE 6.9: Industrial data; Residuals when 8^{th} die bolt becomes stuck at $t \approx 7300s$; Recovery period affects the measurements at $t \approx 16000s$

6.6 Summary

This chapter has reported the design of a FDD system. This system is based on the parity relations and thus requires solving a multi-objective optimisation problem. A genetic algorithm, which is an evolutionary algorithm, is utilised for solving this multi-objective optimisation problem.

This is a novel approach as an analytical method is usually utilised for solving this multi-objective optimisation problem. For residual generation, the parity relation approach is used rather than other popular methods such as the observer approach for several reasons. The plant observation for a plastic film manufacturing process is the CD thickness profile, which needs to be divided into many sections for controlling and monitoring purposes. When the observer approach is employed for residual generation, the number of the residual signals equals the number of the CD sections, and the determination of the thresholds can thus be difficult or the use of a dimensionality reduction technique is necessary. However, by using the parity relations for residual generation, all the residual signals are arranged under one signal without having to employ a dimensionality reduction technique. This makes parity relations more suitable for other sheet-forming processes, too.

Also, optimising an observer based residual generator requires the conversion of the performance indices into the frequency domain for the multi-objective optimisation. Since the conversion needs to be performed at every iteration during the multi-objective optimisation, the computation time required for the optimisation can be significant. Moreover, the observer approach requires an extra algorithm to guarantee the stability condition unlike the parity relation approach.

The simulation results in Section 6.3 demonstrates that the FD system is sensitive to faults but insensitive to disturbances at the same time, which is the desired fault detection property. Many papers and books focus more on fault detection, and fault diagnosis is often neglected. Even when they do, the fault distribution matrices are often known to the authors in advance. Section 6.4, on the other hand, focuses on fault diagnosis and the fault distribution matrices are not given but need to be determined for the particular FDD problem addressed in the section. It is highlighted in the section that the determination of the fault distribution matrices can play a very important role in FDD. The simulation results in the section show that fault diagnosis can be conducted successfully.

The system is also applied to data extracted from the industrial process, and the results demonstrate its suitability in real life in Section 6.5. The design can be used for other kinds of processes, such as papermaking and steel-rolling as long as a reference model can be identified in the state space form.

Chapter 7

Conclusions and Future Work

7.1 Conclusions

The main topics covered in this thesis can be summarised as

- Review of the plastic film manufacturing process
- First-principles modelling of the process
- Model Implementation and validation
- Cross-directional (CD) control
- Fault detection and diagnosis (FDD)

Chapter 2 described the process step by step with plenty of figures for clear presentation. The process described in Chapter 2 was subsequently modelled in Chapter 3. First-principles models of plastic film manufacturing processes are still rare as these models are regarded as difficult and time-consuming to build. Nevertheless, the model introduced in the chapter was mainly based on the first-principles, taking account of the characteristics of the unit operations of the process in addition to empirical knowledge related to the behaviour of polymer. The model can be utilised in many ways, but this thesis demonstrated four applications as follows:

1. The model simulated the real-life process to demonstrate various operational scenarios in Chapters 4, 5, and 6. This can be useful for tuning the process as well as for training the plant operators.

2. The model simulated the real-life process to allow control algorithms to be developed and tested without wasting product in Chapter 5.

3. By adding disturbances and faults, realistic scenarios where faults and disturbances are present were simulated which allowed control and fault monitoring algorithms to be developed safely in Chapters and 5 and 6.

4. A state space model required for both the control and fault monitoring algorithms was identified from the model without the need for experiments on the real-life process in Appendix B.

The model was implemented in Matlab/Simulink®, its parameters were tuned, and validation experiments were carried out in Chapter 4. The die response model that is employed to simulate the plant in real life was utilised for the parameter tuning of the first-principles model. The results in turn demonstrated that the die response of the first-principles model was close to that of the die response model. Besides the validation experiments, a number of step tests were performed and then the results were validated against real-world process understanding to compensate for the limited data available for the validation.

The development of a new model-based CD controller design and its application to the first-principles model were reported in Chapter 5. The controller was based on IMC but also included an observer whose gain was designed to minimise the effects of model-plant mismatch and disturbances. Moreover, the optimal steady state performance was encouraged and actuator saturation was discouraged by introducing a new objective function that needed to be optimised online subject to constraints. Simulation results, which provided comparison between the proposed controller and other existing controllers under different disturbance scenarios demonstrated improvements that the proposed controller could achieve.

A fault detection and diagnosis (FDD) system was introduced in Chapter 6. This FDD system was based on the parity relations and thus required solving a multi-objective optimisation problem. A genetic algorithm (Appendix C), which is an

evolutionary algorithm, was utilised for solving this multi-objective optimisation problem. Many books and papers focus on fault detection, and fault diagnosis is often neglected. Nonetheless, the chapter addressed a fault diagnosis problem and showed that the approximation of the fault distribution matrices could play a very important role in fault diagnosis. The determination of these matrices is not straightforward, but some progress was made in the chapter. The subsequent simulation results demonstrated successful application of the FDD system not only to the first-principles model but also to data extracted from the real-life plant.

7.2 Future Work

7.2.1 Further Applications of the Model

Two most important properties that can be tracked throughout the model are thickness and temperature. Although Chapters 5 and 6 made extensive use of the thickness tracking property of the model, the temperature tracking property was only utilised by the sideways-draw model. Because the film temperature plays an important role in the plastic film manufacturing process, the temperature tracking property of the model would also be valuable for monitoring the temperature of the film at various locations. Further, the model could be utilised for determining the optimal design, position, and spacing of sensors and actuators as discussed in VanAntwerp et al. (2007).

7.2.2 Further Validation and Parameter Tuning of the Model

Due to the limited number of sensors available online, the validation of the model was restricted as discussed in Chapter 4. This was compensated to some degree by performing step tests at various locations of the model, which were then validated against real-world process understanding. The acquisition of more data,

especially properties rather than thickness, such as temperature, and the properties at other locations rather than where the gauging sensor is located would allow more versatile validation and parameter tuning experiments.

7.2.3 More Real-life Process Data

A set of real-life data containing the actuator set-points and sensor measurements under a faulty condition were given, and the FDD system introduced in Chapter 6 was applied to this data set in order to assess the FDD system. More sets under different kinds of faulty conditions would allow further assessment of the FDD system although its performance was also tested by application to the first-principles model. Furthermore, in the data set, a fault occurred but was detected and compensated for by the plant operators quickly, thereby not affecting the output. If a data set containing a fault which could not be detected by the plant operators quickly enough would be more valuable for the purpose of testing the FDD system.

7.2.4 Determination of Disturbance and Fault Distribution Matrices

The controller proposed in Chapter 5 approximated the disturbance distribution matrices, and the FDD system introduced in Chapter 6 approximated the disturbance distribution matrices over and above the fault distribution matrices. With such approximations, the simulation results in Chapter 5 demonstrated improvements that the proposed controller could achieve and those in Chapter 6 showed that faults could be detected and diagnosed successfully. Nonetheless, if better approximation of the disturbance distribution matrices can be acquired, the performance of the controller can improve further and, similarly, better approximation of the disturbance and fault distribution matrices can improve the performance of the FDD system.

Appendix A

Parameters of the First-principles Model

Symbols	Parameters	Units
k_r	conductivity of metal (roll)	W/Km
k_p	conductivity of polymer	W/Km
ρ	density of polymer	kg/m^3
	geometry of casting drums, *see Figure* 3.8	m
	geometry of die, *see Figure* 3.6	m
	geometry of slow-nip rolls to coaters	m
	geometry of stenter oven	m
h_{isp}^{bf}	heat transfer coefficient from air to polymer, buffer stage (stenter)	W/m^2K
h_{isp}^{c}	heat transfer coefficient from air to polymer, cooling stage (stenter)	W/m^2K
h_{isp}^{cr}	heat transfer coefficient from air to polymer, crystallisation stage (stenter)	W/m^2K
h_{isp}^{etc}	heat transfer coefficient from air to polymer, outside stenter	W/m^2K
h_{isp}^{st}	heat transfer coefficient from air to polymer, pre-heat stage (stenter)	W/m^2K
h_{isp}^{sd}	heat transfer coefficient from air to	W/m^2K

Symbols	Parameters	Units
	polymer, sideways-draw stage (stenter)	
h_{iwr}^{cd}	heat transfer coefficient from water to roll, casting drum	W/m^2K
h_{iwr}^{qr}	heat transfer coefficient from water to roll, quench roll	W/m^2K
h_{iwr}^{etc}	heat transfer coefficient from water to roll, rest rolls	W/m^2K
h_{iwr}^{to}	heat transfer coefficient from water to roll, take-off roll	W/m^2K
h_{irp}^{cd}	heat transfer coefficient from roll to polymer, casting drum	W/m^2K
h_{irp}^{qr}	heat transfer coefficient from roll to polymer, quench roll	W/m^2K
h_{irp}^{etc}	heat transfer coefficient from roll to polymer, rest rolls	W/m^2K
h_{irp}^{to}	heat transfer coefficient from roll to polymer, take-off roll	W/m^2K
ξ	mass flow correction factor	
M_c^f	mass fraction crystalline for finished film	%
M_c^{fd}	mass fraction crystalline for forward drawn film	%
M_c^m	mass fraction crystalline for melt	%
M_c^{sd}	mass fraction crystalline for sideways drawn film	%
η_{cast}	neck-in correction factor (casting)	
η_{fd}	neck-in correction factor (forward-draw)	
N	number of lanes	
α, β, and χ	parameters in Equation 3.14	
κ and ψ	parameters in Equation 3.52	
k_g	process gain in Equation 4.5	
Δx	step size for mass and heat transfer modules	
Λ_{fd}	stretch ratio (forward-draw)	
Λ_{sd}	stretch ratio (sideways-draw)	

Symbols	**Parameters**	**Units**
T_s^{cd}	temperature of air surrounding casting drum	K
T_s^{c}	temperature of air surrounding cooling rolls	K
T_s^{ph}	temperature of air surrounding pre-heat rolls	K
T_s^{bf}	temperature at buffer stage (stenter oven)	K
T_s^{cl}	temperature at cooling stage (stenter oven)	K
T_s^{cr}	temperature at crystallisation stage (stenter oven)	K
T_{ph}^{sd}	temperature at pre-heat stage (stenter oven)	K
T_s^{sd}	temperature at sideways-draw	K
T_w^{cd}	temperature of water inside casting drum	K
T_w^{c}	temperature of water inside cooling rolls	K
T_w^{ph}	temperature of water inside pre-heat rolls	K
μ	viscosity of polymer	$bar \cdot s$
$\tilde{w}$	width of sideways-drawn film	m
w	width of un-stretched film	m

Appendix B

System Identification

Both the controller design in Chapter 5 and the fault monitoring algorithm in Chapter 6 need a state space model. Using the System Identification Toolbox™7 in Matlab®, a state space model can be identified from the first-principles model developed in Chapters 3 and 4. This appendix begins with summarising the system identification procedures followed by a summary of the resulting state space model. Then, the model is validated by calculating the accuracy of the model relative to the first-principles model and also by comparing the open-loop responses of the state-space model with those of the first-principles model.

B.1 Identification Procedures

1. 'N' pseudo random binary signals (PRBS) are generated using "idinput" function, where N denotes the number of die bolt heaters assumed for the first-principles model (Section 4.1.1). The range (upper and lower bounds) of the signal determined at this stage represents the operating range, outside which the state space model may not be valid if the system is highly non-linear. As the range increases, the accuracy of the model may reduce or vice versa.
2. The PRBSs are exported to Simulink® using "iddata" function.
3. The PRBSs are fed into the first-principles model, and the CD thickness profile and the PRBSs are saved as the output and input, respectively.

4. From a subset of the input and output, a state space model is estimated using "n4sid" function, which uses subspace method.

B.2 Summary of the Model

The resulting model is a standard state space model as follows:

$$\begin{aligned} \dot{\mathbf{x}}(t) &= \mathbf{A}\mathbf{x}(t) + \mathbf{B}\mathbf{u}(t) \\ \mathbf{y}(t) &= \mathbf{C}\mathbf{x}(t) \end{aligned} \tag{B.1}$$

where $\mathbf{x}(t) \in \mathbb{R}^R$ denotes the states (R=14), and the input, $\mathbf{u}(t) \in \mathbb{R}^N$ and output, $\mathbf{y}(t) \in \mathbb{R}^M$ respectively represent the actuator set-points and CD thickness profile of the final product. In this thesis, N is 8 since it is assumed that the film is divided into 10 lanes for controlling purposes and then the edges – first and last lanes – are removed (Section 4.1.1). Further, it is assumed that there is one actuator per each CD section (lane), hence M being also 8. **A**, **B**, and **C** are given as follows:

$$\mathbf{A} = 10^{-3}\times \begin{bmatrix} 60.7 & -3.8 & 5.1 & -10.5 & 4.9 & -0.7 & 4.8 & 5.7 & 26.1 & -7.3 & -57.9 & 14.2 & 48.8 & 24.3 \\ -4.1 & 72.1 & 4.0 & 17.1 & -52.1 & -18.5 & 4.1 & -15.7 & 27.5 & -74.5 & -9.4 & 1.2 & 5.0 & -39.3 \\ 0.1 & 4.8 & 56.8 & 9.7 & -35.7 & -10.4 & 2.7 & -16.3 & -42.3 & -32.1 & -28.4 & -43.6 & -29.7 & 34.5 \\ 1.8 & -6.5 & 8.5 & 49.7 & 11.3 & 2.1 & 9.2 & 12.9 & -49.7 & 29.0 & -28.3 & -22.2 & 27.5 & -56.3 \\ 0.2 & -1.9 & 3.0 & -10.0 & 54.8 & -2.7 & -11.2 & -37.9 & 2.8 & -0.0 & 1.9 & -23.5 & -5.1 & -30.9 \\ 5.0 & 8.2 & 4.8 & 2.0 & 8.3 & 50.2 & -0.0 & 1.9 & -39.6 & -32.1 & 43.4 & 3.9 & 59.1 & 18.1 \\ 9.3 & 2.3 & -5.5 & 0.1 & 34.5 & -1.5 & 58.4 & 38.6 & 38.4 & 0.4 & 12.2 & -74.3 & 21.2 & 23.6 \\ 368.9 & -274.2 & 112.4 & -533.9 & 1920.5 & 516.0 & -312.1 & 483.6 & -11.0 & 9.3 & -3.9 & 27.5 & -25.9 & -4.3 \\ -223.2 & -197.9 & 416.8 & 518.1 & -260.3 & 387.0 & -336.7 & 2.3 & 495.9 & -5.6 & -1.7 & -4.3 & -7.8 & 9.3 \\ -99.6 & 761.3 & 308.2 & -186.3 & -260.6 & 214.0 & 8.2 & 21.9 & -0.4 & 483.8 & -12.2 & 0.7 & -0.0 & -3.1 \\ 620.8 & 205.8 & 312.6 & 328.1 & -170.3 & -509.2 & -134.6 & 6.8 & -6.6 & -6.4 & 488.7 & 1.5 & 2.1 & 18.2 \\ -158.9 & -70.1 & 392.0 & 142.0 & 523.5 & 57.8 & 682.8 & -6.8 & 6.8 & 5.6 & -7.6 & 492.1 & -2.1 & -13.3 \\ -568.4 & 6.5 & 314.3 & -252.1 & -252.8 & -0.6883 & -0.1997 & 20.8 & -4.5 & 2.9 & 3.5 & 2.3 & 503.5 & -0.5 \\ -229.1 & 391.7 & -427.2 & 638.2 & 428.2 & -163.2 & -181.0 & 8.5 & -4.0 & -2.4 & 7.0 & -2.1 & -10.4 & 504.1 \end{bmatrix} \tag{B.2}$$

$$\mathbf{B} = 10^{-3}\times$$

$$\begin{bmatrix} 318.7 & -948.5 & 1566.7 & 339.5 & -1369.6 & 429.3 & 670.0 & 377.1 \\ -354.1 & -218.2 & -1105.5 & 1783.8 & -238.6 & 535.3 & 105.4 & -468.2 \\ 1281.5 & 92.1 & -73.7 & -857.4 & 14.0 & 1331.2 & -908.3 & -940.1 \\ 34.2 & -1735.6 & -225.4 & 300.9 & 1748.3 & -368.6 & -71.5 & 335.1 \\ 437.5 & -383.1 & -1562.6 & -692.2 & -577.8 & 813.4 & 0.3633 & 1.6344 \\ -1329.3 & -323.3 & 631.5 & -413.0 & 366.8 & 1645.9 & -0.5951 & 0.1199 \\ -238.5 & -657.8 & 120.9 & -992.1 & 83.9 & 581.5 & 2.0150 & -0.8386 \\ -1817.0 & 773.7 & -804.8 & 453.0 & 648.1 & 235.8 & 0.5968 & -0.1451 \\ 65.3 & -270.9 & -84.9 & -29.7 & -83.9 & 376.9 & 0.0261 & 0.0421 \\ 498.6 & -120.9 & -482.1 & 252.3 & 20.9 & -207.9 & 0.2299 & -0.1713 \\ 5.4 & 415.7 & 100.5 & -288.7 & 89.4 & -186.4 & -0.2362 & 0.1273 \\ -86.2 & 44.6 & -273.3 & 116.5 & -3.4 & -35.5 & 0.6404 & -0.4480 \\ -162.8 & 72.2 & 386.1 & 70.4 & 37.1 & -271.4 & -0.3747 & 0.2775 \\ -58.2 & -244.9 & 626.7 & -357.6 & -106.3 & -42.6 & -0.3728 & 0.3992 \end{bmatrix} \tag{B.3}$$

$$\mathbf{C} = 10^{-3}\times$$

$$\begin{bmatrix} -9.9 & -7.8 & -6.5 & -6.9 & -4.4 & 5.8 & -5.4 & -5.1 & -3.6 & 6.4 & -45.0 & -20.9 & -23.4 & 2.5 \\ -0.5 & 5.3 & -4.1 & 1.5 & -1.2 & 3.8 & -3.5 & -5.7 & -0.5 & -1.9 & 27.0 & 16.8 & -26.5 & 15.6 \\ 1.7 & 0.5 & 6.6 & -0.9 & 1.5 & -2.5 & 1.0 & 9.0 & 2.2 & 18.8 & -3.3 & 12.4 & 22.4 & 21.4 \\ 3.3 & -6.1 & 5.1 & 4.1 & 2.1 & -9.3 & -5.1 & 3.8 & 14.7 & -32.7 & -12.1 & 16.2 & 8.9 & -16.7 \\ 15.0 & -0.6 & 4.3 & 6.0 & 4.5 & -0.4 & 3.4 & 8.4 & -39.6 & 6.0 & 20.7 & -5.5 & -10.9 & -14.1 \\ -10.3 & 18.1 & 3.2 & -0.4 & 2.4 & -6.7 & 10.2 & -9.4 & -16.9 & -32.0 & 0.6 & -10.6 & 16.0 & 14.2 \\ 5.7 & -1.1 & 3.5 & 1.1 & -3.6 & -12.7 & 6.7 & 14.6 & 42.3 & 4.7 & 13.4 & -27.3 & 11.1 & -5.3 \\ -5.0 & -8.4 & -12.2 & -4.5 & -1.4 & 22.0 & -7.4 & -15.6 & 1.3 & 30.7 & -1.3 & 18.9 & 2.5 & -17.6 \end{bmatrix} \tag{B.4}$$

With these matrices, the observability matrix

$$\mathbf{P}_o = \begin{bmatrix} \mathbf{C} & \mathbf{CA} & \cdots & \mathbf{CA}^{n-1} \end{bmatrix}^T \tag{B.5}$$

has a full rank and the state space model is thus completely observable (Kokotovic et al., 1999; Li, 2001). This implies that a stable observer can be designed, which is a requirement for the proposed controller design presented in Chapter 5.

B.3 Model Accuracy

"compare" function compares the estimated model with another subset of the input and output for validation. Accuracy, ψ is determined by the following measure:

$$\psi_i = 100(1 - \frac{\|\hat{y}_i - y_i\|}{\|\bar{y}_i - y_i\|}) \tag{B.6}$$

for $i = 1, 2, \ldots, N$, where N represents the number of lanes used for the model and $\mathbf{y}$, $\hat{\mathbf{y}}$, and $\bar{\mathbf{y}}$ denote the output, output estimate, and output mean, respectively. $\|.\|$ represents L_2 norm, and ψ, which is in %, can be defined as the output deviation over the standard deviation.

ψ_i (for $i = 1, 2, \ldots, n$) is shown in Figure B.1, which illustrates that accuracy remains above 90% with 100% being the highest.

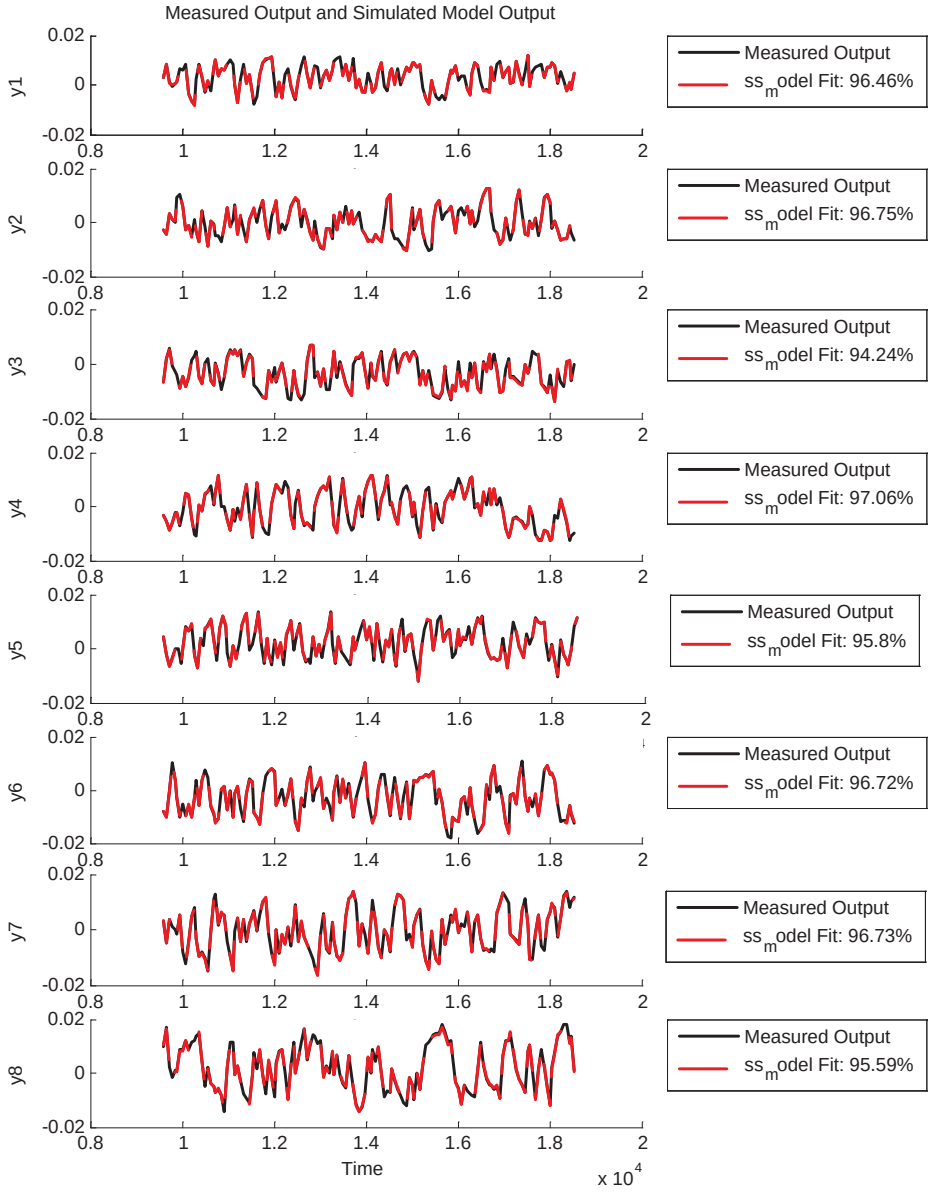

FIGURE B.1: Comparison between the outputs of first-principles model and the state space model

B.4 Open-loop Tests

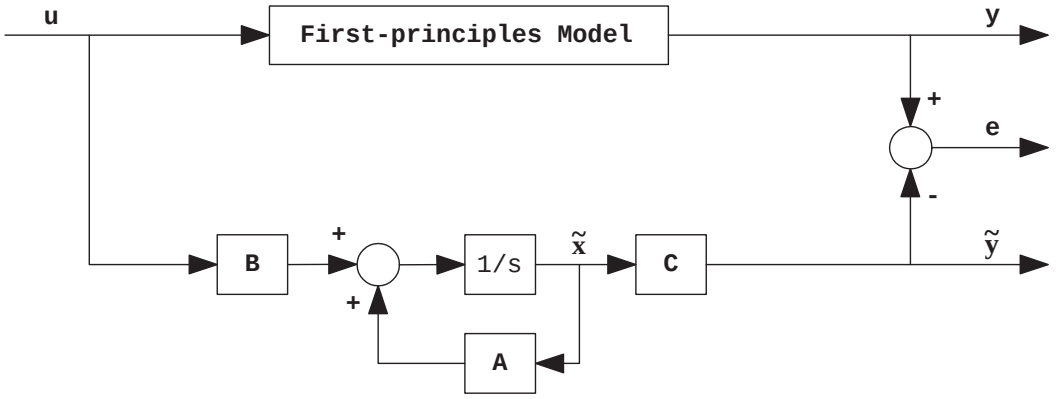

FIGURE B.2: Validation of the state space model

In order to validate the state space model, the CD thickness profile from the first-principles model ($\mathbf{y}$ or measurement) is compared with that from the state-space model ($\tilde{\mathbf{y}}$ or estimate). The configuration for this test is depicted in Figure B.2.

The test has been carried out for various actuator set-points ($\mathbf{u}$) and three of the steady state responses are depicted in Figures B.3, B.4, and B.5. The lower plots show the actuator set-points used for each test, and the upper plots depict the measurements and estimates.

The state-space model has been linearised about a range of the set-points between 0.35 to 0.45. However, the results shown in every figure illustrates that the model estimates follow the measurements closely even when the set-points are not within the range.

The state space model can now be employed as a reference model required for the new controller design and the fault monitoring system introduced in Chapters 5 and 6, respectively.

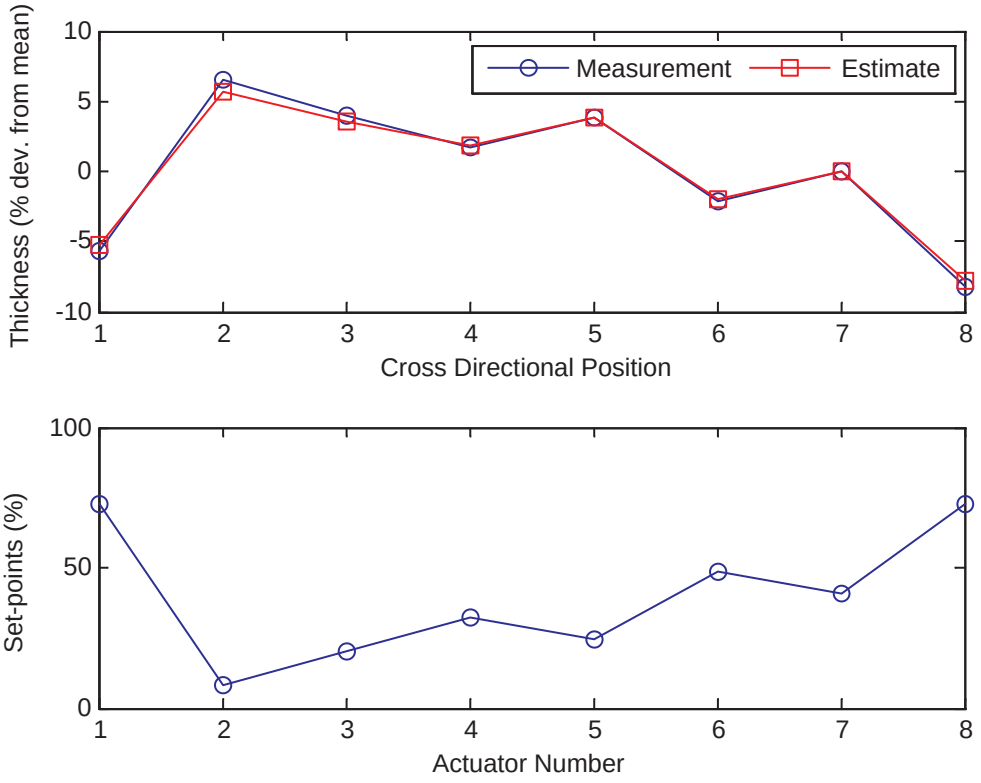

FIGURE B.3: Open-loop Test 1. Upper plot: measurements (y) and estimates ($\tilde{y}$). Lower plot: corresponding actuator set-points

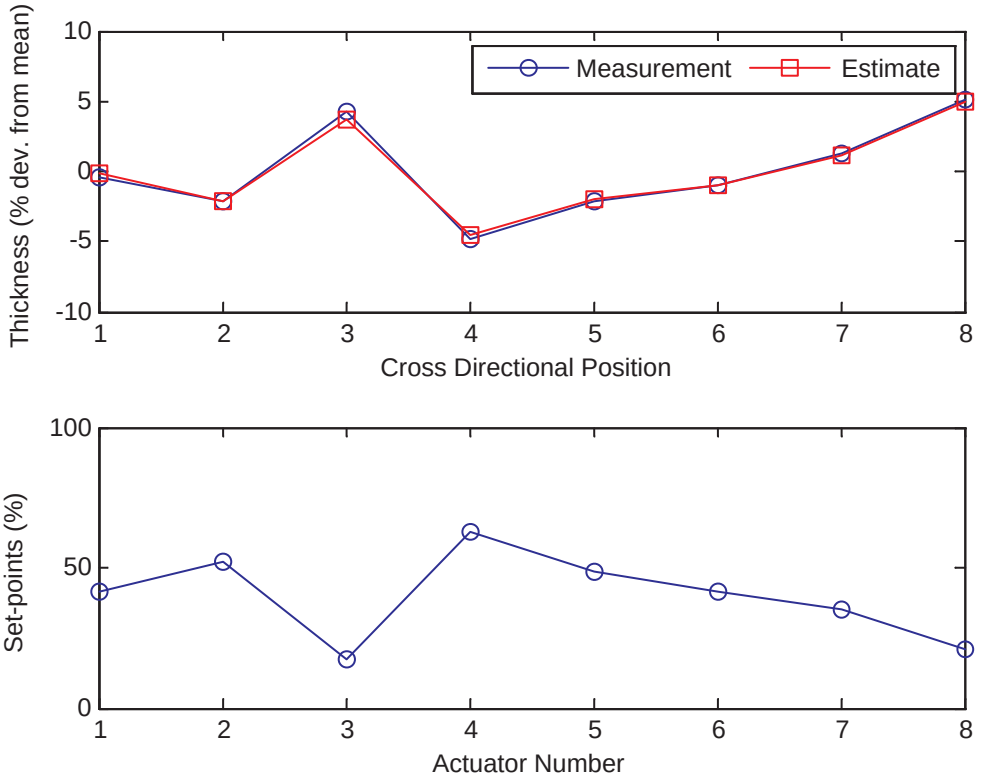

FIGURE B.4: Open-loop Test 2. Upper plot: measurements (y) and estimates ($\tilde{y}$). Lower plot: corresponding actuator set-points

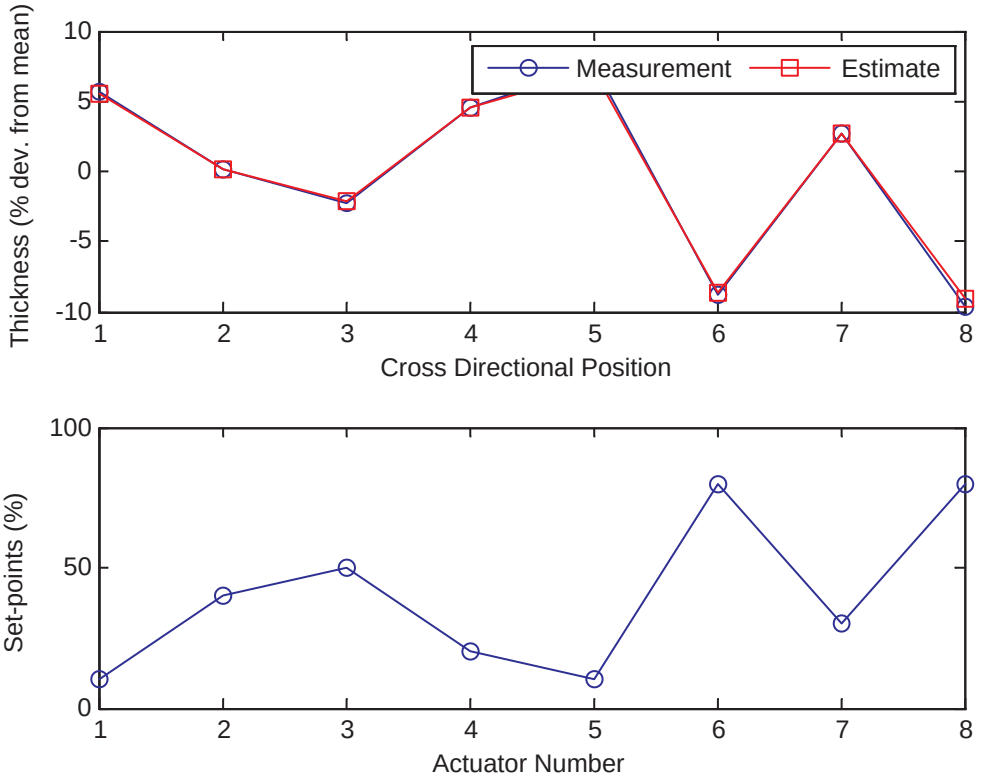

FIGURE B.5: Open-loop Test 3. Upper plot: measurements (y) and estimates ($\tilde{y}$). Lower plot: corresponding actuator set-points

Appendix C

Genetic Algorithm

Chapter 6 utilises a genetic algorithm for solving a multi-objective optimisation problem. Therefore, this appendix briefly summarises a genetic algorithm – detailed introduction to genetic algorithms can be found in many books and papers such as Coley (1999), Davis (1991), Frenzel (1993), Mitchell (1998), and Vose (1999).

Optimisation methods can be classified into calculus-based and direct-search methods (Christofides et al., 2009). Calculus-based methods are often gradient-descent methods, in which the gradients of the objective surface at the current position in every direction are computed, and the direction with the most negative slope is chosen. These methods work effectively when the objective surface is relatively smooth with few local minima. However, real-life data are often multi-modal and even contaminated by noise, which distort the objective surface even further. This increases the possibility of being trapped into local minima and thus decreases the possibility of reaching the global minimum – the optimal solution.

By contrast, the calculation of derivatives is not required for direct-search methods. Instead, parallel searching techniques, as opposed to point by point searching techniques used in calculus-based methods, are exploited, and therefore many regions of the search space can be explored simultaneously. This reduces the possibility of being trapped into local minima and increases the possibility of finding the global minimum.

A genetic algorithm is an evolutionary searching technique, which is a kind of parallel searching technique. It utilises Darwinian survival of the fittest strategy to eliminate unfit characteristics and uses and exchanges the knowledge contained in old solutions to evolve towards an acceptable solution.

C.1 Terminology

Before summarising a genetic algorithm, the terminology used in genetic algorithms is listed as follows:

- *Fitness function*: the objective function
- *Genes*: the elements of each individual
- *Individual and score*: If a fitness function, $f(x_1, x_2, x_3)$ was being minimised, a trial set for x_1, x_2, and x_3 would be an individual. The value of this fitness function would be a score or fitness measure
- *Parents and Children*: In order to produce the population in the next generation, the genetic algorithm selects individuals called parents and uses them to produce new individuals called children or offspring
- *Populations and Generations*: A population is an array of individuals. For instance, if the number of variables in the fitness function is 3 and the population is 10, then the population will be represented by a 10-by-3 matrix. Each successive population is known as a generation

C.2 Main Rules

The genetic algorithm exploits the following three rules at each generation:

- *Selection rule*: selects individuals (parents) that contribute to the population in the next generation.

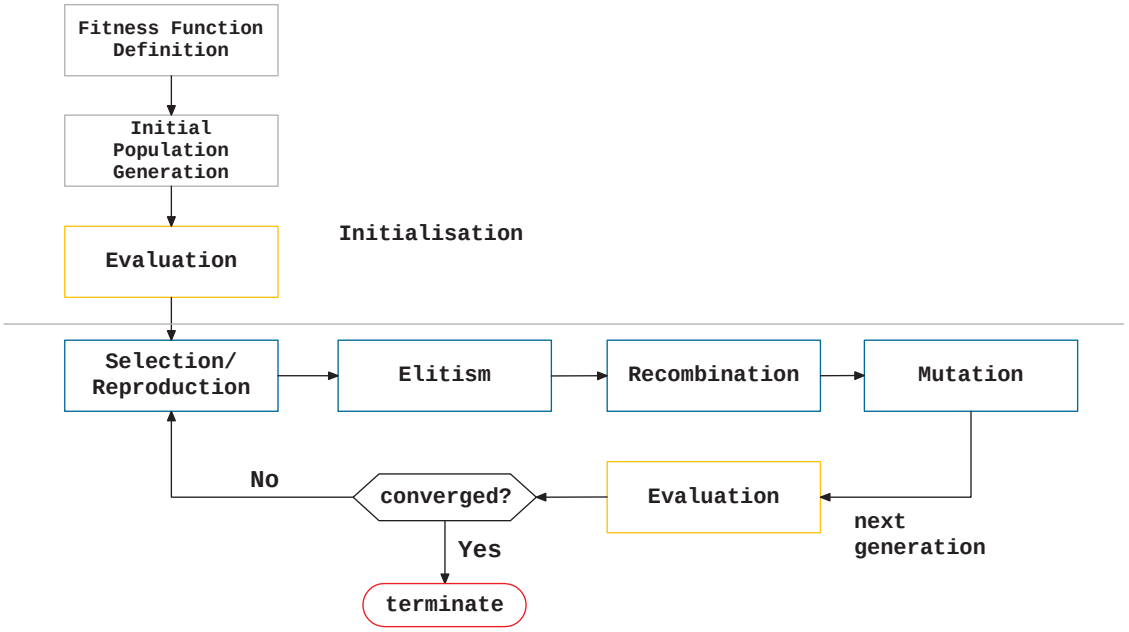

FIGURE C.1: Flow diagram of genetic algorithm

- *Crossover rule*: combines two individuals to produce children (offspring) for the population in the next generation.
- *Mutation rule*: applies random changes to individuals to produce children for the population in the next generation.

C.3 Procedures

The main stages involved in the genetic algorithm are depicted in Figure C.1 and summarised below.

Generation of Initial Population

A random initial population is generated.

Evaluation

Each individual is evaluated on how well it solves the optimisation problem. A score is given to each individual and this score is used in the next stage.

Reproduction

For every individual in the current population, a number of exact copies are created with the fittest individual, in terms of the score given in the previous stage, creating the most copies. The genetic algorithm thus takes advantage of a survival of the fittest strategy at this stage. There are several options to determine how many children each parent will reproduce, but "ratioing" and "ranking" are the options that are most commonly used.

In ratioing, each parent reproduces children in proportion to its score, that is, a parent whose score is 5 times better than another will reproduce 5 times the number of children. When superior parents emerge, they will guide the population more quickly, but the population may converge prematurely increasing the possibility of becoming trapped into local minima.

In ranking, the number of children each parent will reproduce is dependent on how it ranks in the population. For instance, the top 30% reproduce 2 children, the bottom 30% reproduce none, and the middle 40% reproduce 1 child each. The advantage and disadvantage of this option are the opposites of raioing.

Elitism

In order to prevent the fittest parents from failing to reproduce children for the next generation, this stage copies the fittest parents of each generation into the next generation. However, this stage may let superior parents dominate the population prematurely leading to local minima. Therefore, this stage should be avoided if there are too many local minima.

Recombination

Following reproduction and elitism, no individual can be different from the previous generation because they are basically the copies of the previous individuals. Recombination, on the other hand, combines individuals (parents) and reproduces new children that maintain many features from the previous generation although they never existed in the previous generation.

In "single point", which is one of the available options, two individuals are randomly chosen, and a subsection of one individual is swapped with a subsection of the other individual about a randomly chosen crossover point. On the other hand, "scattering", another option, generates a random binary vector. Then, the option selects genes where the vector is a 1 from the first parent and genes where the vector is a 0 from the second parent. For instance, let $\mathbf{P}_1 = [a\,b\,c\,d\,e\,f\,g]$ and $\mathbf{P}_2 = [1\,2\,3\,4\,5\,6\,7]$, then the randomly generated binary vector, $[1\,0\,0\,1\,0\,1\,0]$ will reproduce a crossover child, $[a\,2\,3\,d\,5\,f\,7]$.

In effect, this stage lets good individuals be combined with those that are not as good. However, it assumes that the best solution is not contained in each individual but is contained in the population as a whole and therefore can be found by combining individuals (Chen and Patton, 1999).

Mutation

New information is injected into the population by applying random changes to one or more parents in every generation. In most cases, a random number taken from a Gaussian distribution with mean zero is added to each element of the parent.

C.4 Summary

As depicted in Figure C.1, all the stages in the previous section except the first one repeat until the solution has converged. The genetic algorithm when combined with suitable algorithms can be utilised effectively for solving multi-objective optimisation problems as demonstrated in Section 6.2.

Appendix D

Sample Simulink® Models and Matlab® Files

The first-principles model is composed of many smaller Simulink® models, which further comprises many smaller Simulink modules. Most modules contain a Matlab® file, and it would therefore take too much space to present every model, module, and Matlab file. As a result, only a small number of samples of the Simulink models and modules and Matlab files contained within them are presented here.

D.1 Die Model

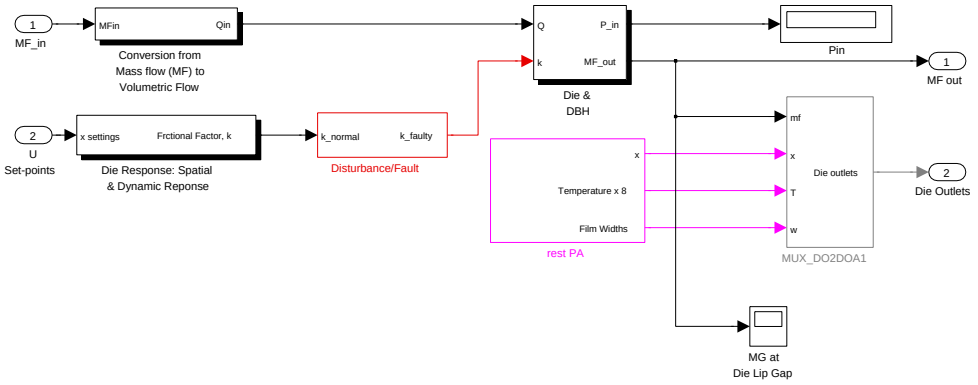

FIGURE D.1: Die model in Simulink®

The Matlab file contained within the module named "Die & DBH", in which all the main equations presented in Section 3.4 are stored, is as follows.

```
function [sys, x0, str, ts] = Die(t,x,u,flag, ...
    dialog_window_parameters)
switch flag,

case 0
%%%%%%%%%%%%%%%%%%%%%%%%%%%%
%%%%%% Initialization %%%%%%
%%%%%%%%%%%%%%%%%%%%%%%%%%%%
global n
sizes = simsizes;
sizes.NumContStates  = 0;
sizes.NumDiscStates  = 0;
sizes.NumOutputs     = n+1;
sizes.NumInputs      = n+1;
sizes.DirFeedthrough = 1;
sizes.NumSampleTimes = 0; % This is a continous time block
sys = simsizes(sizes);
str = [];
x0 = [];
ts  = [];

case 3
```

```
Pout = 1; %1 Bar (Approx.)

global n mju Lip Depth Hw
Q11 = u(1); % input volumetric flow

%%%%%%%%%%%%%%%%%%%%%%%%%%%%%%%%%%%%%%%%%%%%%%%%
%%%%%%% Retrieve DBH coefficients %%%%%%%%
%%%%%%%%%%%%%%%%%%%%%%%%%%%%%%%%%%%%%%%%%%%%%%%%
for i = 1:n
    k(i) = u(i+1);
end

%%%%%%%%%%%%%%%%%%%%%%%%%%%%%%
%%%%%%% Die geometry %%%%%%%
%%%%%%%%%%%%%%%%%%%%%%%%%%%%%%

% Half Lip Gaps
g=[];
for j=1:n
    g(1,j) = Hw(j);
end
for j=1:n
    g(2,j) = (Hw(j)+Lip/2)/2;
end
g(3,:) = Lip/2;

global WebWidth LandLength TL

% Nominal *Half* Lip Gap
NominalLipGap = 0;
for i=1:n
    NG = g(3,i);
    NominalLipGap = NG + NominalLipGap;
end
NominalLipGap = NominalLipGap/n;

% TA varies with position although triangle & taper angles don't
for i=1:n
    TA(i) = atan((Hw(i) - g(3,i))/TL);
end
```

```
% Area (vertical Flow)
for j=1:3
    for i=1:n
        vA(j,i) = (WebWidth/n) * g(j,i) * 2;
    end
end
% Area (horizontal flow, i.e., die body)
for i=1:n
    hA(i) = Hw(i) * ( 2*Depth(i) + (( (Cr^2) * (0.5*pi-2) , ...
        )) ) + Hw(i) * TL; % Hw(i) * TL = TrA + RcA
end

% Calculate X for the flow equations
for i=1:n
    if Depth(i) > Hw(i)
        W(i) = Depth(i);
    else
        W(i) = Hw(i);
    end
    X(i) = (2*Hw(i))/(W(i)+Hw(i));
end

% Length (vertical)
L = Depth;
L(2,:) = TL;
L(3,:) = LandLength;

% Coefficients of the equations
B=[];
C=[];
D=[];
E=[];
for i = 1:n
    B(i) = ( (Hw(i))^2 ) * hA(i);
    C(i) = mju * (3+X(i)) * (1+sqrt( X(i) ));
    for j = 1:3
        D(j,i) = (g(j,i)^2)*vA(j,i);
        E(j,i) = 3*mju*L(j,i);
    end
end

% Initialise matrix size according to number of sections
```

```
m_size = 9*n;
mA =zeros(m_size, m_size);

% Taper & land sections
c = 1; % column index
r = 1; % row index
r1 = 1;
r2 = 1;
    for j=1:n
        for i=1:3
            mA(r1,r1+2*n)  = -E(i,j);
            mA(r1,r2+5*n) =  D(i,j);
            mA(r1,r2+5*n+1) = -D(i,j);
            r1 = r1+1;
            r2 = r2+1;
        end
        r2=r2+1;
    end

% Body section
mA(r1,1) = B(1);
mA(r1,5*n+1) = -B(1);
r1 = r1+1;
c = 5*n+1;
for j=2:n
    mA(r1,j) = -C(j);
    mA(r1,c) = B(j);
    c = c+4;
    mA(r1,c) = -B(j);
    r1 = r1+1;
end
c1 = 5*n+4;
for j=1:n
    mA(r1,j+n) = -k(j);
    mA(r1,c1) = 1;
    c1 = c1+4;
    r1 = r1+1;
end

%%%%%%%%%%%%%%%%%%%%%%%%%%%%%%%%%%%%%%%%
%%%%%% Conservation of mass: Body %%%%%%
%%%%%%%%%%%%%%%%%%%%%%%%%%%%%%%%%%%%%%%%
```

```
c2 = n*2 +1; %c2 = 11; r1=26 for n=5
mA(r1,2) = 1;
mA(r1,c2) = 1;
r1 = r1+1; %r1 becomes 27 for n=5
c2 = c2+3; %c2 =14

for j=2:n-1
    mA(r1,j) = 1;
    mA(r1,j+1) = -1;
    mA(r1,c2) = -1;
    c2 = c2+3;
    r1 = r1+1;
end
mA(r1,j+1) = 1;
mA(r1,c2) = -1;

%%%%%%%%%%%%%%%%%%%%%%%%%%%%%%%%%%%%%%%%
%%%%% Conservation of Mass: Rest %%%%%
%%%%%%%%%%%%%%%%%%%%%%%%%%%%%%%%%%%%%%%%
j2 = r1+3; %j2 = 33
r1 = r1+1; %31 for n=5
for i=1:3*n
    mA(r1,n*2+i) = -1;
    mA(r1,n*2+i+1) = 1;
    r1=r1+1;
end
j = 2*n + 1;
for i=1:n
    mA(j2,i+n) = 1;
    mA(j2,j+i*3) = 0;
    j2 = j2+3;
end

mB =zeros(n*9,1);
mB(3*n+1) = C(1) * Q11;
for i=1:n
    mB(3*n+n+i) = Pout;
end
mB(n*5+1) = Q11;


mX = inv(mA)*mB; %   [
```

```
%   P10
%   Q12
%   Q13
%   Q14
%   Q15

%   Q51
%   Q52
%   Q53
%   Q54
%   Q55

%   Q21
%   Q31
%   Q41

%   Q22
%   Q32
%   Q42

%   Q23
%   Q33
%   Q43

%   Q24
%   Q34
%   Q44

%   Q25
%   Q35
%   Q45


%   P11
%   P21
%   P31
%   P41

%   P12
%   P22
%   P32
%   P42
```

```
                %   P13
                %   P23
                %   P33
                %   P43

                %   P14
                %   P24
                %   P34
                %   P44

                %   P15
                %   P25
                %   P35
                %   P45
                %   ]
%%%%%%%%%%%%%%%%%%%%%%%%%%%%%%%%%%%%%%%%%%%%%%%%%%%%%%%%%%%%%%%%%%%%%%%
%%%% Find matrix column and row indices with non-zeros %%%%
%%%%%%%%%%%%%%%%%%%%%%%%%%%%%%%%%%%%%%%%%%%%%%%%%%%%%%%%%%%%%%%%%%%%%%%
x = [];
i=1;
for r=1:n*9
    for c=1:9*n
        if mA(r,c) ~= 0
            x(i,:) = [r c];
            i = i+1;
        end
    end
end
Vout = mX(n+1:n+5);
Pin = mX(1);

P41 = mX(29);
P42 = mX(33);
P43 = mX(37);
P44 = mX(41);
P45 = mX(45);

Q51 = mX(6);
Q52 = mX(7);
Q53 = mX(8);
Q54 = mX(9);
```

```
Q55 = mX(10);

dP1=P41-1;
dP2=P42-1;
dP3=P43-1;
dP4=P44-1;
dP5=P45-1;

density = 1250;
MF = mX(n+1:n*2) *density;
% MFin = Qin*density;

coeff1=[];
for i=1:n
    coeff1 = [coeff1 C(i)/B(i)];
end

coeff2=[];
for i=1:3
    for j=1:n
        coeff2 = [coeff2 E(i,j)/D(i,j)];
    end
end

sys = [MF; Pin];

case { 1, 2, 4, 9}
sys = [];


end
```

D.2 Casting Model

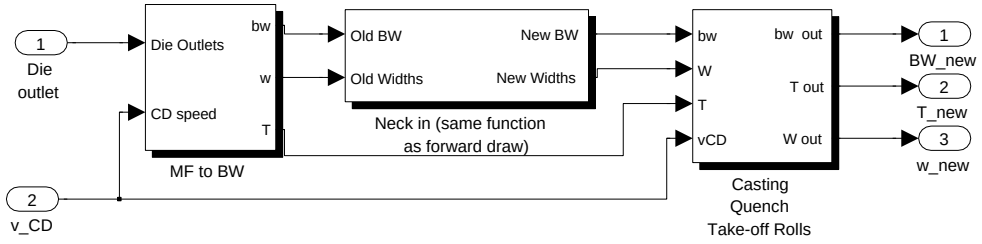

FIGURE D.2: Casting model in Simulink®

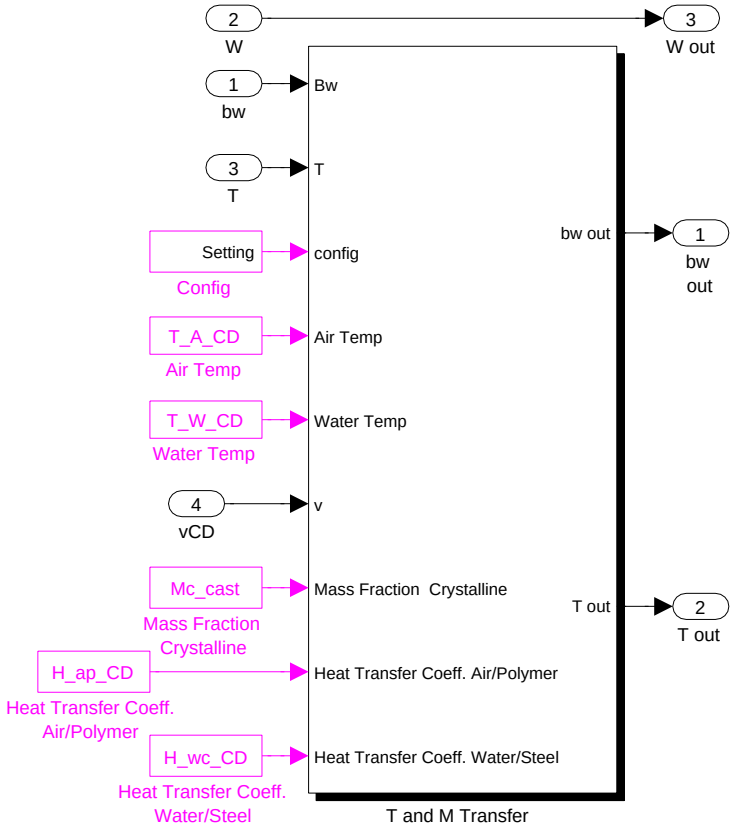

FIGURE D.3: Heat and mass transfer module in Simulink®

All the equations presented in Section 3.5 are contained within the first two modules depicted in Figure D.2. The third module is the mass and heat transfer

module which is common to all other models except the die model. The Matlab file stored inside the mass and heat transfer module is as follows.

```
function [sys, x0, str, ts] = Mass_Heat_Transfer(t,x,u,flag,p1,p2)

switch flag,

case 0
%%%%%%%%%%%%%%%%%%
% Initialization %
%%%%%%%%%%%%%%%%%%
global n
m = p2; % Number of Sections (in x/machine direction)
sizes = simsizes;
sizes.NumContStates  = 2*m*n;
sizes.NumDiscStates  = 0;
sizes.NumOutputs     = 2*n;
sizes.NumInputs      = 2*n + 6*m + 2 + 2*m;
sizes.DirFeedthrough = 0;
sizes.NumSampleTimes = 1; % This is a continous time block
sys = simsizes(sizes);
str = [];
x0 = [];
for i=1:n
    for i=1:m
        x0 = [x0 1];
    end
end
for i=1:n
    for i=1:m
        x0 = [x0 273];
    end
end

ts  = [0 0]; % for continuous states
case 1
%%%%%%%%%%%%%%%%
% Deriviatives %
%%%%%%%%%%%%%%%%
```

```
%%%%%%%%%%%%%%%%%%%%%%%%%%%%%%%%
%%%%%%%% Initiallisation %%%%%%%%
%%%%%%%%%%%%%%%%%%%%%%%%%%%%%%%%
global n density % Number of Lanes & Density
m = p2; % Number of Sections

%%%%%%%%%%%%%%%%%%%%%%%%%%%%%%%%
%%%%%%%%% INPUTS %%%%%%%%%%%%%%%
%%%%%%%%%%%%%%%%%%%%%%%%%%%%%%%%
% Input(u) will be: (for n=2 & m=3)
% [Bw0(1);Bw0(2);T0(1);T0(2)];
j=1;
for i=1:n
    Bw0(i)=u(j);
    j=j+1;
end
for i=1:n
    T0(i) = u(j); % input T
    j=j+1;
end
%%%%%%%%%%%%%%%%%%%%%%%%%%%%%%%%%%%%%%%%%%%%%%%%%%%%%%%%%%%%%%%%%%%%%%%
%%%%%%%%%%%% Top and Bottom Configuration %%%%%%%%%%%%%%
%%%%%%%%%%%%%%%%%%%%%%%%%%%%%%%%%%%%%%%%%%%%%%%%%%%%%%%%%%%%%%%%%%%%%%%
jo = j+m-1;
TopAir = u(j:jo);
j= jo+1;
jo = j+m-1;
TopCyl = u(j:jo);
j= jo+1;
jo = j+m-1;
BotAir = u(j:jo);
j= jo+1;
jo = j+m-1;
BotCyl = u(j:jo);

%%%%%%%%%%%%%%%%%%%%%%%%%%%%%%%%%%%%%%%%%%%%%%%%%%%%%%%%%%%%%%%%%%%%%%%
%%%%%%%%% Top and Bottom Configuration END %%%%%%%%%%%
%%%%%%%%%%%%%%%%%%%%%%%%%%%%%%%%%%%%%%%%%%%%%%%%%%%%%%%%%%%%%%%%%%%%%%%
jo = jo+1;
Tw = u(jo:jo+m-1); % Water Temperature
jo = jo+m;
Ta = u(jo:jo+m-1); % Air Temperature
```

```
jo = jo+m;
v = u(jo); % Speed
jo = jo+1;
Mc = u(jo); % Mass Fraction Crystalline required in function
            % 'Specific_Heat_Capacity'
jo = jo+1;
hap = u(jo:jo+m-1); % heat transfer coeff. from air to polymer
            % (5 outside stenter according to 9 in notes)
jo = jo+m;
hwc = u(jo:jo+m-1); % heat transfer coeff. from water to
                    % cylinder
%%%%%%%%%%%%%%%%%%%%%%%%%%%%%
%%%%%%%% INPUTS END %%%%%%%%%
%%%%%%%%%%%%%%%%%%%%%%%%%%%%%

%%%%%%%%%%%%%%%%%%%%%%%%%%%%%%%%%%%%%%%%%%%%%%%%%%%%%%%%%%%%%%%%%%%%%%%
%%% Parameters, i.e., according to heat transfer data by DTF %%%
%%%%%%%%%%%%%%%%%%%%%%%%%%%%%%%%%%%%%%%%%%%%%%%%%%%%%%%%%%%%%%%%%%%%%%%
Lp=Bw0/density; % Lp (thickness of lanes) different for different
                %lanes
Lp_mean=mean(Lp); % emissivity function requires mean thickness to
                  %calculate eps
eps=emissivity(Lp_mean); % function emissivity calculates eps
                         % using thickness
To=mean(T0); % Mean temperature required by
             % Specific_Heat_Capacity function
Cp=Specific_Heat_Capacity(Mc,To); % specific heat capacity
                                  % in J/kg.K

dx = p1; % x in m, i.e., [1 0.8 0.3,...] whereas p2 is length
         % of p1
sig = 5.67 * (10^-8); % Stefan-Boltz constant in W/(m^2.K^2)

%%%%%%%%%%%%%%%%%%%%%%%%%%%%%%%%%%%%%%%%%%%%%%%%%%%%%%%%%%%%%%%%%%%%%%%
% Finding hwp & hsp, i.e., total heat transfer coeff. from water %
%%%%%%%%%%%%%% to polymer and surroundings to polymer %%%%%%%%%%%
%%%%%%%%%%%%%%%%%%%%%%%%%%%%%%%%%%%%%%%%%%%%%%%%%%%%%%%%%%%%%%%%%%%%%%%

Kp = 0.21; % Polymer Conductivity [W/mk] 0.15 for finished film
           %(from DTF's
           %Heat Transfer Data)
Kc = 16; % Steel Conductivity [W/mk]
```

```
hsp=[];
hwp=[];

for j=1:m
    dummy_hsp=[];
    dummy_hwp=[];
    for i=1:n
        Lc = 0.0127; % thickness of cylinder (from DTF's
                     % Heat Transfer Data)
        hp = Kp/(Lp(i)/2); % heat transfer coeff. inside polymer
                           %(Half only)
        hc = Kc/Lc; % heat transfer coeff. inside cylinder
        %%% DETETED according to 9 in DTF Heat Transfer notes;
        % may be too small
        % and neglected (1/hcp) %%%%
        %hcp = hp*0.5; % heat transfer coeff. from cylinder to
        % polymer (estimated)
        % total heat transfer coefficient (hsp) from surrounding
        % to polymer
        % air-polymer; insider-polymer
        hsp_i = (1/hp)+(1/hap(j));
        hsp_i = 1/hsp_i;
        % total heat transfer coefficient (hsp) from surrounding
        % to polymer
        % water-cylinder; inside-cylinder; cylinder-polymer;
        % inside-polymer(half)
        % hwp_i = (1/hp) + (1/hcp) + (1/hc) + (1/hwc);
        hwp_i = (1/hp) + (1/hc) + (1/hwc(j)); %  (1/hcp)  deleted
        hwp_i = 1/hwp_i;
        dummy_hsp = [dummy_hsp hsp_i];
        dummy_hwp = [dummy_hwp hwp_i];
    end
    hsp(j,:)=dummy_hsp;
    hwp(j,:)=dummy_hwp;
end
%%%%%%%%%%%%%%%%%%%%%%%%%%%%%%%%%%%%%%%%%%%%%%%%%%%%%%%%%%%%%%%%%%%%%%%%
%%%%%%%%%%%%%%%%%%%% End of hwp & hsp %%%%%%%%%%%%%%%%%%%%%%%%%%%%%%%%%%
%%%%%%%%%%%%%%%%%%%%%%%%%%%%%%%%%%%%%%%%%%%%%%%%%%%%%%%%%%%%%%%%%%%%%%%%
j=0;
for jo=1:n
    for i=1:m
```

```
        j=j+1;
        Bw(j) = x(j);
    end
end
io=0;
for jo=1:n
    for i=1:m
        io=io+1;
        j=j+1;
        T(io) = x(j);
    end
end

%%%%%%%%%%%%%%%%%%%%%%%%%%
%%%%% Main Equations %%%%%
%%%%%%%%%%%%%%%%%%%%%%%%%%

% Starting Section
i=0;
jo=0;
for j=1:n
    i1 = 1;
    i=i+1;
    jo=jo+1;
    dBWdt(i) = v*(Bw0(jo) - Bw(i))/dx(i1); % Basis Weight Transfer
    % NOTE Qmt = Qmt/CpBwdxdy etc
    % "Qmt" for heat transfer between sectons
    % "Qwp" for heat transfer from water to polymer
    % (water-cylinder, surface-polymer)
    % "Qsp" for heat transfer from surroundings to polymer
    % (surroundings-polymer)
    Qmt = (v*(T0(jo)-T(i)) / dx(i1)); % always here
    Qwp_top = (((hwp(i1,j)/(Bw(i)*Cp))*(Tw(i1)-T(i))))*TopCyl(i1);
                                    % Top exposed to water-cylinder
    Qwp_bot = (((hwp(i1,j)/(Bw(i)*Cp))*(Tw(i1)-T(i))))*BotCyl(i1);
                                  % Botom Exposed to Water-Cylinder
    Qsp_top = ((eps*sig/(Cp*(Bw(i))))*((Ta(i1)^4)- (T(i)^4)) + ...
        (hsp(i1,j)/(Bw(i)*Cp))*(Ta(i1)-T(i)))*TopAir(i1); %Top
                                                    %Exposed to air
    Qsp_bot = ((eps*sig/(Cp*(Bw(i))))*((Ta(i1)^4)- (T(i)^4)) ...
        + (hsp(i1,j)/(Bw(i)*Cp))*(Ta(i1)-T(i)))*BotAir(i1); %Bot-
                                                % tom Exposed to air
```

```
    dTdt(i) = (Qmt + Qwp_top + Qwp_bot+Qsp_top+Qsp_bot);

    % Following Sections
    for io=1:m-1
        i=i+1;
        i1=i1+1;
        %%% BW %%%
        dBWdt(i) = v*(Bw(i-1) - Bw(i))/dx(i1); % Basis Weight
                                               % Transfer
        %%% T %%%
        Qmt = (v*(T(i-1)-T((i))) / dx(i1));
        Qwp_top = (((hwp(i1,j)/(Bw(i)*Cp))*(Tw(i1)-T(i)))) ...
            *TopCyl(i1);
        Qwp_bot = (((hwp(i1,j)/(Bw(i)*Cp))*(Tw(i1)-T(i)))) ...
            *BotCyl(i1);
        Qsp_top = ((eps*sig/(Cp*(Bw(i))))*((Ta(i1)^4)- (T(i)^4)) ...
            + (hsp(i1,j)/(Bw(i)*Cp))*(Ta(i1)-T(i)))*TopAir(i1);
        Qsp_bot = ((eps*sig/(Cp*(Bw(i))))*((Ta(i1)^4)- (T(i)^4)) ...
            + (hsp(i1,j)/(Bw(i)*Cp))*(Ta(i1)-T(i)))*BotAir(i1);
        dTdt(i) = (Qmt + Qwp_top + Qwp_bot+Qsp_top+Qsp_bot);
    end
end

dxdt = [dBWdt dTdt];

sys = dxdt;
% Output, e.g.,
% = [Bw*m for lane1, Bw*m for lane 2, etc]

case 3
%%%%%%%%%%
% Output %
%%%%%%%%%%
global n
m = p2;
j=1;
j1=1;
i=1;
BW_f = x(1:length(x)/2);
T_f  = x((length(x)/2)+1:end);
for jo=1:m
    for io=1:n
```

```
        BW_m(i)=BW_f(j);
        T_m(i)=T_f(j);
        j=j+m;
        i=i+1;
    end
    j1=j1+1;
    j=j1;
end
x=[BW_m(end-(n-1):end)  T_m(end-(n-1):end)];
sys = x;

case { 2, 4, 9}
%%%%%%%%
% else %
%%%%%%%%

sys = [];


end % switch
```

D.3 Stenter Oven Model

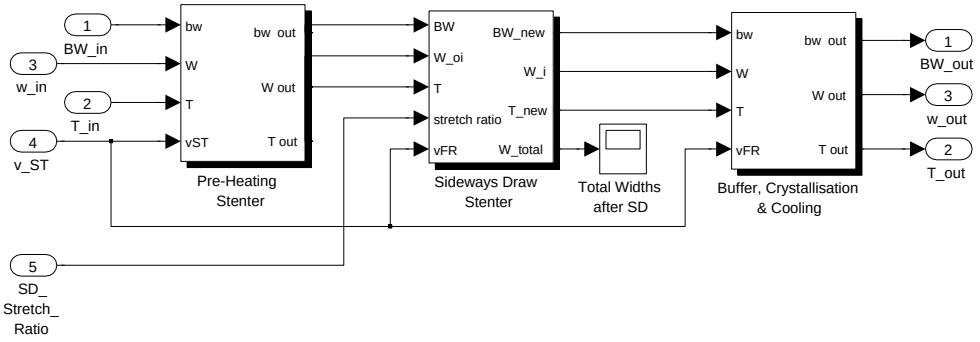

FIGURE D.4: Stenter oven model in Simulink®

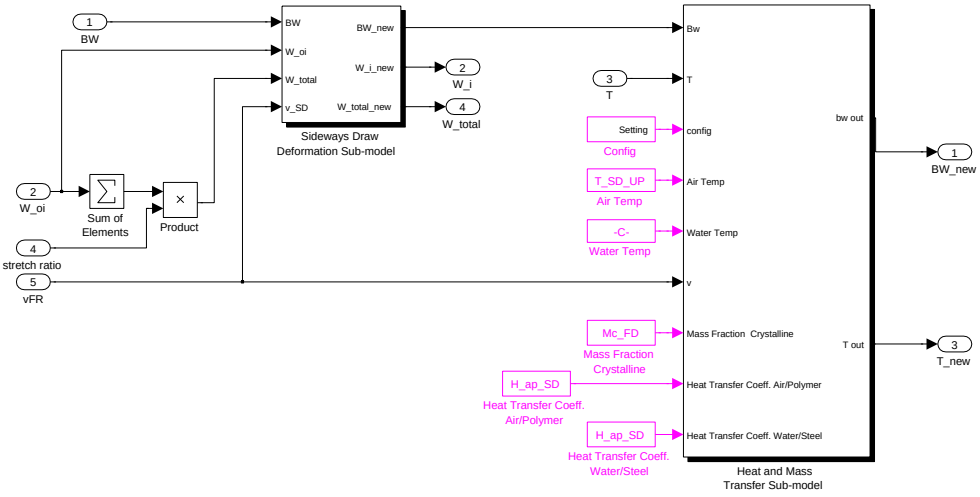

FIGURE D.5: Sideways-draw model with 2 modules in Simulink®

The stenter oven model is comprised of three smaller models as shown in Figure D.4. As depicted in Figure D.5, the sideways-draw model is composed of the mass and heat transfer module presented in the previous section and a deformation module. The Matlab file contained within this deformation module is written using the equations presented in Section 3.9.1 as follows.

```
function [sys, x0, str, ts] = Sideways(t,x,u,flag, ...
    dialog_window_parameters)

switch flag,

case 0

%%%%%%%%%%%%%%%%%%%
% Initialization %
%%%%%%%%%%%%%%%%%%%
global n
sizes = simsizes;
sizes.NumContStates  = 0;
sizes.NumDiscStates  = 0;
sizes.NumOutputs     = n*2+1;
sizes.NumInputs      = n*2+2;
sizes.DirFeedthrough = 1;
sizes.NumSampleTimes = 0; % This is a continous time block
sys = simsizes(sizes);
str = [];
x0 = [];
ts  = [];

case 3
%%%%%%%%%%%%%%%%%%%%%%
%%%%%%% Inputs %%%%%%%
%%%%%%%%%%%%%%%%%%%%%%
global density n TDX
BWoi = u(1:n);
Woi = u(n+1:2*n);
Wo  = sum(Woi);
W = u(2*n+1);
v_SD=u(2*n+2);
TDX = W/Wo;

%%%%%%%%%%%%%%%%%%%%%%%%%%%%%%%%%%
%%%%%%%% For step ratio %%%%%%%%%%
%%%%%%%%%%%%%%%%%%%%%%%%%%%%%%%%%%
global Wold
Wold = [Wold W];

if Wold(end) ≠ Wold(end-1)
```

```
    global iter % if this line is missed out, iter will
                % automatically be set
                % to global iter and global iter will not
                % be zero
    iter = 0;   % reset iter to 0 if W
                %(stretched total width, i.e., TDX) changes
end

%%%%%%%%%%%%%%%%%%%%%%%%%%%%%%%%
%%%%%% Initiallisation %%%%%%%%
%%%%%%%%%%%%%%%%%%%%%%%%%%%%%%%%
if (BWoi(1) ≠ 0) & (Wo≠0)
global BW_old
e = (W-Wo)/Wo; % Total strain between 0 - 1
HToi = BWoi./density; % HTo for initial height
L = ones(n,1); % L remains constant during stretching;
               % for all the lanes are the same
               % Changing L should only make difference to
               % Force, not "Stress and Strain"
Aoi = L .* HToi; % Initial Area of lanes

global iter
if iter == 0
    iter;
    %%%%%%%%%%%%%%%%%%%%%%%%%%%%%%%%%%%%%%%%%%%%%%%%%%%%
    %%%%%%% "fsolve" carried out once first %%%%%%%
    %%%%%%%%%%%%%%%%%%%%%%%%%%%%%%%%%%%%%%%%%%%%%%%%%%%%

    %%%%%%%%%%%%%%%%%%%%%%%%%%%%%%%%%%%%%%%%%%%%%%%%%%%%%%%%%%%%%%%%%%%%%%%
    % Compute for stresses and strains in the sideways draw %
    %%%%%%%%%%%%%%%%%%%%%%%%%%%%%%%%%%%%%%%%%%%%%%%%%%%%%%%%%%%%%%%%%%%%%%%
    est_o = [3*ones(n,1);3];
    options = optimset('Display','off');  % Turn off Display
    x=fsolve(@(x)solve_sideways_draw_prob_2(x,Aoi,n,e, ...
        Woi,v_SD),est_o,options);
    global est
    est = x;
    global x_old
    x_old = x;
end
%%%%%%%%%%%%%%%%%%%%%%%%%%%%%%%%%%%%%%%%%%%%%%%%%%%%%%%%
%%%%%% "fsolve" only used when BW ≠ BW_old %%%%%%
```

```
%%%%%%%%%%%%%%%%%%%%%%%%%%%%%%%%%%%%%%%%%%%%%%%%%%%%%
iter = iter + 1;
BW_old = [BW_old,BWoi(1)];
BW_old(iter);
if iter > 1 %to avoid(BW_old(0))
    if abs(BW_old(iter) - BW_old(iter-1)) < (10^-4)
    %if BW_old(iter) == BW_old(iter-1)
        global x_old
        x = x_old;
    else
        global est
        options = optimset('Display','off');
        [x,fval,ef,op]=fsolve(@(x)solve_sideways_draw, ...
            _prob_2(x,Aoi,n,e,Woi,v_SD),est,options);
        est = x;
        global x_old
        x_old = x;
    end
end

%%%%%%%%%%%%%%%%%%%%%%%%%%%%%%
%%%%%% Extract strains %%%%%%
%%%%%%%%%%%%%%%%%%%%%%%%%%%%%%
strain = x(1:n);
for i = 1:n,
    Wi(i) = Woi(i) * (x(i)+1);
    HTi(i) = ((Woi(i))/(Wi(i)))*HToi(i); %HT for new height;
                                         %V before and after is same
    BWi(i) = HTi(i) * density;
end
Wi=Wi'; % New Widths
HTi = HTi'; % New thickness
BWi = BWi'; % New basis weight

%%%%%%%%%%%%%%%%%%%%
%%%%%% Output %%%%%%
%%%%%%%%%%%%%%%%%%%%
Wtot = sum(Wi);
sys = [BWi; Wi; Wtot];

else
    sys =[];
```

```
end

case { 1, 2, 4, 9}
sys = [];

end
```

```
%%%%%%
%%%%%% Function used when solving sideways draw problem
%%%%%%
function r= solve_sideways_draw_prob_2(x,A0,n,e_tot,Woi,v_SD)
% Woi should be Width of each section = Wo/n
e=(x(1:n)); % Strain in each section
F=(x(n+1)); % The force pulling each section (same everywhere)
r=[]; % Residual (should be zero when solution has been found)
% Equations to ensure that the increases in lengths in each section
% matches the total increase in length

%r=[r;Woi*n*1/(1-e_tot)-sum(Woi*1./(1-e))]; % Engineering Strain

Wo = sum(Woi);
r=[r; Wo*(e_tot+1) - sum(Woi.*(e+1))];

% Equations that connects the strain to the stresses
for i = 1:n,
  r = [r;(2*F)/(A0(i)*(1-e(i)))-s2s(e(i),v_SD)]; % Main equations
end;
return;
```

```
function stress = s2s(strain,v_SD) % means strain to stress
                 %(note this is just an example implementation)

% Variables are obtained from the 'Line Simulator Presentation'
% and the 'm-file'
global TDX
ExitSpeed = v_SD; % m/sec
TdStretchTemp = T_td;
Epsilon = strain;
% "Stress" function cannot be shown due to confidentiality
% reasons
```

```
stress=Stress(Epsilon,TdStretchTemp,ExitSpeed,TDX);
```

D.4 Combined Model

The combined model is depicted in Figure D.6.

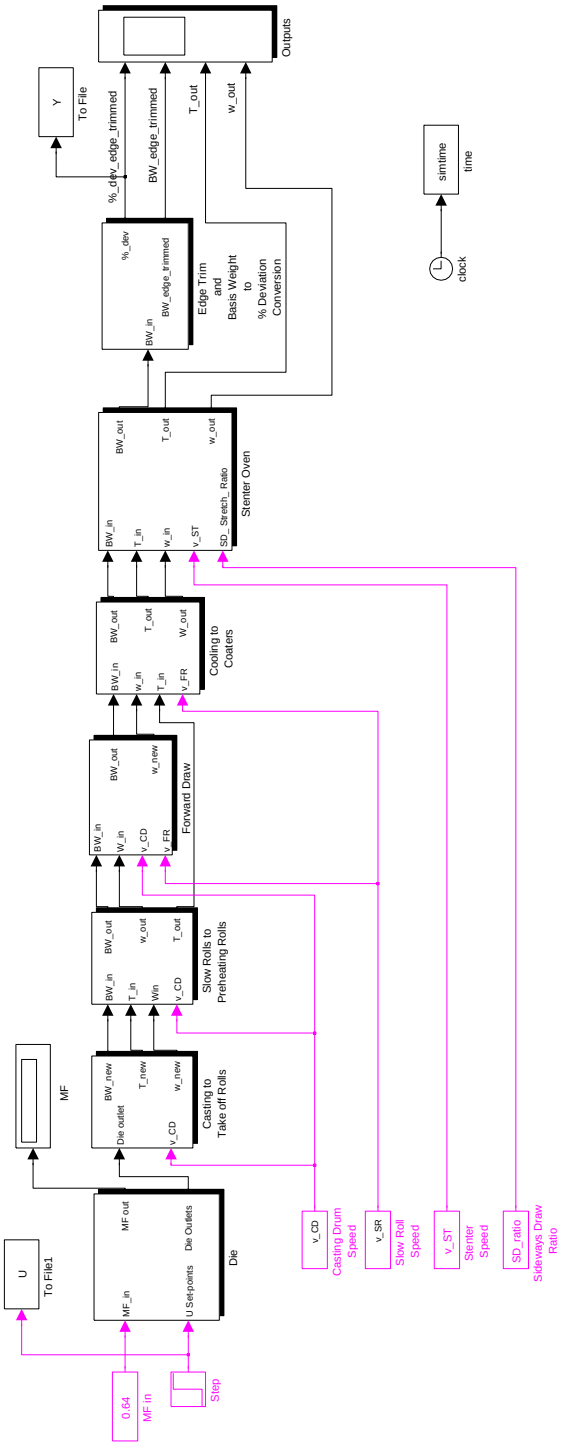

FIGURE D.6: First-principles model in Simulink®

Bibliography

Åström, K.J. (1973). On self tuning regulators. *Automatica*, 9, 185–199.

Åström, K.J. (1977). Theory and application of self-tuning regulators. *Automatica*, 13.

Arkun, Y. and Kayihan, F. (1998). A novel approach to full cross-directional profile control of sheet-forming processes using adaptive principle component analysis and reduced order internal model control design. *Computers and Chemical Engineering*, 22, 945–962.

Balderud, J. (2004). *Model-assisted optimization of a multi-ply paper board machine*. Ph.D. thesis, Department of Chemical Engineering, Karlstad University, Sweden.

Bialkowski, W.L. (1978). Application of steady state Kalman filters - theory with field results. In *Proceedings of the Joint Automatic Control Conference*.

Bialkowski, W.L. (1983). Application of Kalman filter to the regulation of dead time processes. *IEEE Transaction on Automatic Control*, 28, 400–406.

Cegrell, T. and Hedqvist, T. (1975). Successful adaptive control of paper machines. *Automatica*, 11, 53–59.

Chen, J. and Patton, R.J. (1999). *Robust model-based fault diagnosis for dynamic systems*. Kluwer Academic Publishers.

Chiang, L., Russell, E., and Braatz, R. (2001). *Fault Detection and Diagnosis in Industrial Systems*. Advanced Textbooks in Control and Signal Processing. Springer.

Christofides, P.D., Armaou, A., Lou, Y., and Varshney, A. (2009). *Control and Optimization of Multiscale Proess Systems*. Birkhauser.

Coley, D.A. (1999). *An Introduction to Genetic Algorithms for Scientists and Engineers*. World Scientific Publishing Co Pte Ltd.

Coulson, J.M. and Richardson, J.F. (1999). *Chemical Engineering*, volume 1. Elsevier, sixth edition.

Davis, L. (1991). *Handbook of Genetic Algorithms*. Van Nostrand Reinhold Company.

Deckert, J., Desai, M., Deyst, J., and Willsky, A. (1977). F-8 dfbw sensor failure identification using analytic redundancy. *IEE Transactions on Automatic Control*, 22, 795–803.

Dorf, R.C. and Bishop, R.H. (2008). *Modern Control Systems*. Pearson Prentice Hall, eleventh edition.

DTF (2005). Notes regarding the development of a whole film line profile prediction model. Company Confidential Document.

DTF (2006a). Die gap theory. Company Confidential Document.

DTF (2006b). Line simulator: algorithm summary. Company Confidential Document.

DTF (2007a). Die reponse. Company Confidential Document.

DTF (2007b). Heat transfer data for strathclyde case project. Company Confidential Document.

DTF (2007c). Standard conditions print 1. Company Confidential Document.

DTF (2007d). Standard conditions print 2. Company Confidential Document.

DTF (2009). Industrial fault data. Company Confidential Document.

Dumont, G. (1989). Application of advanced control methods in the pulp paper industry - a survey. *Automatica*, 22, 143–153.

Duncan, S.R. and Bryant, G.F. (1997). The spatial bandwidth of cross-directional control systems for web processes. *Automatica*, 33(2), 139–153.

Featherstone, A.P. and Braatz, R.D. (1998). Input design for large-scale sheet and film processes. *Ind. Eng. Chem. Res.*, 37, 449–454.

Featherstone, A., VanAntwerp, J., and Braatz, R. (2000). *Identification and control of sheet and film processes.* Advances in Industrial Control. Springer, London.

Frank, P.M. (1990). Fault diagnosis in dynamic systems using analytical and knowledge based redundancy - a survey and some new results. *Automatica*, 26(3), 459–474.

Frenzel, J.F. (1993). Genetic algorithms. *IEEE Potentials*, 12(3), 21–24.

Gertler, J.J. (1998). *Fault Detection and Diagnosis in Engineering Systems.* Marcel Dekker, Inc., New York.

Glawe, A. (2009). Functional coating technologies for innovative products with new properties on the field of nano coating and surface functionalisation. In *Proceedings of 29th International Exhibition-Congress on Chemical Engineering, Environmental Protection and Biotechnology.* COATEMA Coating Machinery GmbH.

Goodwin, G.C., Carny, B.M., and Edwards, W.J. (1990). Analysis of thermal camber control in rolling mills. In *Proceedings of the IFAC world congress, Tallinn, USSR.*

Gorinevsky, D., Vyse, R., and Heaven, M. (2000). Performance analysis of cross-direction process control using multivariable and spectral models. *IEEE Transactions on Control Systems Technology*, 8(4), 589–600.

Gorinevsky, D. and Gheorghe, C. (2003). Identification tool for cross-directional processes. *IEEE Transactions on Control Systems Technology*, 11(5), 629–640.

Grimble, M.J. (2001). *Industrial Control Systems Design.* Wiley.

Grimble, M.J. and Johnson, M.A. (1988). *Optimal control and stochastic estimation: theory and applications.* Wiley.

Hearn, E.J. (2001). *Mechanics of Materials 1.* Butterworth Heinemann, third edition.

Heath, W.P. (1996). Orthogonal functions for cross-directional control of web-forming processes. *Automatica*, 32, 183–198.

Heath, W.P. and Wills, A.G. (2002). Design of cross-directional controllers with optimal steady state performance. Technical report, Centre for Integrated Dynamics And Control (CIDAC), University of Newcastle, NSW, 2380, Australia.

Heath, W.P. and Wills, A.G. (2003). Design of cross-directional controllers with optimal steady state performance. Technical report, Centre for Integrated Dynamics And Control (CIDAC), University of Newcastle, NSW, 2380, Australia.

Heath, W.P. and Wills, A.G. (2004). Robust cross-directional control of paper making machines with saturating actuators. Technical report, Centre for Integrated Dynamics And Control (CIDAC), University of Newcastle, NSW, 2380, Australia.

Hertzberg, R.W. (1996). *Deformation and fracture mechanics of engineering materials*. John Wiley & Sons, Inc., fourth edition.

Himmelblau, D.M. (1978). *Fault Detection and Diagnosis in Chemical and Petrochemical Processes*. Elsevier Scientific Publishing Company.

Holman, J.P. (2001). *Heat Transfer*. McGraw Hill, ninth edition.

Incropera, F.P., Dewitt, D.P., Bergman, T.L., and Lavine, A.S. (2007). *Fundamentals of Heat and Mass Transfer*. John Wiley & Sons, sixth edition.

Iri, M., Aoki, K., O'Shima, E., and Matsuyama, H. (1979). An algorithm for diagnosis of system failure in the chemical process. *Computers and Chemical Engineering*, 3, 489–493.

Isermann, R. and Ball, P. (1996). Trends in the application of model based fault detection and diagnosis of technical processes. In *Proceedings of the 13th IFAC World Congress*, volume N, 1–12. IEEE Press.

Jai, A.E. and Pritchard, A.J. (1987). Sensors and actuators in distributed systems. *International Journal of Control*, 46, 1139–1153.

Janna, W.S. (2000). *Engineering Heat Transfer*. Boca Raton: CRC Press, second edition.

Kanai, T. and Campbell, G. (1999). *Film Processing*. Hanser Gardner Publications.

Kang, H. and White, J. (1990). A double bubble tubular film process to produce biaxially oriented poly (p phenylene sulfide) (pps) film. *Polym. Eng. Sci*, 30, 1228.

Kang, H., White, J., and Cakmak, M. (1990). A basic study of single and double bubble tubular film extrusion of polyethylene terephthalate. *Int. Polym. Process*, 5, 62.

Kim, M. and White, J. (1992). A basic study of single and double bubble tubular film extrusion of polyethylene terephthalate. *Int. Polym. Process*, 7, 38.

Kokotovic, P., Khalil, H.K., and O'Reilly, J. (1999). *Singular Perturbation Methods in Control: Analysis and Design*, volume 25. Classics in Applied Mathematics.

Konak, A., Coit, D.W., and Smith, A.E. (2006). Multi-objective optimization using genetic algorithms: A tutorial. *Reliability Engineering and System Safety*, 91, 992–1007.

Kresta, J.V., Marlin, T.E., and MacGregor, J.F. (1991). Multivariable statistical monitoring of process operating performance. *Can. J. of Chem. Eng.*, 69, 35–47.

Kristinsson, K. and Dumont., G. (1996). Cross-directional control on paper machines using gram polynomials. *Automatica*, 32(4), 533–548.

Levy, S. and Carley, J.F. (1989). *Plastics extrusion technology handbook*. Industrial Press Inc.

Li, Q. (2001). *Observer-Based Fault Detection for Nuclear Reactors*. Ph.D. thesis, Department of Nuclear Engineering, Massachusetts Institute of Technology.

Looney, M.K., MacDonald, W.A., Moussalli, P.G.O., and Robinson, J.N. (2005). Formulation of polyester films and the role played by polymer, process and property relationships (3p's) on product design, manufacturing robustness and end use of functionality. In *Proceedings of the 7th World Congress of Chemical Engineering, SECC, Glasgow, UK*.

Lou, X., Willsky, A.S., and Verghese, G.C. (1986). Optimally robust redundancy relations for failure detection in uncertain systems. *Automatica*, 22(3), 333–344.

Lydersen, A.L. (1983). *Mass Transfer in Engineering Practice*. John Wiley & Sons.

Ma, M. and Williams, D. (1988). A simplified adaptive model predictive controller. *Tappi Journal*, 17, 190–194.

MacDonald, W.A. (2007). *Encyclopedia of Polymer Science and Technology*. Wiley, 3rd edition.

Maciejowski, J.M. (1989). *Multivariable Feedback Design*. Addison-Wesley.

Mijanovic, S., Stewart, G.E., Dumont, G.A., and Davies, M.S. (2002). Stability-preserving modification of paper machine cross-directional control near spatial domain boundaries. In *Proceedings of IEEE conference on decision and control, Las Vegas, Nevada, USA*.

Mironovski, L.A. (1979). Functional diagnosis of linear dynamic systems. *Automation and Remote Control*, 40, 1198–1205.

Mironovski, L.A. (1980). Functional diagnosis of dynamic system - a survey. *Automation and Remote Control*, 41, 1122–1142.

Mitchell, M. (1998). *An Introduction to Genetic Algorithms*. MIT Press.

Nellis, G. and Klein, S. (2008). *Heat Transfer*. Cambridge.

Ogata, K. (2002). *Modern Control Engineering*. Pearson Education International, fourth edition.

O'Reilly, J. (1983). *Observers for Linear Systems*. Academic Press Inc. (London) Ltd.

Patton, R.J., Chen, J., and Liu, G.P. (1997). Robust fault detection of dynamic systems via genetic algorithms. *IMechE Part I-J of Systems and Control Engineering*, 211(5), 357–364.

Patton, R.J., Chen, J., and Siew, T. (1994). Fault diagnosis in nonlinear dynamic systems via neural networks. In *Proceedings of the IEE International Conference: Control 1994, Warwick, UK*.

Piovoso, M.J. and Kosanovich, K.A. (1994). Applications of multivariate statistical methods to process monitoring and controller design. *International Journal of Control*, 59, 746–765.

Piovoso, M.J., Kosanovich, K.A., and Pearson, R.K. (1994). Monitoring process performance in real time. In *Proceedings of the American Control Conference*.

Pirkle, J.C.J. and Braatz, R.D. (2003). Dynamic modeling of blown film extrusion. *Polymer Engineering and Science*, 137, 159–178.

Rhee, S. and White, J. (2001). Pa612 double bubble tubular film process - processability and structure development. *Int Polym Process*, 16, 272–284.

Ringwood, J. (1995). Multivariable control using the singular value decomposition in steel rolling with quantitative robustness assessment. *Control Engineering Practice*, 3(4), 495–503.

Shames, I.H. and Cozzarelli, F.A. (1992). *Elastic and inelastic stress analysis*. Prentice-Hall International, Inc.

Sikora, R., Bialkowski, W.L., MacGregor, J., and Tayler, P. (1984). A self-tuning strategy for moisture control in papermaking. In *Proceedings of the American Control Conference*.

Simani, S., Fantuzzi, C., and Patton, R.J. (2003). *Model based Fault Diagnosis in Dynamic Systems Using Identification Techniques*. Springer.

Skogestad, S. (2008). *Chemical and Energy Process Engineering*. CRC Press.

Song, K. and White, J. (2000a). Single and double bubble tubular film extrusion of polybutylene terephthalate. *Int. Polym. Process*, 15, 157.

Song, K. and White, J. (2000b). Single and double bubble tubular film extrusion of polyethylene-2,6 naphthalate (pen). *Polym Eng Sci*, 40, 1122.

Stevens, M.J. and Covas, J.A. (1995). *Extruder principles and operation*. Chapman & Hall.

Stewart, G., Gorinevsky, D., and Dumont., G. (2003a). Feedback controller design for a spatially distributed system: the paper machine problem. *IEEE Transactions on Control Systems Technology*, 11(5), 612–628.

Stewart, G., Gorinevsky, D., and Dumont, G. (2003b). Two-dimensional loop shaping. *Automatica*, 39, 779–792.

Sutera, S. and Skalak, R. (1993). The history of poiseuille's law. *Annual Review of Fluid Mechanics*, 25, 1–19.

Taylor, A. and Duncan, S. (2006). Actuator mapping and stability in real-life cross-directional control systems. In *Proceedings of Control Systems 2006, Tampere, Finland*, 191–196.

Taylor, T.O. (1989). Not all mylar is archival. *Abbey Newsletter*, 13, 5.

Tham, M.T. (2002). Introduction to robust control. Technical report, Chemical and Process Engineering, University of Newcastle upon Tyne.

Tucker, C.L. (1989). *Computer Modeling for Polymer Processing*. Hanser Publishers.

VanAntwerp, J.G. and Braatz, R.D. (1999). Robust control of large scale paper machines. In *In AIChE annual meeting*.

VanAntwerp, J.G., Featherstone, A.P., Braatz, R.D., and Ogunnaike, B.A. (2007). Cross-directional control of sheet and film processes. *Automatica*, 43, 191–211.

Venkatasubramanian, V., Rengaswamy, R., Yin, K., and Kavuri, S. (2003). A review of process fault detection and diagnosis, part i: Quantitative model-based methods. *Computers and Chemical Engineering*, 27, 293–311.

Venkatasubramanian, V., Rengaswamy, R., Yin, K., and Kavuri, S. (2004). A review of process fault detection and diagnosis, part ii: Qualitative models and search strategies. *Computers and Chemical Engineering*, 27, 313–326.

Venkatasubramanian, V., Rengaswamy, R., Yin, K., and Kavuri, S. (2005). A review of process fault detection and diagnosis, part iii: Process history based methods. *Computers and Chemical Engineering*, 27, 327–346.

Vlachopoulos, J. and Strutt, D. (2003). An overview of polymer processing. Technical report, Centre for Advanced Polymer Processing and Design (CAPPA-D), Department of Chemical Engineering, McMaster University, Hamilton ON L8S 4L7, Canada.

Vose, M.D. (1999). *The simple genetic algorithm: foundations and theory*. Complex adaptive systems. Cambridge, Mass.: MIT Press.

Wilkie, J., Johnson, M., and Katebi, R. (2002). *control engineering: an introductory course*. palgrave.

Wills, A.G. and Heath, W.P. (2002). Analysis of steady-state performance for cross-directional control. In *Proceedings of IEE Conference on Control Theory Application*.

Wise, B.M. and Gallagher, N.B. (1996). The process chemometrics approach to process monitoring and fault detection. *Journal of Process Control*, 6, 329–348.

Yamane, H. and White, J. (1987). Simulation of tubular film extrusion of polymer melts: Non-newtonian and non-isothermal effects on bubble shape. *Int. Polym. Process*, 2, 107.

Zakian, V. (1979). New formulation for the method of inequalities. *IEE Transactions on Control Theory and Application*, 126(6), 579–584.

Zakian, V. and Al-Naib, U. (1973). Design of dynamical and control systems by the method of inequalities. *IEE Transactions on Control Theory and Application*, 120(11), 1421–1427.